Tracing Molecular Gas in the Andromeda Galaxy

by

Benjamin L. Gerard

Department of Astrophysical and Planetary Sciences

December 11$^{\text{th}}$, 2013

Thesis Adviser: Jeremy Darling, Department of Astrophysical and Planetary Sciences

Thesis Defense Committee:

- Jeremy Darling, Department of Astrophysical and Planetary Sciences
- Nikta Amiri, Department of Astrophysical and Planetary Sciences
- Erica Ellingson, Department of Astrophysical and Planetary Sciences
- John Gunther, Department of Jazz Studies

ABSTRACT

We present results from an Andromeda Galaxy (M31) survey of star-forming regions based on 24 μm luminosity for H_2O masers, $NH_3(1,1)$ and $NH_3(2,2)$ lines, and Hydrogen recombination lines (H66α). Although five H_2O masers were detected in the initial survey of 206 regions towards M31, we do not detect additional masers in a follow up survey of 300 similar luminous 24 μm regions. We do not detect $NH_3(1,1)$, $NH_3(2,2)$, or H66α lines in any of the 506 regions. The typical rms noise for 244 kHz channels in individual spectra is 2.5 mJy. Additionally, averaging and medianing 446 $NH_3(1,1)$, $NH_3(2,2)$, and H66α spectra and 441 H_2O spectra, shifted to the correct radial velocity as indicated by CO and HI, yields no detection for any observed line. The typical rms noise for 244 kHz channels in stacked spectra is 0.13 mJy. The non-detection of $NH_3(1,1)$ provides an upper limit on the typical $NH_3(1,1)$ integrated flux in a M31 giant molecular cloud. A comparison with typical Milky Way (MW) $NH_3(1,1)$ integrated fluxes scaled to the distance of M31 shows an ambiguity in consistency between our upper limit on the M31 NH_3 content and the typical MW NH_3 content depending on the use of the near or far distance in our MW flux scaling method. To resolve this ambiguity, we also examine the relationship between $NH_3(1,1)$ integrated flux and Herschel 500 μm flux density (i.e., the NH_3 abundance) for giant molecular cloud-sized regions in M31 and the MW. Comparing this relationship between M31 and the MW independently indicates that our upper limit on the typical M31 NH_3 abundance is consistent with the typical MW NH_3 abundance. The non-detection of H_2O provides an upper limit on H_2O maser peak flux density. Comparing this upper limit with typical MW H_2O maser peak flux densities scaled to the distance of M31 indicates that our upper limit on the M31 H_2O maser luminosity is consistent with the typical MW H_2O maser luminosity.

Subject headings: dark matter - galaxies: individual (M31) - galaxies: kinematics and dynamics - ISM: clouds - ISM: molecules - Local Group - masers - proper motions - radio lines: galaxies

1. Introduction

The Milky Way (MW) and the Andromeda Galaxy (M31) are the two most massive galaxies in the Local Group (LG)[1]. Thus, it is important to know their velocity vectors (or equivalently the M31 velocity vector in the MW reference frame, $\vec{v}_{\rm M31}$) in order to create an accurate LG dynamical model (e.g., van der Marel et al. 2012b). Radial velocities for M31 are readily available through measurements of Doppler motion (e.g., Nieten et al. 2006, Chemin et al. 2009), but measurements of M31's transverse velocity, $\vec{v}_{\rm M31\text{-}tan}$, are not clear (e.g., values for $\vec{v}_{\rm M31\text{-}tan}$ in Peebles et al. 2001, Sawa & Fujimoto 2005, Loeb et al. 2005, van der Marel & Guhathakurta 2008, van der Marel et al. 2012a, and Peebles & Tully 2013 do not show a clear agreement between one another; see Appendix 1). As a result, the M31 velocity vector, $\vec{v}_{\rm M31}$, is also not clear.

Measuring the proper motion[2] of five detected astrophysical water (H_2O) masers[3] in M31 (Darling 2011) is expected to provide a measurement of $\vec{v}_{\rm M31\text{-}tan}$ with an uncertainty of $\sim$5 μas yr^{-1} (1 μas $= \frac{1^\circ \times 10^{-6}}{3600}$; Darling 2011), or $\sim$18 km s^{-1} placed at 780 kpc (1 pc $\approx$ 3.26 light years), the distance to M31 (McConnachie et al. 2005). One other direct measurement of $\vec{v}_{\rm M31\text{-}tan}$ has been made from proper motion measurements of stars in M31, which yields an uncertainty for $\vec{v}_{\rm M31\text{-}tan}$ of 42 km s^{-1} (van der Marel et al. 2012a). Thus, measuring the proper motion of H_2O masers in M31 is expected to yield the most accurate value of $\vec{v}_{\rm M31\text{-}tan}$, and as a result provide the most accurate information to determine the LG, MW, and M31 masses, model LG dynamics (i.e., past and future evolution), and describe the LG dark matter structure (see Appendix 1).

Understanding the physical environment of these M31 H_2O masers and other molecular regions in M31 by comparison to similar and/or different physical conditions in the MW is also important. The MW and M31 have similar masses, density profiles, disk sizes, and star formation rates (Yin et al. 2009), and so we expect the physical conditions in giant molecular clouds (GMCs)[4] to be similar in both galaxies. In the MW, we observe a high abundance of

---

[1]The Local Group is a collection of $\sim$50 galaxies, all believed to be gravitationally bound to one another.

[2]Proper motion is the apparent motion of an object across the sky. This measurement can be used to obtain a tangential (angular) velocity of the measured object after subtracting out components for the Earth's diurnal motion, the Earth's annual motion, and the (orthogonal) components for the object's rotation and divergence (e.g., see Brunthaler et al. 2005, Brunthaler et al. 2007)

[3]A maser is a microwave laser. Like optical lasers, astrophysical masing occurs from the same process of population inversion and amplification via stimulated emission, but, unlike optical lasers, astrophysical masers are not phase coherent (e.g., see Chapman & Baan, 2008).

[4]A giant molecular cloud is a large cloud of gas and dust, $\sim$100 pc in diameter, containing much smaller

H_2O masers in HII regions[5] embedded within GMCs (e.g., Urquhart et al. 2011). However, in M31 we observe fewer H_2O masers across a broad range of GMCs (Darling 2011). This result could be because M31 is much further away from us compared to the MW, and thus our current sensitivity using radio telescopes is generally not adequate enough to detect masers, or it could be that there are actually fewer H_2O masers in M31 because the physical conditions in M31 GMCs are different from the physical conditions in MW GMCs. To address this ambiguity we reduced and analyzed spectral data in 446 different M31 GMCs for ammonia (NH_3), a tracer of dense gas and star formation in GMCs (e.g., Dunham et al. 2011, Longmore et al. 2013), hydrogen recombination lines, a tracer of HII regions in GMCs (e.g., Avalos & Lizano 2012), and water (H_2O) masers, also a tracer of dense gas and star formation in GMCs (e.g., Urquhart et al. 2011). We describe the physics of each line below.

1.1. NH_3

Any three dimensional molecule has three principle moments of inertia: $I_x, I_y,$ and I_z, and so the Hamiltonian operator for any rotating three dimensional molecule is

$$\hat{H} = \frac{{J_x}^2}{2I_x} + \frac{{J_y}^2}{2I_y} + \frac{{J_z}^2}{2I_z}, \tag{1}$$

where J_x, J_y, and J_z are the components of the total angular momentum projected along each principle axis. The square of the total angular momentum is

$$\mathbf{J}^2 = {J_x}^2 + {J_y}^2 + {J_z}^2 \tag{2}$$

The tetrahedral structure of NH_3 classifies it as a symmetric top molecule, meaning $I_x = I_y$, and so equation 1 becomes

$$\hat{H} = \frac{{J_x}^2 + {J_y}^2}{2I_\perp} + \frac{{J_z}^2}{2I_\parallel}, \tag{3}$$

where $I_x = I_y = I_\perp$ and $I_z = I_\parallel$. Combining equations 2 and 3 gives

$$\hat{H} = \frac{\mathbf{J}^2}{2I_\perp} + {J_z}^2 \left(\frac{1}{2I_\parallel} - \frac{1}{2I_\perp} \right) \tag{4}$$

The energy eigen values for equation 4 applied to the Schrödinger equation are then

$$W(J,K) = J(J+1)\frac{\hbar^2}{2I_\perp} + K^2\hbar^2 \left(\frac{1}{2I_\parallel} - \frac{1}{2I_\perp} \right), \tag{5}$$

---

regions of highly concentrated star formation.

[5]HII regions are regions of ionized hydrogen (HII).

where J is the quantum number for $\mathbf{J}^2$ and K is the quantum number for J_z. $I_\perp$ and $I_\parallel$ are typically measured in the laboratory and given as $B = \frac{\hbar}{4\pi I_\perp}$ and $C = \frac{\hbar}{4\pi I_\parallel}$ (referred to as rotational constants). For NH_3, $B = 283.13299$ GHz and $C = 185.75141$ GHz (Herzberg 1966).

There is a small potential barrier created by the plane of hydrogen atoms that acts to prevent the nitrogen atom from inverting NH_3's tetrahedral structure. However, because the barrier is small the nitrogen atom can tunnel through the plane of hydrogen atoms at constant (J, K) quantum numbers, creating a splitting of energy states. This process is referred to as rotation inversion, or inversion doubling. For example, $NH_3(J = 3, K = 3)$ rotation inversion transition occurs at a rest frequency of 23.870130 GHz (Wilson et al. 2012, pg. 438).

1.2. Hydrogen Recombination Lines

On the boundary of an HII region, where electrons first begin to recombine with protons, a series of electron transitions occurs from $n = \infty$ to $n = 1$ (n is the principal quantum number) as the electron cascades down to the ground state of hydrogen. These transitions are called hydrogen recombination lines. For example, analogous to the Lyman series, which has electron transitions for Lyman α ($n = 2 \rightarrow n = 1$), Lyman β ($n = 3 \rightarrow n = 1$), etc., we observe H66α ($n = 67 \rightarrow n = 66$) at

$$h(\nu_{\mathrm{H66}\alpha}) \approx -13.6 \text{ eV} \left(\frac{1}{67^2} - \frac{1}{66^2} \right) \tag{6}$$

$$\nu_{\mathrm{H66}\alpha} \approx 22.36 \text{ GHz} \tag{7}$$

1.3. H_2O

The H_2O molecule is an asymmetric top, and so it has three different principle moments of inertia, or three different rotational constants: $A = 835.73144$ GHz, $B = 435.05882$ GHz, and $C = 278.35730$ GHz (Herzberg 1966). H_2O must also have three quantum numbers for three orthogonal axes of rotation. One common choice of basis is $J_{K_a K_c}$, where J is the quantum number for $\mathbf{J}^2$ (i.e., the total angular momentum), K_a is the quantum number for $\mathbf{J}$ projected along the A-axis, and K_c is the quantum number for $\mathbf{J}$ projected along the C-axis[6]

[6]Note that because H_2O is asymmetric on all three principle axes, $\mathbf{J}$ will precess about K_a or K_c so that the time-averaged eigenvalues for projection of angular momentum onto the A and C axes satisfy the

(Wilson et al. 2012, chap. 15). A commonly observed astrophysical H_2O line in the $J_{K_aK_c}$ basis is the $J_{K_aK_c} = 6_{16}\rightarrow5_{23}$ 22.235253 GHz rotational transition, which is only observed as a maser transition(Wilson et al. 2012, pg. 483).

1.4. Preface

In this thesis we discuss the observations of 506 luminous 24 μm regions in M31 for NH_3(1,1), NH_3(2,2), H66α, and H_2O ($6_{16}\rightarrow5_{23}$), the data reduction process for these lines, the subsequent statistical averaging/medianing procedure used to analyze the typical properties of each observed region, the NH_3(1,1) content & NH_3 abundance in M31 GMCs, and the H_2O maser luminosity in M31 GMCs.

2. Observations, Data Reduction, and Stacking

2.1. How The Observations are Made

In radio astronomy, we use the wave nature of light instead of its particle nature. The power spectrum, $S(\nu)$ (i.e., power as a function of frequency), of an observed source is obtained from the autocorrelation of its voltage amplitude on the telescope's receiver by a Fourier transform:

A convenient choice of units allows for

$$p(t) = v^2(t),$$

since power $= \frac{(\text{voltage})^2}{\text{resistance}}$, where $p(t)$ is the received power and $v(t)$ is the voltage difference measured by a telescope receiver that is created by an electromagnetic wave being emitted from the observed source. The total energy emitted over time is then

$$E_{\text{em}} = \int_{-\infty}^{\infty} p(t)\mathrm{d}t = \int_{-\infty}^{\infty} v^2(t)\mathrm{d}t \equiv \int_{-\infty}^{\infty} S(t)\mathrm{d}t = 2\int_{0}^{\infty} S(\nu)\mathrm{d}\nu$$

We can then use the autocorrelation function,

$$R(\tau) \equiv \int_{-\infty}^{\infty} v(t')v(t'+\tau)\mathrm{d}t'$$

---

following: $K_a \leq J$ and $K_c \leq J$.

where τ is a variable time lag between two measurements of v, to show that (Burke & Graham-Smith 2010, chap. 3, appendix 1)

$$\int_{-\infty}^{\infty} v(t')v(t'+\tau)\mathrm{d}t' \overset{\mathrm{FT}}{\rightleftharpoons} 2\int_{0}^{\infty} V(\nu')(V(\nu'-\nu))\mathrm{d}\nu = 2\int_{0}^{\infty} V(\nu')V^{*}(\nu')\mathrm{d}\nu \tag{8}$$

$$= 2\int_{0}^{\infty} \left|V(\nu')\right|^{2}\mathrm{d}\nu \tag{9}$$

$$= 2\int_{0}^{\infty} S(\nu)d\nu, \tag{10}$$

and, thus, a Fourier transform of $R(\tau)$ gives $S(\nu)$. In practice, we can only estimate $R(\tau)$ over a finite time interval, $\mathcal{T}$, centered around a specific time, t. As a result, we can only estimate $S(\nu)$. But $\lim_{\mathcal{T}\to\infty}\left(\int_{t-\mathcal{T}/2}^{t+\mathcal{T}/2} v(t')v(t'+\tau)dt'\right) = R(\tau)$, which means a longer exposure time, $\mathcal{T}$, yields a better the estimate of $S(\nu)$.

To convert $S(\nu)$ to a flux density in Jy ($1\mathrm{Jy} = 10^{-26}\mathrm{Joules\ s^{-1}m^{-2}Hz^{-1}}$), each telescope has a gain, $G\left(\frac{\mathrm{Kelvin}}{\mathrm{mJy}} \propto \frac{\mathrm{power}}{\mathrm{mJy}}\right)$ (i.e., the units of Kelvin indicate that the object's observed power can be related to a temperature through the assumption of emission via blackbody radiation), which accounts for its effective collecting area[7], so that

$$\text{flux density} = \frac{S(\nu)}{G}$$

Thus, the final result is a flux calibrated spectrum: a plot of flux density vs. frequency.

2.2. Observations

We observed the $6_{16} \rightarrow 5_{23}$ 22.23508 GHz water maser line, $(J = 1, K = 1)$ and $(J = 2, K = 2)$ NH_3 rotation inversion lines at 23.69451 GHz and 23.72263 GHz, respectively, and the $(n = 67) \rightarrow (n = 66)$ 22.36417 GHz hydrogen recombination line (H66α) toward 506 luminous 24 μm sources in M31 (see Figure 1) with the Green Bank Telescope (GBT) in 2010 October through 2012 January. For all 506 sources, a 50 MHz bandpass was centered on a heliocentric velocity of -300 km $\mathrm{s^{-1}}$ for 239 sources in the central parts of the galaxy and along the minor axis, on -100 km $\mathrm{s^{-1}}$ for 136 sources in the redshifted northeast wedge of the galaxy, and on -500 km $\mathrm{s^{-1}}$ for 131 sources in the blueshifted southwest wedge of the galaxy (see Figure 1).

[7]but see §2.2, which explains how this gain is modified under varying weather and calibration conditions.

In order to center a spectrum on a velocity instead of frequency, we know from the effect of Doppler motion that

$$\frac{f_{\rm rest}}{f_{\rm obs}} = 1 + \frac{v_{\rm obs}}{c}, \tag{11}$$

where c is the speed of light, $f_{\rm rest}$ is the rest frequency of a given emission or absorption line, and $f_{\rm obs}$ is the observed frequency of a line due to any apparent radial (Doppler) motion causing a blueshift (radial motion towards the observer, increasing $f_{\rm obs}$) or redshift (radial motion away from the observer, decreasing $f_{\rm obs}$). Thus, we can anticipate where in the electromagnetic spectrum we should see a line if we already know its Doppler velocity. For M31, we know that the velocity comes from a combination of systemic motion[8] and rotational motion[9], and so knowing the rest frequency for a given line, we can center a given spectra to a velocity that appropriately matches what we expect to see due to Doppler motion. Figure 1 shows the 24 μm map of M31 with the pointing centers and primary beam size for our GBT water maser survey.

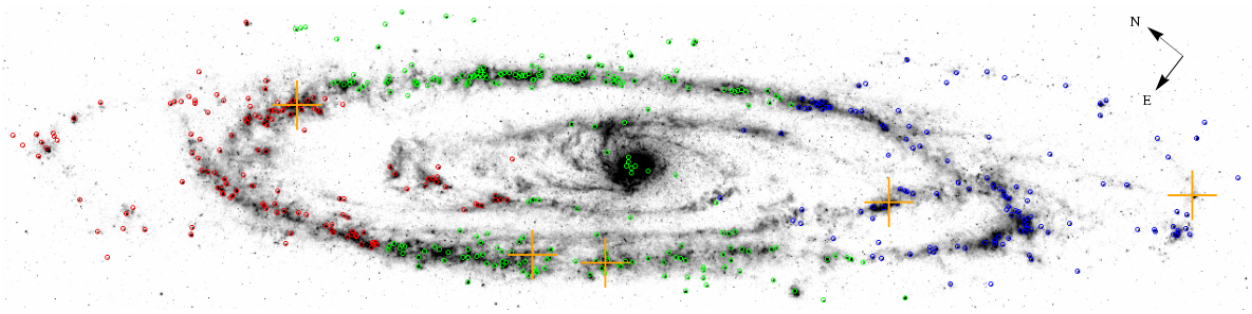

Fig. 1.— A M31 24 μm map (Gordon et al. 2006) showing the pointing centers for 506 luminous regions in our M31 water maser survey. The five detected 22 GHz H_2O masers (Darling 2011) are indicated with orange crosses. The colors indicate the -500 km s^{-1} (blue), -300 km s^{-1} (green), and -100 km s^{-1} (red) tuning centers, $v_{\rm obs}$, for each region, which were set based on their Doppler velocity in M31.

As explained in Darling (2011), observations were conducted with the dual K-band[10]

[8]M31 is moving towards the MW at ∼300 km s^{-1} (de Vaucouleurs et al. 1991).

[9]The southwest portion M31 is rotating towards the MW at ∼200 km s^{-1} and the northeast portion is rotating away from the MW at ∼200 km s^{-1} (see Nieten et al. 2006, Chemin et al. 2009).

[10]The K-band indicates a center frequency of ∼23 GHz (∼1.3 cm)

receivers in a nodding mode[11] in two circular polarizations[12] with a 12.2 kHz channel width and nine-level sampling[13]. The time on-source was 5 minutes except for sources that were re-observed to confirm or refute possible lines (typically 10 minutes). A winking calibration diode[14] and hourly atmospheric opacity estimates[15] were used for flux density calibration. Opacities ranged from 0.033 to 0.137 nepers but were typically 0.06 nepers. The estimated uncertainty in the flux density calibration is 20%. Pointing was typically good to within a few arcseconds (") and the largest pointing drifts during observations were no more than 6". The resolution of the 24 μm Spitzer image is 6" (Gordon et al. 2006), so the unresolved IR sources remained within the 33" GBT beam even during the largest pointing drifts. The 33" beam (FWHM) at 22 GHz spans 125 pc in M31.

2.3. Data Reduction

Spectra were Hanning smoothed[16] before averaging both polarizations. After averaging both polarizations spectra were Gaussian smoothed[17] to obtain a final spectral resolution of

---

[11]The basic concept of nodding involves taking two simultaneous observations of both the source and the background, regularly switching, or "nodding," each feed in order to subtract out the background noise from the on-source feed. A diagram of the nodding process is shown in Figure 2.

[12]An observation of each source is measured from one left circularly-polarized spectrum and one right circularly-polarized spectrum.

[13]Nine-level sampling is a digital conversion process which converts the measured voltage amplitude into a digital signal with a resolution of four evenly spaced positive possible voltage values and four evenly spaced negative values.

[14]Since almost all of the noise in a radio spectrum comes from the telescope's internal circuitry, a winking calibration diode is a diode that acts as a source of internal blackbody radiation with a known flux to serve as an internal flux calibrator. Throughout the observation process, the diode periodically turns on and off, allowing for a flux calibration between the difference of the on/off stages.

[15]As shown in the GBT Spectral Line Calibration Manual, www.gb.nrao.edu/GBT/DA/gbtidl/gbtidl_calibration.pdf, varying atmospheric opacity modifies the flux calibration by a factor of $e^{\left(\frac{\tau_0}{\sin(el)}\right)}$, where τ_0 is the measured atmospheric opacity at zenith and el is the altitude (i.e., the angle between the observed source and the horizon).

[16]Hanning smoothing is an algorithm used to remove Gibbs ringing after taking the Fourier transform of the autocorrelation function to obtain a power spectrum, but also decreases the resolution by a factor of two. The process involves running a mean across the spectral x-axis with a triangular smoothing kernel (i.e., the central channel is weighted by 0.5, and the two adjacent channels are weighted by 0.25).

[17]Gaussian smoothing is a weighted average of the flux values in each original channel that lie within the specified channel width for the new, post-smoothed resolution. This is identical to the Hanning smoothing

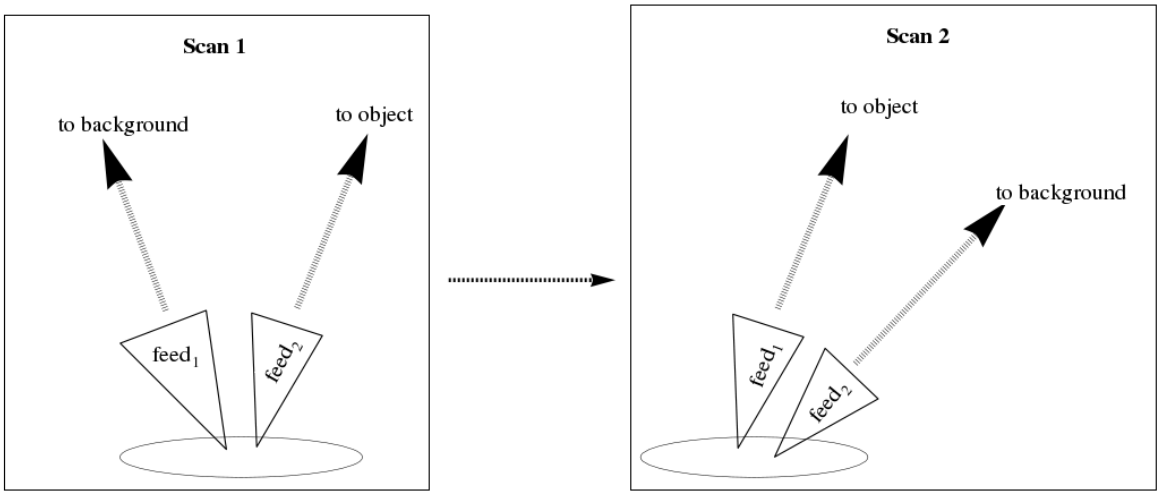

Fig. 2.— A schematic diagram of a nodding mode scan pair.

244 kHz for the H_2O, $NH_3(1,1)$, and $NH_3(2,2)$ line search. H66α spectra were additionally Gaussian smoothed to a final resolution of 732 kHz in order to account for their larger observed width in previous surveys (e.g., see Avalos & Lizano 2012). Polynomial baselines, typically of fifth order, were fit and subtracted to obtain flat and generally uniform-noise spectra. Spectral rms noise measurements for each pointing center are listed in Table 2. All data reduction was performed in GBTIDL[18].

2.4. Stacking

2.4.1. Methodology

An additional averaging/medianing procedure, called stacking, was used to characterize the typical properties of an M31 GMC. The basic concept involves centering each spectrum

kernel except that each channel at the old resolution is weighted by its proximity to the mean value on a Gaussian fit (where the 1σ width is $\sqrt{(\text{old resolution})^2 - (\text{new resolution})^2}$) of the flux values within the specified post-smoothed channel resolution. However, if a very narrow line is present in the pre-smoothed spectra (e.g., a one channel peak before a 10 channel smoothing), it is unlikely that this line will remain in the post-smoothed spectra (§3 explains how to catch this potentially "missed" line).

[18]GBTIDL (http://gbtidl.nrao.edu/) is an NRAO data reduction package, written in the IDL language for the reduction of GBT data.

on its known radial velocity[19], and then separately averaging and medianing all spectra. If a signal exists in each spectrum that is well below its individual noise limit, say at 0.2 σ, then, assuming that the noise is Gaussian and the 1σ standard deviation is relatively similar in all spectra, averaging/medianing all 506 spectra should decrease the noise by $\sqrt{506}\approx 22$ but not decrease the signal, and so the old $0.2\sigma_a$ signal becomes visible as a $4.4\sigma_b$ peak:

$$0.2\sigma_a \left(\frac{22\sigma_b}{\sigma_a}\right) = 4.4\sigma_b,$$

where σ_a is the typical 1σ standard deviation for individual an spectrum and σ_b is the 1σ standard deviation for the stacked spectrum.

The noise in each stacked spectrum decreases by $\sqrt{N}$ as a result of averaging[20]. In general, two signals, s_1 and s_2, from two different spectra are averaged as follows:

$$s_{\rm avg} = \frac{s_1\left(\frac{1}{{\sigma_1}^2}\right) + s_2\left(\frac{1}{{\sigma_2}^2}\right)}{\frac{1}{{\sigma_1}^2} + \frac{1}{{\sigma_2}^2}},$$

where $s_{\rm avg}$ is an average of s_1 and s_2 weighted by the variance from each spectra (i.e., a higher noise gets a lower weight). And so in general,

$$s_{\rm avg} = \frac{\sum_{n=1}^{N}\left(\frac{s_n}{{\sigma_n}^2}\right)}{\sum_{n=1}^{N}\left(\frac{1}{{\sigma_n}^2}\right)} \tag{12}$$

---

[19]The colors of the pointing centers in Figure 1 indicate that the radial velocity across M31 is a step function, but in reality this function has a smooth gradient (see Table 2).

[20]See the explanation below equation 13 which also accounts for the meadianing procedure in a stacked spectrum.

The resulting error on $s_{\rm avg}$ from equation 12 is

$$\sigma^2_{s_{\rm avg}} = \left(\sigma_1 \frac{d}{ds_1}\left(s_{\rm avg}\right)\right)^2 + \left(\sigma_2 \frac{d}{ds_2}\left(s_{\rm avg}\right)\right)^2 + ...$$

$$\sigma^2_{s_{\rm avg}} = \left(\sigma_1 \frac{\frac{1}{{\sigma_1}^2}}{\frac{1}{{\sigma_1}^2} + \frac{1}{{\sigma_2}^2} + ... + \frac{1}{{\sigma_N}^2}}\right)^2 + \left(\sigma_2 \frac{\frac{1}{{\sigma_2}^2}}{\frac{1}{{\sigma_1}^2} + \frac{1}{{\sigma_2}^2} + ... + \frac{1}{{\sigma_N}^2}}\right)^2 + ...$$

$$\sigma^2_{s_{\rm avg}} = \frac{\frac{1}{{\sigma_1}^2} + \frac{1}{{\sigma_2}^2} + ... + \frac{1}{{\sigma_N}^2}}{\left(\frac{1}{{\sigma_1}^2} + \frac{1}{{\sigma_2}^2} + ... + \frac{1}{{\sigma_N}^2}\right)^2}$$

$$\sigma_{s_{\rm avg}} = \frac{1}{\sqrt{\frac{1}{{\sigma_1}^2} + \frac{1}{{\sigma_2}^2} + ... + \frac{1}{{\sigma_N}^2}}}$$

$$\sigma_{s_{\rm avg}} = \frac{1}{\sqrt{\sum_{n=1}^{N}\left(\frac{1}{{\sigma_n}^2}\right)}},$$

but if $\sigma_1 \simeq \sigma_2 \simeq ... \simeq \sigma_n$ then

$$\sigma_{s_{\rm avg}} = \frac{1}{\sqrt{N/({\sigma_n}^2)}}$$

$$\sigma_{s_{\rm avg}} = \frac{\sigma_n}{\sqrt{N}} \tag{13}$$

So, if the spectra being stacked all have a similar rms noise (σ_n), then the noise for the stacked spectra is reduced by a factor of $\sqrt{N}$. Because medianing is a similar process to averaging, given that there are no large outliers, we expect the median stack (analogue to the average stack, except each channel is medianed after stacking N spectra instead of averaged) to also decrease the average noise in individual spectra by $\sqrt{N}$.

2.4.2. CO and HI velocities

For each of the individual 506 regions, we obtained an exact value for both carbon monoxide[21] (CO) $J = 1 \rightarrow 0$ and HI (neutral hydrogen)[22] radial velocities (Nieten et al. 2006, Chemin et al. 2009, respectively). We obtained CO radial velocities for each region from Nieten et al. 2006 (see Table 2), using a CO(1-0) radial velocity map of M31 (see Figure 3). This CO(1-0) map of M31 was obtained by convolving the radial velocity and position data of ∼1.7 million CO(1-0) spectra into a velocity map (Nieten et al. 2006).

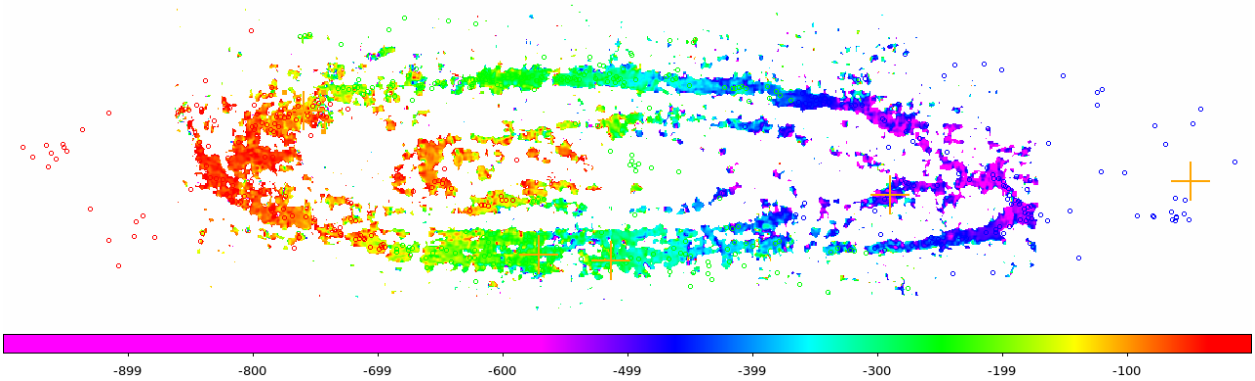

Fig. 3.— A M31 CO(1-0) line velocity map (Nieten et al. 2006) overlaid with the same 506 regions as shown in Figure 1. The scale bar indicates velocity in km s^{-1}.

We obtained HI velocities for each region using the M31 rotation curve[23] results from Chemin et al. (2009). A plot of the Chemin et al. (2009) M31 rotation curve is shown in Figure 4, which shows the M31 rotational velocity vs projected radius (i.e., radius projected into the plane of the M31 disk).

In order to convert this rotational velocity to a radial velocity, we used a tilted ring model, which projects the rotational velocity onto the plane of the sky and adds the result

[21]Equation 1 can also be generalized to diatomic molecules, such as carbon monoxide, where all three rotational constants are identical, and so only one quantum number, J is needed to describe rotational transitions.

[22]HI 21cm emission comes from the atomic hydrogen spin flip transition, where the spin of the proton and electron change from being aligned to being anti-aligned or vice versa.

[23]A galaxy's rotation curve shows its rotational velocity as a function of its radial distance from the center. A rotation curve can be obtained, for example, by extrapolating the Doppler velocity along a radially symmetric spiral galaxy, where the line of sight motion corresponds to a full three-dimensional space velocity, to its general rotational velocity structure in any direction.

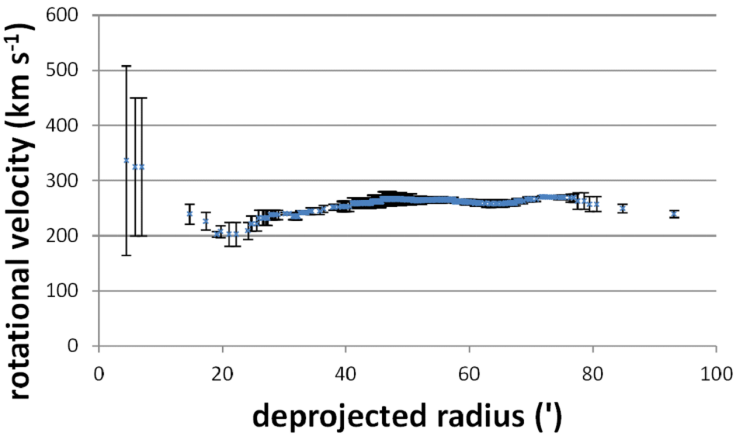

Fig. 4.— A plot of the M31 rotation curve (Chemin et al. 2009). The x-axis shows units of arcminutes (’), where 1 degree (°) = 60 arcminutes (’) = 3600 arcseconds (”).

to the systemic velocity:

$$v_{\rm radial} = v_{\rm systemic} - (v_{\rm rotational})\sin(i)\cos(\theta), \tag{14}$$

where i and θ are the inclination and azimuthal angle, respectively, defined below in Figure 5. We can use the M31 rotation curve (Figure 4) to determine $v_{\rm rotational}$ given the value of

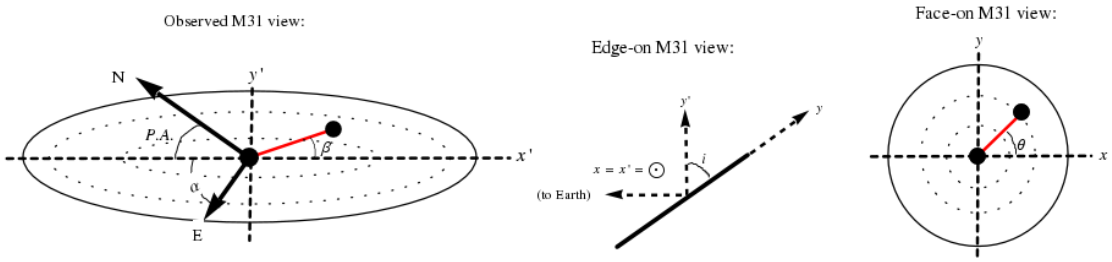

Fig. 5.— A diagram showing the parameters used in the tilted ring model.

$$r \equiv \sqrt{x^2 + y^2} \tag{15}$$

We can also find θ using x and y:

$$\theta \equiv \tan^{-1}\left(\frac{y}{x}\right), \tag{16}$$

but Figure 5 shows that $x' = x$ and $y' = y\cos(i)$, and thus equation 15 becomes

$$r = \sqrt{(x')^2 + \left(\frac{y'}{\cos(i)}\right)^2}, \tag{17}$$

and equation 16 becomes

$$\theta = \tan^{-1}\left(\frac{y'}{x'\cos(i)}\right) \tag{18}$$

Thus, given x', y', $v_{\rm systemic}$, and i, we can find $v_{\rm radial}$.

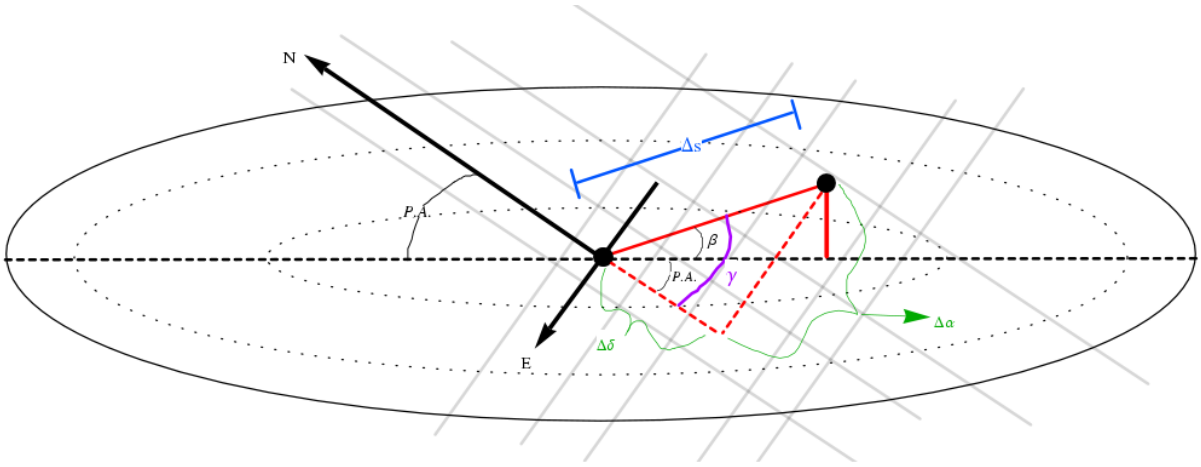

Fig. 6.— A diagram showing the parameters used to find x' and y' in the tilted ring model.

From Figure 6,

$$\begin{aligned}\beta &= \gamma - P.A \\ &= \tan^{-1}\left(\frac{\Delta\alpha}{\Delta\delta}\right) - P.A., \text{ and} \qquad (19)\\ \Delta s &= \sqrt{(\Delta\alpha)^2 + (\Delta\delta)^2} \qquad (20)\end{aligned}$$

Also,

$$\begin{aligned}\Delta\delta &= \delta_{\rm M31\ center} - \delta_{\rm object}, \text{ and} \\ \Delta\alpha &= (\alpha_{\rm M31\ center} - \alpha_{\rm object})\cos(\bar{\delta}) \qquad (21)\end{aligned}$$

where $\bar{\delta} = \frac{1}{2}(\delta_{\text{M31 center}} + \delta_{\text{object}})$. From equation 21, it follows that[24]

$$y' = (\Delta s)\sin\beta, \text{ and} \tag{22}$$

$$x' = (\Delta s)\cos\beta \tag{23}$$

So, using i (Walterbos & Kennicutt 1987), *P.A.* (Walterbos & Kennicutt 1987), $v_{\text{rotational}}$ & corresponding r (Chemin et al. 2009), v_{systemic} (de Vaucouleurs et al. 1991), $\alpha_{\text{M31 center}}$ & $\delta_{\text{M31 center}}$ (de Vaucouleurs et al. 1991), and specific values for α_{object} & δ_{object} in equations 14-23 yields an HI radial velocity for each object, shown in Table 2.

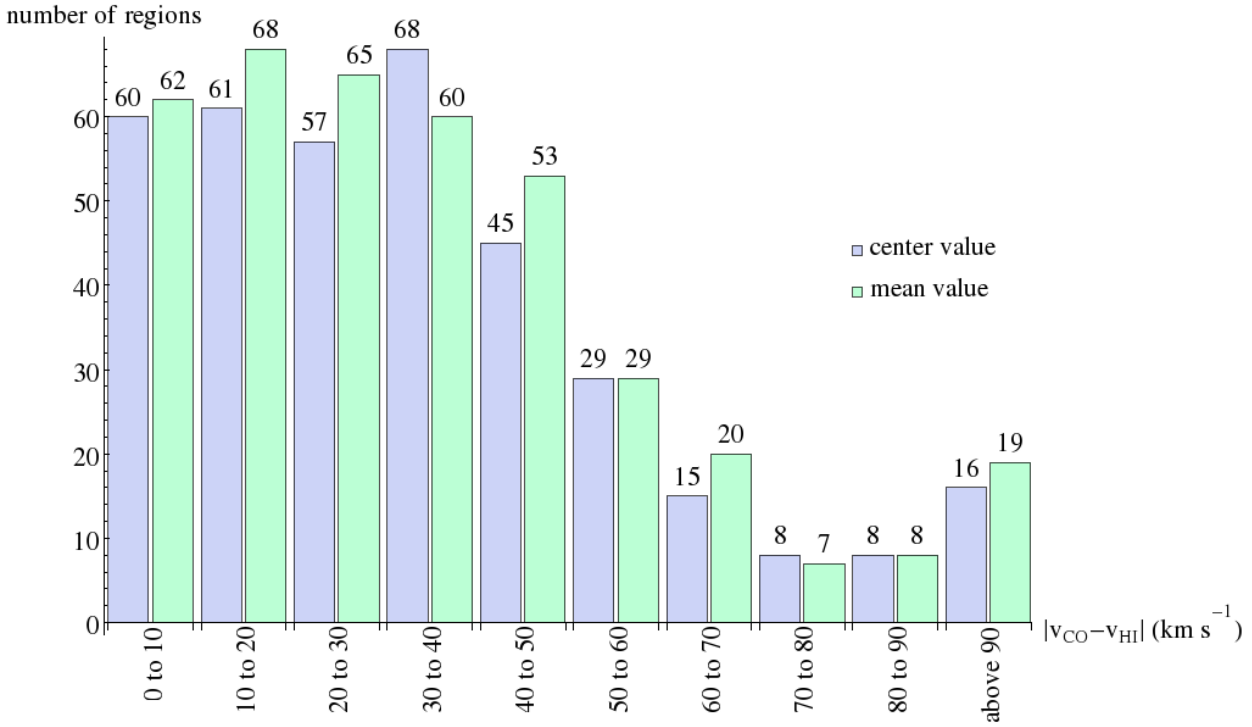

Fig. 7.— A histogram showing the discrepancy between CO and HI velocities for two different methods of obtaining CO velocity: taking the value directly in the center of each region ("center value"), and taking the average of all values within each region after removing individual outliers ("mean value").

Although a CO velocity, v_{CO}, is generally more precise than an HI velocity, v_{HI}, for

[24]In equations 20, 21, and throughout the rest of this thesis, α and δ represent right ascension and declination, respectively, and are the analogue of terrestrial longitude and latitude applied the celestial sphere. See Carrol & Ostlie (2006, §1.3) for a basic review of positions and distances on the sky.

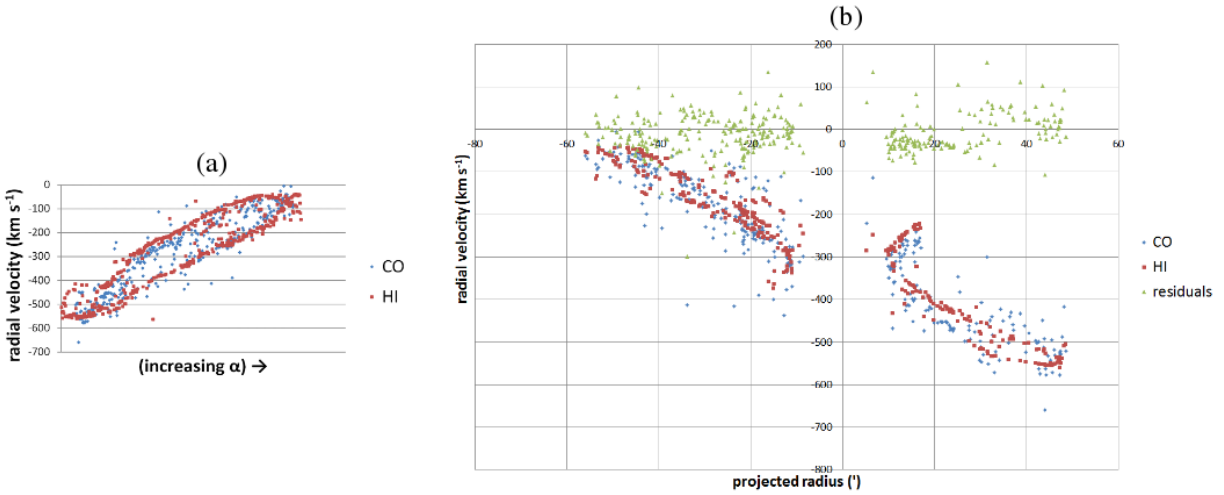

Fig. 8.— (a) A plot comparing the CO and HI velocities for each region in M31 vs. the region's right ascension (α), and (b) a plot comparing the CO and HI velocities for each region in M31 vs. the region's apparent radius (i.e., projected onto the sky) from the M31 dynamical center.

the same region[25], as shown in Figure 3, 139 of the 506 observed regions do not have CO coverage. Thus, because HI emission is much more ubiquitous than CO emission in the Universe, we used HI velocities to shift and center spectra in the stacking process when no CO coverage was available.

Because the Nieten et al. (2006) M31 CO map has multiple pixels within one GBT beam, $v_{\rm CO}$ could be defined in two different ways: choosing the CO velocity value at the center of the GBT beam, or averaging all the CO velocity values within the GBT beam[26]. Figure 7 shows that there is hardly any difference between these two procedures for the purpose of stacking 506 spectra, and so we chose to use the "center value" of the CO velocity within the GBT beam to define $v_{\rm CO}$.

Although $v_{\rm CO}$ and $v_{\rm HI}$ have similar accuracies (e.g., Figure 7 shows that 67% of all CO velocities differ by less than 40 km s^{-1} from their corresponding HI velocities; also see Chemin et al. 2009, Nieten et al. 2006, Table 2, and Figure 8), we expect $v_{\rm CO}$ to more

[25]Uncertainties for $v_{\rm CO}$ in Nieten et al. (2006) were ∼1 km s^{-1}, whereas uncertainties for $v_{\rm HI}$ in Chemin et al. (2009) range from ∼10 to 60 km s^{-1}.

[26]For the averaging procedure, we removed outlier $v_{\rm CO}$ values before averaging all other $v_{\rm CO}$ values within the GBT beam. We choose to define outliers at an arbitrary cutoff of a 30 km s^{-1} discrepancy between the mean and the outlier (i.e., *before* removing the outlier).

accurately trace molecular gas than $v_{\rm HI}$ (Nieten et al. 2006).

2.4.3. Removed Sources

Some $v_{\rm CO}$ values were not usable in stacking due to an unreasonably large velocity dispersion within the GBT beam, indicating a large enough disagreement with the center $v_{\rm CO}$ value as to effect the accuracy of the stacking process. A similar unreasonable uncertainty exists with one $v_{\rm HI}$ value. Thus, we removed individual sources from the stacking procedure whose CO velocity dispersion, $\Delta v_{\rm CO}$, was greater than 150 km s^{-1}, and we also removed sources whose CO velocity dispersion was less than 150 km s^{-1} but whose $v_{\rm HI}$ uncertainty, $\sigma v_{\rm HI}$, was greater than[27] 100 km s^{-1}. These conditions required that we remove 16 sources from the stacking procedure (see Table 1).

Some sources had both no CO coverage and no HI coverage. HI coverage was present for most sources, but 6 sources (see Table 1) with no CO coverage lie within 5.00', or 1.13 kpc (McConnachie et al. 2005), of the M31 dynamical center where there is no coverage for the M31 HI rotation curve (Chemin et al. 2009).

We crossed-matched planetary nebulae identified in Merrett et al. (2006) to remove an additional 9 sources (planetary nebulae) from our 506 luminous 24 μm sources. Additionally, we used a method similar to Ford et al. (2013)[28] to also identify an additional 29 old stars (i.e., in non-star-forming regions) from our source list (see Table 1). Planetary nebulae and old stars do not represent the same physical conditions as star forming regions, and so we also removed these objects from the stacking procedure.

Table 1 shows the 60 sources removed from the stacking process, resulting in a total stack of 446 objects[29] instead of 506 objects. Table 2 shows all 506 observed sources. The names of observed sources are listed in the sexagesimal form ($\alpha + \delta$).

---

[27]Although the main components contributing to M31 radial velocity measurements are its rotational and systemic velocities, some regions may carry a peculiar velocity that does not agree with the results of obtaining $v_{\rm HI}$ from the tilted ring model (which only accounts for rotational and systemic velocities), and so we removed sources with a large $\Delta v_{\rm CO}$ from the stacking procedure instead of simply substituting $v_{\rm HI}$ for $v_{\rm CO}$.

[28]See Figure 4 in Ford et al. 2013. We use a similar method, plotting 24 μm emission vs. 3.6μm emission to identify the old stars.

[29]For the H_2O stack, we also removed the additional five detected H_2O masers from Darling (2011), shown in bold in Table 2, yielding a total stack of 441 objects for H_2O.

Table 1. Removed Sources

Object (J2000)	v_{CO} (km s^{-1})	Δv_{CO} (km s^{-1})	v_{HI} (km s^{-1})	Removed (see note)	Object (J2000)	v_{CO} (km s^{-1})	Δv_{CO} (km s^{-1})	v_{HI} (km s^{-1})	Removed (see note)
003838.7+402613.5	···	···	-513(39)	O	004300.0+413654.2	-241	17	-195(54)	O
003849.2+402551.7	···	···	-534(31)	O	004310.0+413751.6	-201	79	-180(57)	PN
003950.9+402252.1	···	···	-544(15)	PN	004310.5+410426.8	-437	584	-336(22)	Δv_{CO}
003954.4+403820.4	···	···	-538(24)	O	004314.0+413906.3	-416	508	-173(59)	Δv_{CO}
004031.2+403952.0	-659	225	-552(13)	Δv_{CO}	004314.2+410033.9	···	···	-339(24)	O
004040.4+402709.8	···	···	-503(45)	PN	004321.7+414033.2	-286	156	-162(59)	Δv_{CO}
004044.2+404446.4	-433	150	-545(10)	Δv_{CO}	004325.6+410206.4	···	···	-327(17)	O
004121.2+411947.8	-241	399	-323(14)	Δv_{CO}	004329.2+414848.0	-193	47	-170(58)	PN
004129.5+411006.3	-452	162	-384(45)	Δv_{CO}	004332.5+410907.0	-320	54	-303(4)	O
004129.8+412211.1	···	···	-312(8)	O	004341.5+414224.3	···	···	-127(54)	O
004201.5+404115.7	···	···	-425(58)	O	004341.7+415313.0	···	···	-161(59)	O
004208.9+412329.8	-321	19	-287(9)	O	004351.4+415718.7	-226	195	-151(62)	Δv_{CO}
004210.7+412322.3	-304	15	-286(9)	O	004354.8+414715.6	-413	199	-115(55)	Δv_{CO}
004226.1+410548.2	-467	59	-433(53)	O	004355.1+411433.1	-240	189	-269(19)	Δv_{CO}
004228.1+405657.7	-422	44	-406(53)	O	004355.8+411211.6	-229	99	-281(12)	PN
004228.3+412911.4	-293	22	-249(30)	O	004403.9+413414.8	···	···	-96(20)	O
004228.4+412852.4	-268	23	-250(30)	O	004410.5+420247.5	···	···	-138(61)	O
004229.8+410550.6	···	···	-403(46)	O	004410.6+411653.4	-122	164	-256(26)	Δv_{CO}
004230.1+412904.0	-273	7	-248(31)	O	004416.3+411730.9	-238	163	-254(28)	Δv_{CO}
004230.9+405714.6	-393	19	-400(52)	O	004419.3+412247.0	-247	183	-219(44)	Δv_{CO}
004232.7+411143.6	···	···	-563(113)	σv_{HI}	004420.2+415101.5	-232	223	-82(38)	Δv_{CO}
004236.4+413308.7	-278	224	-233(38)	Δv_{CO}	004433.8+415249.7	-82	17	-63(29)	PN
004237.4+414158.3	···	···	-227(41)	O	004435.6+415606.9	-135	0	-78(37)	PN
004241.7+411435.0	···	···	···	···	004506.1+415121.0	-48	25	-47(15)	O
004241.9+405155.2	···	···	-380(44)	O	004515.9+420254.4	···	···	-52(16)	O
004244.4+411608.5	···	···	···	···	004540.0+415510.2	-55	20	-60(23)	PN
004245.3+411656.9	···	···	···	···	004608.5+421131.0	···	···	-48(10)	O
004247.0+411618.4	···	···	···	···	004641.6+421156.2	···	···	-46(15)	PN
004248.2+411651.7	···	···	···	···	004642.6+421406.8	···	···	-42(12)	O
004249.1+411554.6	···	···	···	···	004703.1+415755.4	···	···	-145(53)	O

Note. — In the "Removed" column, " ··· " indicates a source with no CO or HI coverage, "Δv_{CO}" indicates a source with Δv_{CO}>150 km s^{-1}, "σv_{HI}" indicates a source with σv_{HI}>100 km s^{-1}, "PN" indicates a source identified as a planetary nebula in Merrett et al. (2006), and "O" indicates a source we identified as an old star/non-star-forming-region using a method similar to Ford et al. (2013, Fig. 4).

Table 2. Water Maser Survey Results

Object	rms Noise				v_{obs}	v_{CO}	v_{HI}
	H_2O	$NH_3(1,1)$	$NH_3(2,2)$	H66α			
(J2000)	(mJy)	(mJy)	(mJy)	(mJy)	(km s^{-1})	(km s^{-1})	(km s^{-1})
003838.7+402613.5	2.0	2.4	2.3	2.2	-500	···	-513(39)
003849.2+402551.7	3.2	2.7	2.6	3.2	-500	···	-534(31)
003852.5+401904.9	2.0	2.1	2.4	2.0	-500	···	-558(12)
003904.8+402927.4	1.2	1.3	1.5	1.3	-500	···	-530(32)
003906.7+403704.5	3.5	2.8	3.0	3.0	-500	···	-495(54)
003909.8+402705.0	2.1	2.1	2.1	2.0	-500	···	-538(20)
003910.2+403725.6	3.2	2.8	4.2	2.9	-500	···	-497(53)
003914.6+404157.9	2.1	2.2	2.3	2.1	-500	···	-474(60)
003916.1+403629.5	3.0	2.6	2.8	2.9	-500	···	-506(47)
003918.9+402158.4	0.7	0.6	0.6	0.5	-500	···	-552(10)
003930.2+402106.4	3.7	2.6	3.0	3.5	-500	···	-551(10)
003933.2+402215.6	3.2	2.8	2.8	3.2	-500	···	-551(11)
003935.2+404814.6	2.1	2.1	2.1	2.2	-500	···	-456(62)
003937.5+402011.5	3.4	2.9	2.9	3.2	-500	···	-551(12)
003938.9+401921.3	2.5	2.3	2.4	2.4	-500	···	-548(14)
003939.1+405018.3	1.9	2.3	2.0	2.0	-500	···	-447(62)
003939.8+402856.3	3.1	2.8	2.8	3.1	-500	···	-554(10)
003941.5+402133.7	1.7	2.1	2.2	2.3	-500	···	-547(12)
003941.9+402045.6	2.0	2.0	2.1	2.1	-500	···	-546(13)
003943.0+402039.9	2.1	2.4	2.5	2.3	-500	···	-545(14)
003944.5+402030.4	3.3	2.9	2.5	2.6	-500	···	-544(15)
003945.2+402058.0	1.9	2.4	2.4	2.2	-500	···	-544(15)
003948.5+403113.1	2.0	1.9	2.0	2.2	-500	···	-557(10)
003950.5+402305.9	2.2	2.2	2.2	2.2	-500	···	-544(14)
003950.9+402252.1	1.9	2.1	2.2	2.0	-500	···	-544(15)
003951.3+405306.1	1.9	2.1	2.1	2.2	-500	···	-438(60)
003954.4+403820.4	3.4	3.5	3.6	3.6	-500	···	-538(24)
003956.8+402437.6	1.9	2.2	2.4	2.1	-500	···	-544(15)
004000.3+405318.6	2.0	2.2	2.2	2.1	-500	···	-440(59)
004004.7+405840.9	3.2	3.2	3.2	3.3	-500	···	-415(57)
004010.4+404517.7	1.9	2.0	2.3	2.0	-500	-502	-517(41)
004020.3+403124.5	2.1	2.4	2.6	2.0	-500	···	-549(16)
004020.5+403723.9	2.0	2.3	2.2	2.1	-500	-539	-560(16)
004023.8+403904.4	3.4	3.5	3.7	3.3	-500	-495	-555(14)
004026.2+403706.5	3.0	3.7	3.9	3.3	-500	···	-559(16)
004030.9+404230.0	3.0	2.3	2.8	3.1	-500	-496	-550(14)
004031.2+403952.0	2.9	2.4	2.4	2.5	-500	-659	-552(13)
004031.3+404032.8	2.1	2.0	2.0	1.6	-500	-449	-552(13)
004031.7+404127.0	3.3	3.0	3.3	2.7	-500	-562	-552(13)
004032.5+405127.4	2.0	2.3	1.9	1.9	-500	-450	-497(48)
004032.6+403856.1	3.3	2.9	2.8	2.6	-500	-533	-554(14)
004032.7+403531.2	2.1	2.4	2.7	2.0	-500	-528	-550(17)
004032.7+403936.5	3.5	3.4	3.4	3.4	-500	-563	-555(14)
004032.7+410045.1	2.0	2.0	2.0	2.1	-500	-457	-419(57)

Table 2—Continued

Object	rms Noise				v_{obs}	v_{CO}	v_{HI}
	H_2O	$NH_3(1,1)$	$NH_3(2,2)$	H66α			
(J2000)	(mJy)	(mJy)	(mJy)	(mJy)	(km s^{-1})	(km s^{-1})	(km s^{-1})
004032.8+405540.2	1.9	2.1	2.2	2.0	-500	-449	-464(61)
004032.9+403919.2	3.3	3.6	3.6	3.2	-500	-577	-555(14)
004033.0+404102.8	3.0	3.7	3.5	3.1	-500	-574	-552(13)
004033.3+403352.1	3.1	2.8	2.7	2.9	-500	···	-542(21)
004033.8+403246.6	3.1	2.8	2.7	2.8	-500	···	-538(24)
004034.7+403541.2	2.8	2.8	3.0	2.8	-500	-578	-548(18)
004035.1+403701.1	4.0	3.5	4.0	3.0	-500	-518	-553(18)
004035.8+403724.6	3.6	5.1	3.3	3.7	-500	-572	-554(18)
004036.0+403821.0	3.0	3.3	3.4	3.1	-500	···	-551(15)
004036.1+410117.5	2.1	1.9	1.8	2.0	-500	···	-419(57)
004036.3+403641.9	2.1	2.1	2.2	2.0	-500	-532	-551(18)
004036.3+405329.3	1.9	2.0	2.1	2.1	-500	-571	-487(54)
004036.8+403557.1	2.0	2.2	2.1	2.0	-500	-548	-548(20)
004038.0+403514.9	2.9	3.8	3.3	3.4	-500	-526	-543(22)
004038.0+404728.3	2.0	2.2	2.1	2.0	-500	···	-531(21)
004038.6+403814.7	2.9	3.7	3.6	3.3	-500	···	-549(16)
004038.7+403533.2	2.3	2.2	2.3	2.3	-500	-537	-543(22)
004038.8+403431.0	3.4	3.5	3.3	3.0	-500	-488	-538(25)
004039.4+403730.5	3.4	4.4	3.2	3.3	-500	-543	-550(19)
004039.7+403457.9	2.2	2.2	2.2	2.3	-500	-521	-539(24)
004040.4+402709.8	2.2	2.2	2.2	2.0	-500	···	-503(45)
004041.6+405105.0	2.0	2.0	1.8	1.7	-500	-543	-511(37)
004042.1+403454.5	3.4	3.2	3.5	3.3	-500	-531	-535(27)
004043.3+404321.9	3.1	3.0	2.9	2.7	-500	-524	-547(13)
004043.6+403530.5	3.3	2.9	2.8	3.2	-500	-548	-537(27)
004043.7+405251.5	2.0	2.0	2.2	2.1	-500	-441	-499(44)
004044.2+404446.4	3.0	2.8	3.1	2.5	-500	-433	-545(10)
004045.7+405134.5	1.9	1.8	2.2	1.8	-500	···	-513(34)
004046.4+405541.9	3.0	2.7	2.5	2.6	-500	-512	-480(55)
004046.5+405606.4	2.8	2.7	2.5	2.8	-500	-543	-476(56)
004047.3+405903.2	2.0	2.0	2.1	2.0	-500	-493	-450(60)
004050.0+405938.5	1.7	2.3	2.2	2.0	-500	-498	-448(60)
004051.6+410006.5	2.9	2.5	2.5	2.5	-500	-499	-446(60)
004051.7+403602.3	2.1	2.2	2.3	2.2	-500	···	-526(34)
004051.9+403249.7	3.4	3.8	3.4	2.9	-500	-418	-510(43)
004053.0+403218.0	3.8	3.8	3.5	3.7	-500	-522	-505(45)
004055.1+403703.2	3.8	4.0	3.6	3.4	-500	-526	-526(35)
004057.3+403607.0	2.2	2.3	2.4	2.2	-500	···	-517(40)
004058.2+410302.3	1.9	2.2	2.0	2.1	-500	-469	-425(58)
004058.3+403711.1	2.1	2.2	2.1	2.1	-500	-512	-521(39)
004058.4+405325.2	2.2	2.3	2.4	2.0	-500	···	-511(27)
004058.4+410217.9	1.9	2.2	2.1	1.9	-500	-467	-431(59)
004058.4+410225.9	2.0	2.1	2.0	2.1	-500	-470	-430(58)
004058.6+404558.0	2.1	2.0	1.8	2.1	-500	-502	-541(11)

Table 2—Continued

Object	rms Noise				v_{obs}	v_{CO}	v_{HI}
	H_2O	$NH_3(1,1)$	$NH_3(2,2)$	H66α			
(J2000)	(mJy)	(mJy)	(mJy)	(mJy)	(km s^{-1})	(km s^{-1})	(km s^{-1})
004058.6+410332.3	3.0	2.8	3.0	3.1	-500	-466	-423(59)
004059.1+410233.1	2.1	2.4	2.3	2.2	-500	-473	-430(58)
004059.8+403652.4	4.8	4.2	3.3	3.0	-500	-493	-516(41)
004100.6+410334.0	3.7	3.0	3.0	3.2	-500	-460	-423(58)
004101.6+410405.8	2.3	2.2	2.1	2.1	-500	-453	-419(57)
004102.0+410254.9	1.7	1.9	1.9	1.9	-500	-471	-430(58)
004102.3+410431.7	2.1	2.4	2.2	2.0	-500	-452	-416(56)
004102.7+410344.5	2.1	2.1	2.4	1.9	-500	-455	-422(57)
004103.1+403749.9	2.3	2.4	2.3	2.0	-500	-499	-516(42)
004104.8+410534.6	1.8	1.2	1.2	1.3	-500	-453	-409(54)
004107.2+410410.0	2.0	2.1	2.2	2.2	-500	-453	-424(57)
004107.6+404812.5	3.5	2.9	2.8	3.0	-500	-522	-533(10)
004108.6+410437.9	1.2	1.3	1.2	1.2	-500	-451	-421(57)
004109.1+404852.7	3.0	3.6	3.9	3.4	-500	-483	-534(10)
004109.2+404910.3	3.1	3.6	3.7	3.3	-500	-498	-534(9)
004110.4+404949.5	3.1	3.0	3.5	3.0	-500	-551	-529(10)
004110.6+410516.4	2.2	2.6	2.2	2.2	-500	-454	-416(56)
004112.5+410609.7	3.4	2.6	2.9	2.5	-300	-455	-409(54)
004113.7+403918.6	2.2	2.2	2.3	2.2	-500	-479	-502(49)
004113.8+410814.6	2.0	2.1	2.2	2.0	-300	-424	-392(49)
004113.9+410736.1	2.2	2.0	2.2	2.0	-300	-417	-397(50)
004114.8+410923.7	3.8	3.0	3.3	3.4	-300	-425	-384(46)
004115.9+404011.6	3.1	2.8	2.6	2.7	-500	-462	-503(49)
004119.1+404857.4	3.6	3.1	3.2	3.4	-500	-457	-523(17)
004119.5+411948.8	3.9	3.3	3.1	3.0	-300	-268	-323(15)
004120.0+410821.5	3.0	2.7	2.8	2.6	-300	-396	-395(50)
004120.9+403414.0	2.4	2.7	2.6	2.5	-500	···	-466(58)
004121.2+411947.8	2.5	2.7	2.5	2.5	-300	-241	-323(14)
004121.7+404947.7	1.4	1.5	1.6	1.4	-500	-529	-517(18)
004123.2+405000.6	3.4	3.3	2.9	3.0	-500	-547	-516(19)
004124.1+411124.1	3.1	3.7	3.7	3.7	-300	-398	-372(40)
004124.8+411154.6	3.4	2.9	2.7	2.6	-300	-403	-368(39)
004125.4+404200.4	3.7	3.2	3.1	3.3	-500	-471	-493(54)
004126.1+404959.1	3.7	3.2	3.3	3.5	-500	-498	-516(23)
004126.5+411206.9	3.0	3.0	2.8	2.8	-300	-398	-367(38)
004127.3+404242.7	2.0	2.3	2.3	2.2	-500	-440	-493(54)
004128.1+404155.2	2.0	2.4	2.1	2.2	-500	-459	-487(56)
004128.1+411222.6	3.6	4.0	4.4	3.2	-300	-386	-365(37)
004129.2+411242.8	4.2	4.2	4.1	3.6	-300	-414	-362(36)
004129.3+404218.9	2.2	2.3	2.2	2.2	-500	-430	-486(56)
004129.5+411006.3	4.0	3.9	4.4	3.8	-300	-452	-384(45)
004129.8+405059.5	2.2	1.6	1.7	1.7	-500	-476	-509(24)
004129.8+412211.1	3.1	3.0	2.8	2.9	-300	···	-312(8)
004130.3+410501.7	3.1	3.0	3.4	3.1	-500	-473	-440(55)

Table 2—Continued

Object	rms Noise				v_{obs}	v_{CO}	v_{HI}
	H_2O	$NH_3(1,1)$	$NH_3(2,2)$	H66α			
(J2000)	(mJy)	(mJy)	(mJy)	(mJy)	(km s^{-1})	(km s^{-1})	(km s^{-1})
004131.9+411331.5	3.8	4.4	4.1	4.1	-300	-414	-357(33)
004135.7+405009.3	2.4	2.8	2.8	2.4	-500	···	-498(39)
004136.9+403805.6	2.2	2.4	2.2	2.3	-500	···	-452(59)
004137.0+405142.5	3.3	3.3	3.0	3.5	-500	-461	-498(33)
004138.6+404401.2	3.4	3.1	3.0	3.1	-500	-422	-474(59)
004141.3+411916.7	2.4	2.3	2.6	2.5	-300	···	-321(13)
004143.6+410840.1	2.0	2.0	2.1	2.0	-500	-400	-411(52)
004144.6+411658.1	3.9	4.4	4.1	3.9	-300	-361	-333(20)
004145.0+404746.4	2.2	2.5	2.4	2.4	-500	···	-473(57)
004146.7+411846.6	3.3	2.8	3.1	3.0	-300	-326	-323(14)
004147.4+411942.4	3.9	4.3	4.4	4.1	-300	-358	-317(11)
004148.2+411903.8	3.6	3.2	4.5	3.1	-300	-329	-321(13)
004149.6+411953.8	2.4	2.7	2.5	2.3	-300	-389	-315(10)
004151.3+412500.7	2.8	2.6	2.7	2.4	-300	···	-293(6)
004151.6+404620.5	2.0	2.4	2.1	2.1	-500	-300	-456(61)
004151.9+412442.1	3.3	3.1	3.3	3.6	-300	···	-294(6)
004154.5+404718.9	2.2	2.3	2.2	2.1	-500	-407	-454(61)
004159.4+405720.8	2.1	1.7	1.7	1.8	-500	···	-473(46)
004200.6+404747.8	2.2	2.5	2.4	2.3	-300	···	-443(61)
004200.9+405217.2	2.1	2.2	2.2	2.1	-500	-346	-452(58)
004201.5+404115.7	2.3	2.4	2.5	2.3	-300	···	-425(58)
004202.4+412436.0	1.1	1.1	1.2	1.3	-300	-310	-288(9)
004202.9+412232.4	1.1	1.3	1.2	1.1	-300	-349	-295(5)
004203.9+404907.1	2.6	2.1	2.1	2.4	-300	···	-441(61)
004204.9+404936.6	2.2	2.4	2.2	2.5	-300	-472	-440(61)
004206.7+405621.5	2.0	2.3	2.0	2.0	-500	···	-446(53)
004208.5+405720.2	2.0	2.0	2.1	2.1	-500	-449	-449(54)
004208.5+412409.8	2.2	2.2	2.1	2.1	-300	-325	-285(10)
004208.7+405052.1	2.2	2.1	2.3	2.0	-300	-435	-436(61)
004208.8+412639.9	3.2	2.8	2.9	2.7	-300	-310	-276(15)
004208.9+412329.8	2.3	2.7	2.2	2.1	-300	-321	-287(9)
004209.0+412442.3	2.3	2.3	2.3	2.3	-300	-287	-282(12)
004209.5+412705.5	2.1	2.4	2.3	2.0	-300	···	-274(16)
004209.5+412832.3	3.3	2.9	3.1	2.6	-300	···	-270(18)
004209.8+412412.2	2.2	2.3	2.2	2.3	-300	-328	-283(11)
004210.3+412529.3	2.1	2.7	2.4	2.5	-300	-322	-278(14)
004210.7+412322.3	2.2	2.0	2.3	2.4	-300	-304	-286(9)
004211.2+412442.6	2.4	2.1	2.3	2.3	-300	-295	-280(13)
004211.6+411909.4	2.7	2.8	2.4	2.6	-300	···	-308(6)
004212.3+412415.7	2.9	2.7	2.7	2.6	-300	-349	-281(12)
004213.8+405117.7	3.9	3.4	3.7	3.5	-300	-382	-427(59)
004214.8+412508.9	2.8	3.0	2.8	2.6	-300	-320	-276(15)
004218.1+412631.1	2.4	2.1	2.6	2.5	-300	-267	-268(20)
004218.7+412751.8	2.7	2.7	2.5	2.6	-300	-326	-263(23)

Table 2—Continued

Object	rms Noise				v_{obs}	v_{CO}	v_{HI}
	H_2O	$NH_3(1,1)$	$NH_3(2,2)$	H66α			
(J2000)	(mJy)	(mJy)	(mJy)	(mJy)	(km s^{-1})	(km s^{-1})	(km s^{-1})
004220.6+412749.0	3.1	2.6	2.6	2.7	-300	-300	-261(24)
004221.7+412827.6	2.8	4.0	3.2	2.7	-300	-259	-258(25)
004224.8+412758.7	2.9	3.0	3.0	2.8	-300	-291	-256(26)
004225.9+412831.9	2.9	2.7	2.7	2.9	-300	-298	-254(28)
004226.1+410548.2	3.8	3.0	2.9	2.9	-500	-467	-433(53)
004226.4+412811.2	3.4	2.5	2.3	3.1	-300	-278	-254(27)
004227.6+412019.6	2.1	2.3	2.1	2.0	-300	-221	-285(10)
004227.9+413258.5	2.5	2.7	2.7	2.5	-300	···	-244(33)
004228.1+405657.7	2.7	2.3	2.4	2.3	-300	-422	-406(53)
004228.3+412911.4	3.1	2.9	2.6	3.1	-300	-293	-249(30)
004228.4+412852.4	1.2	1.3	1.5	1.4	-300	-268	-250(30)
004229.8+410550.6	2.9	2.6	2.5	2.6	-300	···	-403(46)
004230.1+412904.0	2.8	2.5	2.6	2.6	-300	-273	-248(31)
004230.3+412935.9	4.0	3.0	3.2	3.3	-300	-283	-246(32)
004230.9+405714.6	3.0	2.8	2.9	3.2	-300	-393	-400(52)
004232.1+412936.5	2.6	2.5	2.5	2.5	-300	-260	-244(33)
004232.3+413008.7	2.7	2.4	2.7	2.6	-300	-273	-242(34)
004232.7+411143.6	2.0	2.1	2.1	2.1	-300	···	-563(113)
004234.2+413007.3	3.0	2.4	3.0	2.6	-300	-263	-240(35)
004235.0+404838.1	2.2	2.3	2.4	2.2	-300	···	-389(48)
004235.3+413224.4	2.4	2.6	2.5	2.7	-300	-262	-235(37)
004235.6+413149.0	3.2	2.8	2.6	2.8	-300	-312	-235(37)
004236.4+413308.7	2.6	2.6	2.5	2.7	-300	-278	-233(38)
004236.9+410158.0	2.5	2.4	2.4	2.4	-300	-413	-387(46)
004237.4+414158.3	1.8	2.1	2.1	2.3	-300	···	-227(41)
004238.6+413150.5	3.7	2.9	2.9	2.8	-300	-272	-231(39)
004238.9+413135.6	2.9	2.9	2.6	3.3	-300	-290	-231(39)
004240.1+410222.7	3.5	2.8	2.7	2.6	-300	-426	-382(44)
004240.9+405910.8	2.4	2.6	2.4	2.3	-300	-379	-383(45)
004241.3+412246.7	4.1	3.1	3.2	3.4	-300	-113	-248(30)
004241.7+411435.0	3.4	4.0	3.8	3.5	-300	···	···
004241.7+413245.4	2.5	2.7	2.5	2.5	-300	-264	-225(42)
004241.9+405155.2	3.6	3.3	3.5	3.7	-300	···	-380(44)
004242.1+410303.0	2.7	2.4	2.7	2.5	-300	-344	-377(42)
004242.5+410001.4	3.0	3.0	2.9	3.2	-300	-367	-380(44)
004242.5+413155.2	3.9	3.2	3.4	3.3	-300	-261	-226(41)
004242.6+411722.5	4.0	3.7	3.6	3.3	-300	···	-238(48)
004242.9+413159.8	3.7	3.6	3.6	3.8	-300	-262	-225(42)
004244.1+413259.2	3.4	2.5	2.9	2.9	-300	-255	-222(43)
004244.4+411608.5	3.7	3.4	3.2	3.6	-300	···	···
004244.9+413338.6	2.3	2.7	2.7	2.5	-300	-241	-220(45)
004245.0+405448.3	2.2	2.3	2.6	2.5	-300	···	-377(43)
004245.2+413316.7	2.6	2.6	2.6	2.6	-300	-253	-220(44)
004245.3+411656.9	3.6	3.6	3.8	4.0	-300	···	···

Table 2—Continued

Object	rms Noise				v_{obs}	v_{CO}	v_{HI}
	H_2O	$NH_3(1,1)$	$NH_3(2,2)$	H66α			
(J2000)	(mJy)	(mJy)	(mJy)	(mJy)	(km s^{-1})	(km s^{-1})	(km s^{-1})
004246.2+410111.4	2.4	2.3	2.4	2.1	-300	-400	-374(41)
004246.8+414447.0	2.2	2.1	2.0	2.0	-300	···	-217(45)
004247.0+411618.4	3.8	3.9	3.7	3.9	-300	···	···
004247.0+413333.0	4.0	3.1	3.3	3.1	-300	-236	-217(45)
004247.5+413131.1	2.6	2.4	2.5	2.5	-300	···	-219(44)
004247.9+413400.5	3.1	3.0	3.1	2.9	-300	-255	-216(46)
004248.2+411651.7	3.6	3.9	4.0	3.6	-300	···	···
004249.1+411554.6	3.8	3.6	4.0	3.5	-300	···	···
004249.1+411945.9	3.1	2.8	2.4	2.6	-300	···	-141(95)
004249.1+413440.0	2.3	2.7	2.6	2.5	-300	-242	-213(47)
004249.3+412507.5	3.2	2.6	2.7	2.7	-300	-167	-226(40)
004251.0+413507.8	3.2	2.6	3.0	3.0	-300	-237	-210(49)
004252.3+410014.8	2.1	2.0	2.0	1.9	-300	···	-366(38)
004252.4+410120.7	2.8	2.9	2.9	2.4	-300	-333	-364(37)
004253.0+413526.7	2.6	2.4	2.4	2.4	-300	-243	-206(50)
004253.5+413516.2	2.4	2.4	2.3	2.3	-300	-250	-207(49)
004254.4+405832.8	2.3	2.4	2.6	3.0	-300	···	-364(37)
004256.9+413728.1	1.6	1.7	1.8	1.4	-300	-291	-202(51)
004258.2+410015.9	3.1	2.5	2.5	2.8	-300	-311	-358(34)
004258.8+413456.2	1.9	2.0	2.0	2.0	-300	-223	-197(52)
004259.1+413741.3	1.9	2.2	2.1	1.9	-300	-264	-198(53)
004259.4+413722.5	2.0	2.2	2.2	1.8	-300	-260	-197(53)
004259.4+413732.1	2.0	2.1	2.1	1.8	-300	-269	-197(53)
004300.0+413526.2	2.0	2.0	2.1	1.9	-300	-200	-196(53)
004300.0+413654.2	2.5	2.4	2.3	2.1	-300	-241	-195(54)
004301.0+413627.9	1.4	1.3	1.3	1.2	-300	-248	-194(54)
004301.5+413717.2	2.8	2.6	2.7	2.6	-300	-238	-193(55)
004301.9+413655.2	1.8	2.1	2.2	1.9	-300	-224	-193(54)
004302.5+413740.5	3.5	3.3	3.2	3.7	-300	-237	-191(55)
004302.5+414910.5	2.1	2.0	2.2	2.0	-300	···	-204(51)
004303.4+413719.3	1.8	2.0	2.0	1.8	-300	-252	-191(55)
004304.3+413739.5	2.0	2.3	2.2	1.9	-300	-233	-190(55)
004304.8+410554.0	2.7	2.3	2.6	2.5	-300	-369	-337(23)
004305.7+413749.8	2.0	1.9	1.8	1.9	-300	-220	-187(56)
004306.7+410213.4	2.2	2.4	2.4	2.4	-300	···	-345(27)
004306.9+413807.1	3.3	2.6	2.8	2.9	-300	-189	-185(56)
004308.2+410156.8	1.3	1.5	1.5	1.5	-300	···	-344(26)
004309.7+413849.3	1.8	1.9	2.3	2.1	-300	-207	-181(57)
004310.0+413751.6	1.8	2.0	2.0	2.0	-300	-201	-180(57)
004310.5+410426.8	2.3	2.4	2.6	2.6	-300	-437	-336(22)
004311.1+413743.3	1.8	2.2	2.1	2.2	-300	-158	-177(57)
004311.3+410459.5	3.6	3.3	3.5	3.7	-300	-376	-334(21)
004311.6+411245.5	2.5	2.4	2.3	2.9	-300	···	-298(4)
004312.4+410125.2	2.3	2.6	2.5	2.3	-300	···	-341(24)

Table 2—Continued

Object	rms Noise				v_{obs}	v_{CO}	v_{HI}
	H_2O	$NH_3(1,1)$	$NH_3(2,2)$	H66α			
(J2000)	(mJy)	(mJy)	(mJy)	(mJy)	(km s^{-1})	(km s^{-1})	(km s^{-1})
004312.5+413747.4	1.8	2.1	2.0	2.0	-300	-88	-174(58)
004312.7+410531.5	1.2	1.3	1.3	1.4	-300	-315	-331(19)
004313.2+410632.4	2.3	2.5	2.3	2.6	-300	-332	-327(17)
004314.0+413906.3	1.9	2.5	2.4	1.9	-300	-416	-173(59)
004314.2+410033.9	2.4	2.3	2.3	2.3	-300	···	-339(24)
004315.2+414947.4	2.0	2.6	2.4	2.3	-300	···	-187(56)
004317.9+410252.8	1.5	1.4	1.4	1.5	-300	-300	-333(20)
004320.1+410611.1	1.4	1.2	1.2	1.3	-300	-334	-322(14)
004320.8+414038.5	2.1	2.3	2.2	2.1	-300	-247	-163(60)
004321.7+414033.2	2.3	2.3	2.2	2.5	-300	-286	-162(59)
004322.0+414116.5	2.1	2.2	2.1	2.0	-300	-189	-162(60)
004324.1+414124.7	2.0	1.6	1.8	1.8	-300	-209	-158(60)
004324.3+414418.7	1.9	1.7	1.7	1.9	-300	···	-165(60)
004324.4+410802.9	2.5	2.4	2.3	2.1	-300	-317	-312(9)
004325.6+410206.4	4.4	3.8	3.2	3.9	-300	···	-327(17)
004326.4+410508.4	2.4	2.3	2.3	2.1	-300	···	-320(13)
004328.2+414122.1	1.6	1.8	1.9	2.1	-300	···	-150(60)
004328.6+411818.0	3.9	4.0	3.9	3.9	-300	-299	-245(32)
004329.2+414848.0	1.2	1.4	1.5	1.4	-300	-193	-170(58)
004330.4+412757.0	2.6	2.6	2.5	2.3	-100	···	-68(20)
004330.4+414432.5	2.4	2.2	2.1	2.4	-300	-230	-153(61)
004331.2+414222.9	2.1	2.2	2.2	2.0	-300	-202	-147(59)
004331.3+414243.6	1.8	2.0	1.9	2.2	-300	-234	-147(60)
004332.1+414251.8	1.2	1.2	1.3	1.5	-300	-255	-145(60)
004332.4+414227.5	1.7	1.7	1.9	2.0	-300	-207	-145(59)
004332.5+410907.0	2.6	3.1	2.7	2.7	-300	-320	-303(4)
004333.6+411432.3	2.8	2.7	2.4	2.7	-300	-311	-274(16)
004334.9+410953.6	3.8	3.2	3.4	3.9	-300	-305	-298(4)
004338.7+411222.1	2.4	2.6	2.6	2.7	-300	-277	-285(10)
004339.1+411018.4	2.5	2.5	2.8	3.1	-300	-314	-294(5)
004339.3+411001.1	2.8	2.9	2.7	2.6	-300	-302	-296(5)
004339.4+412229.2	2.3	2.3	2.3	2.3	-300	···	-206(46)
004339.7+414534.9	2.0	2.3	2.1	2.3	-300	-118	-137(61)
004340.8+411152.7	2.6	2.4	2.7	2.6	-300	-276	-286(9)
004341.5+414224.3	2.5	2.5	2.6	2.2	-300	···	-127(54)
004341.6+411135.3	2.8	2.5	2.5	2.5	-300	-304	-288(9)
004341.7+412302.9	2.5	2.7	2.6	2.3	-300	-211	-196(49)
004341.7+414519.4	2.0	1.6	1.6	1.7	-300	-152	-132(60)
004341.7+415313.0	2.0	2.4	2.2	2.0	-300	···	-161(59)
004343.4+414521.6	2.1	2.1	2.3	2.2	-300	-135	-131(59)
004343.9+411137.6	1.3	1.2	1.4	1.1	-300	-285	-287(9)
004344.6+412321.3	2.4	2.4	2.4	2.6	-300	-111	-192(51)
004346.3+414418.5	3.8	3.3	3.3	3.5	-300	-183	-121(55)
004346.8+411239.7	2.9	2.6	2.4	2.7	-300	-258	-281(12)

Table 2—Continued

Object	rms Noise				v_{obs}	v_{CO}	v_{HI}
	H_2O	$NH_3(1,1)$	$NH_3(2,2)$	H66α			
(J2000)	(mJy)	(mJy)	(mJy)	(mJy)	(km s^{-1})	(km s^{-1})	(km s^{-1})
004348.1+411133.2	3.2	2.9	3.0	3.0	-300	-282	-285(10)
004349.0+415657.7	3.6	4.1	4.1	4.1	-300	-199	-153(62)
004349.4+411053.8	2.4	2.2	2.1	2.1	-300	···	-288(8)
004351.4+414706.2	3.5	3.7	3.8	4.0	-300	-165	-118(58)
004351.4+415718.7	2.1	2.4	2.4	1.9	-300	-226	-151(62)
004352.5+412524.1	2.8	2.6	2.7	3.1	-100	-178	-177(53)
004352.5+414858.8	2.3	2.4	2.5	2.1	-300	···	-125(59)
004353.9+415743.8	1.8	2.2	2.2	2.0	-300	-174	-148(62)
004354.8+414715.6	2.9	2.5	2.6	2.5	-300	-413	-115(55)
004354.9+412603.6	3.2	2.4	2.7	2.7	-100	-144	-169(55)
004355.1+411433.1	2.4	2.2	2.4	2.4	-300	-240	-269(19)
004355.2+412650.8	3.0	3.2	2.8	2.8	-100	-165	-161(54)
004355.8+411211.6	4.1	3.5	3.0	3.9	-300	-229	-281(12)
004356.6+412629.6	2.4	2.1	2.0	1.8	-100	-139	-166(55)
004356.8+414831.6	3.6	3.4	3.5	3.8	-300	-165	-113(56)
004357.7+414854.0	3.1	2.6	2.8	2.6	-300	-164	-113(56)
004358.2+414726.9	3.0	2.3	2.6	2.3	-300	-121	-108(52)
004358.7+414837.5	3.0	2.5	2.6	2.4	-300	-119	-110(55)
004358.9+411742.1	2.6	2.4	2.5	2.1	-300	-267	-249(30)
004401.5+414909.6	3.8	3.6	3.6	3.3	-300	-160	-106(54)
004403.0+414954.7	3.1	2.9	2.8	2.4	-300	-153	-107(54)
004403.4+411708.2	2.2	2.3	2.3	2.5	-300	-287	-254(27)
004403.9+413414.8	3.4	2.7	2.8	2.6	-100	···	-96(20)
004404.2+412107.8	2.5	2.3	2.2	2.6	-300	-261	-227(41)
004404.9+415016.1	2.8	2.7	2.6	2.9	-300	-168	-105(53)
004405.2+412718.2	2.8	2.4	2.8	2.9	-100	-112	-173(54)
004405.7+411719.7	2.3	2.9	2.5	2.4	-300	-260	-253(28)
004406.4+412745.0	2.9	2.6	2.8	2.4	-100	-137	-169(54)
004407.0+412759.3	3.3	2.8	3.0	3.0	-100	-140	-167(54)
004407.8+412110.7	3.0	2.7	2.7	2.6	-300	-243	-226(42)
004409.2+413331.9	2.4	2.3	2.3	2.3	-100	-91	-104(33)
004409.5+411856.6	1.2	1.3	1.3	1.3	-300	-257	-243(33)
004410.5+420247.5	2.9	2.7	3.0	2.6	-100	···	-138(61)
004410.6+411653.4	2.2	2.4	2.4	2.3	-300	-122	-256(26)
004411.0+413206.3	2.1	2.4	2.5	2.5	-100	-123	-121(45)
004411.8+414747.5	2.2	2.3	2.1	1.8	-100	···	-84(37)
004411.9+413356.4	2.1	2.3	2.2	2.3	-100	-108	-101(34)
004412.1+413320.5	2.8	3.1	2.7	2.8	-100	-102	-109(39)
004413.7+413413.5	2.2	2.2	2.4	2.2	-100	-81	-102(35)
004414.4+411742.3	2.4	2.7	2.4	2.3	-300	-258	-252(28)
004414.6+412840.3	2.3	2.5	2.5	2.7	-100	-115	-167(56)
004415.3+411905.7	2.9	2.5	3.8	2.7	-300	-232	-244(33)
004415.9+411717.6	2.1	2.2	2.4	2.2	-300	-267	-255(27)
004416.0+414950.7	3.1	2.7	3.0	2.7	-100	···	-84(40)

Table 2—Continued

Object	rms Noise				v_{obs}	v_{CO}	v_{HI}
	H_2O	$NH_3(1,1)$	$NH_3(2,2)$	H66α			
(J2000)	(mJy)	(mJy)	(mJy)	(mJy)	(km s^{-1})	(km s^{-1})	(km s^{-1})
004416.1+412105.4	2.3	2.4	2.5	2.2	-300	-240	-231(39)
004416.3+411730.9	2.4	2.6	2.4	2.4	-300	-238	-254(28)
004416.7+412444.1	2.1	2.3	2.2	2.1	-300	-257	-203(51)
004418.2+413406.6	2.8	2.8	2.8	2.8	-100	-148	-112(41)
004419.2+411930.9	2.9	2.5	2.5	2.7	-300	-234	-243(33)
004419.3+412247.0	2.4	2.6	2.5	2.5	-300	-247	-219(44)
004419.9+412201.2	3.2	2.7	2.5	2.7	-300	-259	-226(42)
004420.2+415101.5	3.4	2.5	2.6	2.8	-100	-232	-82(38)
004420.7+411751.0	2.3	2.6	2.7	2.2	-300	-389	-253(28)
004420.9+411835.7	2.5	2.5	2.5	2.4	-300	-247	-249(30)
004422.8+412529.1	2.1	2.3	2.2	2.1	-300	-228	-199(52)
004423.0+412050.9	3.3	2.9	3.0	2.7	-300	-246	-235(37)
004423.3+413842.6	2.8	2.6	3.0	2.7	-100	···	-79(17)
004423.7+412437.3	3.3	2.5	2.5	2.6	-300	-224	-208(49)
004424.1+412117.3	2.9	2.8	2.7	2.9	-300	-198	-232(39)
004424.2+414918.9	3.2	2.4	2.5	2.7	-100	-93	-69(26)
004424.4+415120.5	1.7	2.0	2.1	2.0	-100	-160	-76(34)
004424.9+413739.1	2.1	2.1	1.9	1.8	-100	-51	-93(26)
004425.0+414942.6	1.8	2.2	2.1	1.9	-100	-91	-70(27)
004425.4+415006.1	1.8	2.2	2.1	2.1	-100	···	-71(28)
004426.2+412054.1	2.4	2.1	2.1	2.0	-300	-222	-236(36)
004426.7+412729.3	2.4	2.3	2.2	2.2	-300	-213	-186(56)
004427.5+413529.8	3.0	2.5	2.7	2.5	-100	···	-112(44)
004429.1+412334.0	3.2	2.5	2.8	2.6	-300	-217	-219(45)
004429.6+412138.9	2.1	2.1	2.1	2.2	-300	-283	-233(38)
004429.6+415133.5	1.9	2.0	1.9	2.0	-100	-109	-68(29)
004430.2+415242.7	2.0	2.1	2.3	2.0	-100	-103	-69(33)
004430.5+415154.8	1.1	1.1	1.1	1.2	-100	-92	-68(29)
004431.1+415110.2	3.0	2.6	2.9	3.0	-100	-93	-67(25)
004431.1+415638.2	1.9	2.0	2.1	1.9	-100	-90	-87(43)
004431.9+412233.3	2.9	2.6	2.7	2.6	-300	-181	-228(40)
004431.9+412400.1	2.2	2.2	2.0	4.5	-300	-215	-217(45)
004432.6+412518.7	2.2	2.3	2.3	2.4	-300	-190	-209(49)
004433.8+415249.7	2.3	2.1	1.9	2.1	-100	-82	-63(29)
004435.6+415606.9	3.1	2.6	2.6	2.8	-100	-135	-78(37)
004436.7+412445.1	2.3	2.9	2.6	2.5	-300	-217	-216(46)
004437.3+415350.2	1.9	2.1	2.3	1.9	-100	-131	-63(29)
004437.7+415259.8	2.1	2.4	2.3	2.4	-100	-114	-63(24)
004437.9+415154.0	3.8	2.5	2.7	2.6	-100	-131	-61(20)
004438.5+412511.1	3.7	3.4	3.3	3.6	-300	-204	-214(47)
004439.4+415251.3	2.2	2.4	2.2	2.3	-100	-105	-60(22)
004440.3+414923.9	1.9	2.2	2.2	2.0	-100	···	-56(13)
004441.5+415312.7	1.9	2.0	2.2	1.9	-100	-98	-58(21)
004441.7+412659.6	2.1	2.4	2.1	2.2	-300	-201	-202(51)

Table 2—Continued

Object	rms Noise				v_{obs}	v_{CO}	v_{HI}
	H_2O	$NH_3(1,1)$	$NH_3(2,2)$	H66α			
(J2000)	(mJy)	(mJy)	(mJy)	(mJy)	(km s^{-1})	(km s^{-1})	(km s^{-1})
004442.7+415341.1	1.3	1.4	1.4	1.3	-100	-63	-55(23)
004443.9+412758.0	3.9	3.3	3.9	3.6	-300	-186	-196(53)
004444.1+415359.0	3.3	2.5	2.6	2.7	-100	-70	-54(22)
004444.8+412839.9	2.6	2.4	2.6	2.6	-300	-196	-192(54)
004447.1+415657.7	2.5	2.5	2.3	2.2	-100	···	-64(26)
004447.6+412641.5	2.5	2.5	2.5	2.5	-300	-219	-210(48)
004448.1+415307.3	2.3	2.5	2.4	2.4	-100	-87	-51(16)
004448.4+412254.2	3.1	3.0	2.9	2.7	-300	···	-230(40)
004448.6+415343.6	2.3	2.5	2.5	2.3	-100	-86	-52(17)
004450.6+415608.3	2.3	2.3	2.3	2.0	-100	-69	-54(22)
004450.9+412909.2	2.2	2.4	2.3	2.3	-300	-175	-194(53)
004451.8+415423.7	1.2	1.3	1.4	1.3	-100	-109	-47(18)
004452.7+415309.1	1.3	1.5	1.4	1.5	-100	-58	-48(15)
004452.8+415457.5	2.3	2.1	2.0	2.3	-100	-87	-48(18)
004453.0+415340.3	3.0	2.9	2.8	3.0	-100	-95	-49(15)
004454.4+420327.4	1.8	2.0	2.2	2.1	-100	···	-85(37)
004456.1+412918.2	3.2	2.9	2.8	2.7	-300	-178	-198(52)
004456.2+413124.1	2.5	2.3	2.0	2.1	-300	-159	-182(57)
004457.2+415524.0	3.1	2.7	2.6	2.6	-100	-69	-46(17)
004457.3+413141.8	2.1	2.4	2.4	1.9	-300	-160	-181(57)
004458.0+414034.7	1.3	1.6	1.4	1.3	-100	-106	-104(51)
004458.1+420008.6	2.3	2.2	2.3	2.3	-100	-112	-62(25)
004458.3+415906.9	2.4	2.4	2.4	2.2	-100	···	-58(21)
004458.7+415536.1	2.1	1.9	1.7	3.2	-100	-77	-45(16)
004459.1+413233.8	4.2	3.3	4.8	3.3	-300	-136	-174(59)
004459.1+414058.5	3.1	2.7	2.8	2.9	-100	-109	-102(50)
004459.3+413139.2	2.9	2.2	2.4	2.5	-300	-171	-183(56)
004459.5+415510.4	2.4	2.6	2.3	2.4	-100	-64	-43(16)
004500.7+412836.9	4.1	3.2	3.3	3.4	-300	-170	-205(50)
004500.9+413101.1	3.0	2.8	2.8	2.9	-300	···	-190(54)
004503.0+413249.4	2.0	2.3	2.1	1.9	-300	-145	-178(57)
004504.6+413237.6	1.8	2.1	2.4	2.0	-300	-135	-181(56)
004505.3+413845.9	2.3	2.5	2.4	2.7	-100	···	-130(59)
004505.9+413925.5	2.2	2.4	2.3	2.3	-100	-127	-124(59)
004506.1+413615.0	2.1	1.9	1.9	1.8	-100	-150	-152(61)
004506.1+415121.0	3.4	2.7	3.8	2.6	-100	-48	-47(15)
004506.2+413424.4	3.0	2.6	2.6	2.7	-100	-137	-168(59)
004506.9+413407.8	2.8	2.7	2.7	2.7	-100	-142	-172(58)
004507.5+413439.4	2.1	2.4	2.4	2.4	-100	-140	-168(59)
004508.2+413424.2	2.2	2.5	2.3	2.4	-100	-128	-171(58)
004509.0+415209.7	3.3	2.7	2.6	2.7	-100	-57	-47(14)
004510.0+420143.6	2.3	2.7	2.4	2.5	-100	-89	-54(18)
004510.3+420228.5	2.6	2.5	2.5	2.6	-100	···	-56(20)
004510.4+413716.0	1.9	2.2	2.2	2.1	-100	-100	-149(61)

Table 2—Continued

Object	rms Noise				v_{obs}	v_{CO}	v_{HI}
	H_2O	$NH_3(1,1)$	$NH_3(2,2)$	H66α			
(J2000)	(mJy)	(mJy)	(mJy)	(mJy)	(km s^{-1})	(km s^{-1})	(km s^{-1})
004510.5+413426.7	2.4	2.4	2.2	2.5	-100	-117	-173(58)
004510.8+415938.9	2.3	2.3	2.2	2.1	-100	···	-48(13)
004511.2+413644.9	3.3	2.7	2.5	2.6	-100	-113	-156(60)
004511.3+413633.9	2.7	2.7	2.9	2.6	-100	-130	-157(60)
004511.6+420130.3	2.0	2.1	2.4	2.1	-100	···	-52(17)
004512.1+415542.5	1.9	2.0	2.2	2.0	-100	-58	-40(15)
004512.4+413709.6	3.2	2.7	2.8	2.6	-100	-133	-154(60)
004512.8+413531.6	2.4	1.9	2.1	2.0	-100	-133	-168(59)
004514.4+413723.6	2.5	2.4	2.3	2.6	-100	-108	-154(60)
004515.2+413948.5	3.1	2.5	2.6	2.5	-100	···	-134(60)
004515.9+420254.4	2.3	2.4	2.3	2.3	-100	···	-52(16)
004518.1+413920.5	2.2	2.5	2.6	2.2	-100	-64	-143(60)
004518.5+414013.2	2.1	2.1	2.1	1.8	-100	···	-135(60)
004518.7+413906.1	2.2	2.1	2.4	2.2	-100	···	-146(60)
004518.8+420331.8	1.2	1.4	1.3	1.5	-100	-69	-55(15)
004520.7+414716.7	3.1	2.5	2.8	2.5	-100	-112	-82(41)
004520.9+414248.8	2.3	2.2	2.3	1.9	-100	-78	-117(56)
004521.6+420345.1	2.3	2.3	2.4	2.3	-100	-62	-53(14)
004523.1+414346.0	2.0	2.0	2.1	2.3	-100	-99	-113(55)
004524.4+415537.4	2.1	1.8	2.1	3.6	-100	-78	-44(14)
004526.8+415820.1	2.6	2.0	2.1	2.6	-100	···	-43(12)
004527.0+415135.5	1.8	2.4	2.2	2.0	-100	···	-63(27)
004528.0+415928.1	2.6	2.6	2.3	2.3	-100	-26	-42(11)
004528.2+414513.6	3.1	2.8	2.4	2.8	-100	-88	-108(53)
004528.2+414630.6	1.7	2.1	2.3	2.1	-100	-85	-99(49)
004528.6+415000.2	2.1	2.0	2.3	2.0	-100	-59	-75(35)
004532.2+414543.3	2.0	2.5	2.2	1.9	-100	-86	-110(54)
004533.3+414739.8	2.0	2.4	2.3	2.1	-100	-57	-97(48)
004533.6+414728.2	2.3	2.3	2.4	2.5	-100	-66	-99(49)
004534.1+414703.3	2.3	2.5	2.2	2.5	-100	-5	-103(51)
004536.3+414252.0	2.1	2.3	2.3	2.4	-100	-129	-140(59)
004536.5+415307.7	2.2	2.0	2.2	2.0	-100	-74	-67(28)
004536.9+415704.0	3.2	2.7	2.7	2.4	-100	-69	-50(14)
004537.2+415802.4	2.9	2.6	2.8	3.0	-100	-40	-47(13)
004537.3+415107.0	3.2	2.9	2.7	2.6	-100	···	-79(38)
004537.6+415424.1	3.2	2.8	3.1	2.8	-100	-63	-61(24)
004538.5+415231.1	3.2	2.9	2.9	2.4	-100	-41	-72(33)
004540.0+415510.2	3.2	2.7	2.5	2.9	-100	-55	-60(23)
004541.4+415550.4	1.9	2.0	2.0	2.2	-100	-55	-58(22)
004541.6+415107.7	3.3	2.5	2.6	2.6	-100	-82	-84(41)
004542.9+415234.8	2.5	2.0	2.0	2.0	-100	-63	-77(36)
004543.3+415109.3	1.1	1.2	1.2	1.2	-100	-124	-89(42)
004543.3+415301.1	3.0	2.7	2.6	2.7	-100	-53	-75(35)
004543.5+414235.1	2.0	2.3	2.0	2.0	-100	···	-147(60)

Table 2—Continued

Object	rms Noise				v_{obs}	v_{CO}	v_{HI}
	H_2O	$NH_3(1,1)$	$NH_3(2,2)$	H66α			
(J2000)	(mJy)	(mJy)	(mJy)	(mJy)	(km s^{-1})	(km s^{-1})	(km s^{-1})
004544.3+415207.4	3.1	2.9	2.8	2.8	-100	-6	-84(39)
004549.7+421017.1	2.3	2.3	2.4	2.0	-100	···	-53(12)
004555.2+415645.8	2.1	2.2	2.5	2.1	-100	···	-72(29)
004608.5+421131.0	2.9	2.6	3.0	2.7	-100	···	-48(10)
004613.4+415224.4	2.1	2.5	2.4	2.2	-100	-93	-110(56)
004617.6+415158.0	3.4	2.7	2.7	2.8	-100	-83	-117(58)
004623.9+421215.2	2.1	2.4	2.5	2.5	-100	···	-42(10)
004625.4+421156.0	2.2	2.3	2.3	2.3	-100	···	-42(10)
004626.0+421121.7	2.2	2.3	2.2	2.3	-100	···	-43(11)
004627.9+415920.4	2.2	2.4	2.3	2.2	-100	···	-85(45)
004631.5+421342.6	2.4	2.5	2.4	2.3	-100	···	-38(10)
004633.4+421244.2	2.5	2.3	2.4	2.2	-100	···	-40(11)
004633.6+415932.0	3.0	2.8	2.8	2.8	-100	···	-91(47)
004634.2+415636.8	1.9	2.1	2.2	2.1	-100	···	-111(54)
004634.4+421143.1	2.4	2.0	2.0	1.9	-100	···	-42(12)
004641.6+421156.2	3.2	2.7	2.7	2.6	-100	···	-46(15)
004641.9+421547.8	2.3	2.4	2.5	2.4	-100	···	-40(11)
004642.2+415837.3	2.4	2.5	2.3	2.3	-100	···	-113(52)
004642.6+421406.8	2.4	2.5	2.5	2.6	-100	···	-42(12)
004645.9+420453.1	2.2	2.2	2.3	2.3	-100	···	-76(39)
004654.5+420046.2	2.3	2.2	2.6	2.2	-100	···	-118(50)
004703.1+415755.4	2.3	2.3	2.5	2.3	-100	···	-145(53)

Note. — The average rms noise is (2.5 ± 0.6) mJy. Detected H_2O maser regions are in bold. 1σ v_{CO} uncertainties are typically $\sim$1 km s^{-1} (Nieten et al. 2006). v_{HI} 1σ uncertainties (Chemin et al. 2009) are listed in parenthesis next to v_{HI} values. Also note that the listed v_{CO} values are in the Local Standard of Rest (LSR) frame, but each v_{CO} value was converted from LSR to barycentric (BAR) radial velocity to be used with spectra in the stacking procedure, already in BAR velocity. The LSR frame is a reference frame which is centered on the Solar motion around the Galactic center in an assumed perfectly circular orbit (see, e.g., Carrol & Ostlie 2006, §24.3, pg. 903). BAR velocity is measured in the barycenter (center of mass) reference frame of the Solar System.

3. Detection Heuristics

During and after the data reduction process, we used a number of heuristics to determine if a potential emission or absorption line feature was real:

- The Gaussian smoothed $\left(244\frac{\text{kHz}}{\text{channel}}\right)$ spectrum for each source contains 186 channels (i.e., spectral x-axis values), so for 506 sources, there are a total of 94,116 channels that random noise can "fall on." Assuming the spectral noise is Gaussian, if a potential signal is below 4.6σ it is possible to that the "signal" is a result of observing Gaussian noise:

$$94116\left(1-\frac{1}{\sqrt{2\pi}}\int_{-4.5}^{4.5}e^{-\left(x^2/2\right)}\,dx\right)\approx 0.6>0.5,\ \text{but} \tag{24}$$

$$94116\left(1-\frac{1}{\sqrt{2\pi}}\int_{-4.6}^{4.6}e^{-\left(x^2/2\right)}\,dx\right)\approx 0.4<0.5 \tag{25}$$

- It is also important to check the pre-smoothed spectrum for each source in order to catch potential emission or absorption features that may disappear after smoothing (e.g., averaging a one channel wide peak over 10 channels will create one smoothed channel, removing the prior evidence of a narrow peak). Thus, the same heuristic applies to the pre-Gaussian smoothed $\left(12.2\frac{\text{kHz}}{\text{channel}}\right)$ spectra, which contain 2,048 channels per spectrum, or a total of 1,036,288 channels. Assuming the spectral noise is Gaussian, if a potential signal is below 5.1σ it is possible that the "signal" is a result of observing Gaussian noise:

$$1036288\left(1-\frac{1}{\sqrt{2\pi}}\int_{-5.0}^{5.0}e^{-\left(x^2/2\right)}\,dx\right)\approx 0.6>0.5,\ \text{but} \tag{26}$$

$$1036288\left(1-\frac{1}{\sqrt{2\pi}}\int_{-5.1}^{5.1}e^{-\left(x^2/2\right)}\,dx\right)\approx 0.4<0.5 \tag{27}$$

- Observing both polarizations: if the two polarizations look significantly different from one another, or if the feature appears in one polarization but not the other, a different polarized light source within the GBT beam may be interfering with the spectral data for the compact 24 μm M31 source. In general, we do not expect to observe the presence of strong magnetic fields in molecular, star-forming regions (J. Darling, private communication). Figure 9 shows an example $NH_3(2,2)$ spectrum with a potential signal at the same velocity only in the right polarization and averaged polarization spectra (but not in the left polarization), indicating that the signal is not real.

- Compare the doppler velocity of the potential feature with the M31 CO velocity (or HI velocity if there is not CO coverage) at the same location as the observed source.

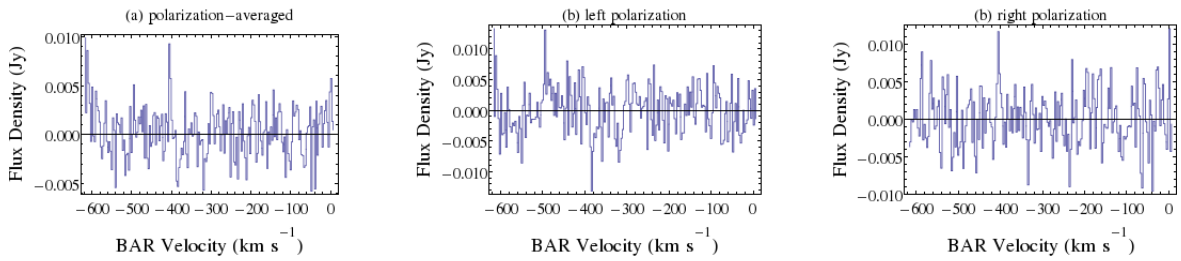

Fig. 9.— (a) An example of a polarization-averaged $NH_3(2,2)$ spectrum for 004229.8+410550.6 with an apparent 3.7σ signal (a). This signal is not at the same velocity in the left polarization (b) as the signal in the right polarization (c), indicating that the signal is not real.

If the feature is real, these two velocities should be similar to one another. Figure 10 shows an example H66α spectrum of a potential emission feature present in both polarizations but outside the CO velocity range, indicating that the feature is not real.

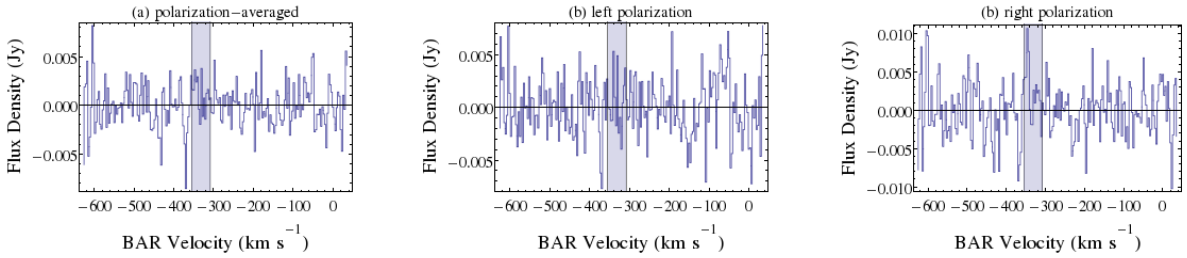

Fig. 10.— An example of a polarization-averaged H66α spectrum for 004324.4+410802.9 with an apparent -4.0σ signal (a). Signals are also present in both the left (b) and right (c) polarizations. The shaded region shows the range of CO velocity within the GBT beam, indicating that the signal is not real.

- We expect to see both $NH_3(1,1)$ and $NH_3(2,2)$ emission at similar velocities if the signal is real and the sensitivity can detect both lines. In general, we can describe the two populations of $NH_3(1,1)$ and $NH_3(2,2)$ with a Boltzmann distribution (Henkel et al. 2000):

$$\frac{S_{\mathrm{NH_3(2,2)}}}{S_{\mathrm{NH_3(1,1)}}} \propto \frac{N_{\mathrm{NH_3(2,2)}}}{N_{\mathrm{NH_3(1,1)}}} = \frac{g_{(2,2)}}{g_{(1,1)}} e^{-\frac{h\nu}{k_b T_{\mathrm{rot}}}}, \tag{28}$$

where $S_{\mathrm{NH_3(1,1)}}$ & $N_{\mathrm{NH_3(1,1)}}$, $S_{\mathrm{NH_3(2,2)}}$ & $N_{\mathrm{NH_3(2,2)}}$, and $g_{(1,1)}$ & $g_{(2,2)}$ are the line intensities, number densities, and degeneracy configurations for $NH_3(1,1)$ and $NH_3(2,2)$,

respectively, $h\nu$ is the energy difference between the $NH_3(1,1)$ and $NH_3(2,2)$ inversion states, k_b is Boltzmann's constant, and $T_{\rm rot}$ is the rotational temperature of NH_3 in the surrounding region. Equation 28 indicates that $NH_3(1,1)$ and $NH_3(2,2)$ emission should both be present if $NH_3(1,1)$ emission is high enough above the spectral noise limit (i.e., if $NH_3(1,1)$ is apparent as a weak signal, then $NH_3(2,2)$ may not be visible because it is below the spectral noise limit, and thus other detection heuristics must be used).

4. Results

4.1. Individual Spectra

The detection of five H_2O masers in the first 206 observed regions is discussed in Darling (2011). We detect no additional H_2O masers in the follow up survey of 300 24 μm sources. We detect no $NH_3(1,1)$, $NH_3(2,2)$, or H66α in in any of the observed 506 24 μm sources. The average rms noise in non-detection spectra with 244 kHz channels is (2.5±0.6) mJy. Non-detection spectra generally did not show any features greater than 3σ. A number of detection heuristics (e.g., presence in both polarizations, Gaussian noise limits, agreement with CO velocity, presence of both $NH_3(1,1)$ and $NH_3(2,2)$; see §3) showed that features greater than 3σ were not real.

4.2. Stacked Spectra

4.2.1. $NH_3(1,1)$

We detect no signal in the $NH_3(1,1)$ mean and median stacks, shown in Figure 11. The measured rms noise[30] in the mean and median stacks are 0.12 mJy and 0.15 mJy, respectively. Compared to the average (2.5±0.6) mJy rms noise in an individual spectrum (see Table 2), the rms noise in the mean and median stacks both agree with theoretical $\sqrt{N}$

[30]Note that in each stack for $NH_3(1,1)$, $NH_3(2,2)$, H66α, and H_2O, we calculate the rms noise in only the central 50% of each spectrum. Upon shifting and centering each individual spectrum to $v_{\rm CO}$ or $v_{\rm HI}$ (but still keeping the same bandwidth), a portion of the shifted spectra no longer has data (∼25% on either the blue or red side). Thus, the noise on the edges of each stacked spectrum should be greater than the noise in the center, since *less* than $\sqrt{N}$ spectra are being averaged/medianed on the edges.

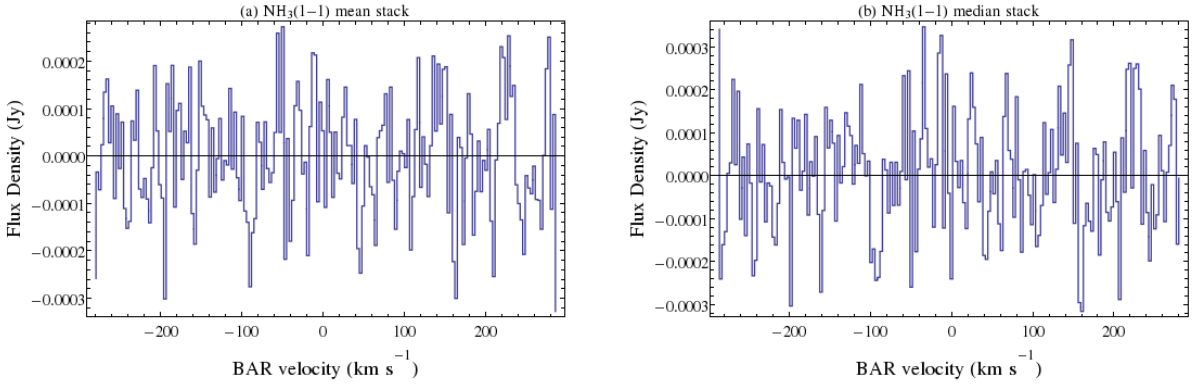

Fig. 11.— A plot of the $NH_3(1,1)$ mean (a) and median (b) stacks.

noise reduction:

$$\frac{(2.5 \pm 0.6)\text{mJy}}{\sqrt{446}} = (0.12 \pm 0.03)\ \text{mJy} \tag{29}$$

4.2.2. $NH_3(2,2)$

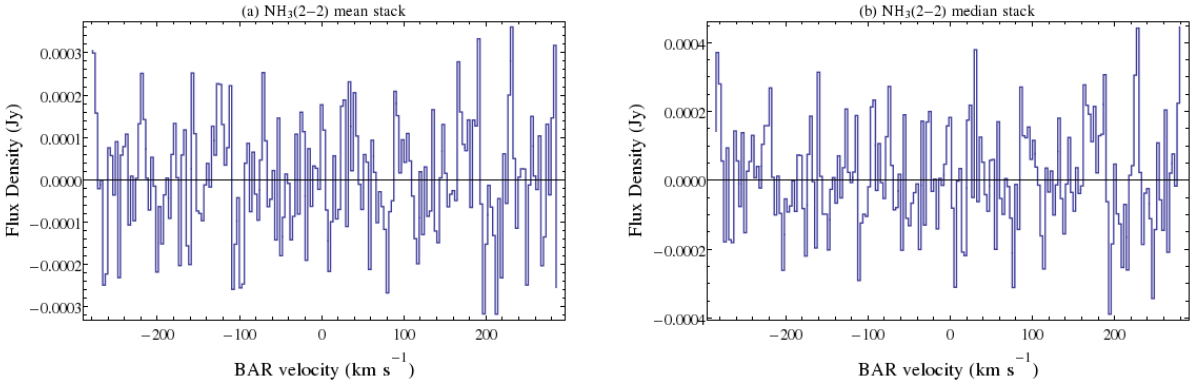

Fig. 12.— A plot of the $NH_3(2,2)$ mean (a) and median (b) stacks.

We detect no signal in the $NH_3(2,2)$ mean and median stacks, shown in Figure 12. The rms noise in the mean and median stacks are 0.10 mJy and 0.13 mJy, respectively, and thus both agree with $\sqrt{N}$ noise reduction in equation 29.

4.2.3. H66α

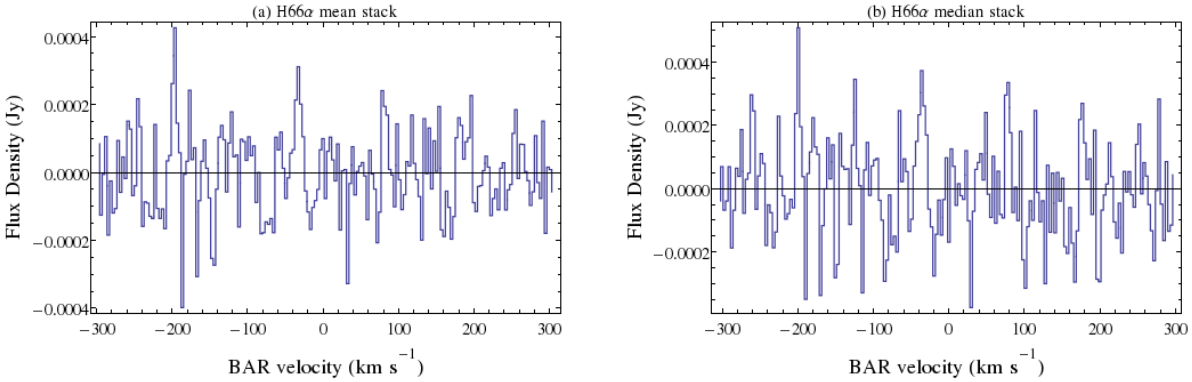

Fig. 13.— A plot of the H66α mean (a) and median (b) stacks.

We detect no signal in the H66α mean and median stacks, shown in Figure 13. The rms noise in the mean and median stacks are 0.12 mJy and 0.15 mJy, respectively, both in agreement with $\sqrt{N}$ noise reduction in equation 29. It is also worth noting that the large peak on the right (blue) edge of the H66α mean and median stacks is consistent with noise reduction *less than* $\sqrt{N}$, as explained in footnote 30.

4.2.4. H_2O

We detect no signal in the H_2O mean and median stacks, shown in Figure 14. The rms noise in the mean and median stacks are 0.12 mJy and 0.13 mJy, respectively, and thus both agree with $\sqrt{N}$ noise reduction[31] in equation 29.

We also did a subset, or bootstrap, mean and median stack of the 50 brightest observed 24 μm sources (Gordon et al. 2006), shown in Figure 15. If a signal were present in the bootstrap stack but not the total stack, this would indicate that only the brighter 24 μm sources, or dustier M31 GMCs, typically contain H_2O above the observed sensitivity limit in the bootstrap stack. However, we detect no signal in the bootstrap H_2O mean and median stacks. The rms noise in the bootstrap mean and median stacks is 0.38 mJy and 0.42 mJy, respectively, and thus both agree with $\sqrt{N}$ noise reduction: $\frac{(2.5\pm0.6)\text{mJy}}{\sqrt{50}} = (0.35\pm0.08)$ mJy.

[31]Although the H_2O stacks included 441 sources instead of 446 sources (see footnote 29), to two significant figures, $\frac{(2.5\pm0.6)\text{mJy}}{\sqrt{441}} = \frac{(2.5\pm0.6)\text{mJy}}{\sqrt{446}} = (0.12 \pm 0.3)$ mJy

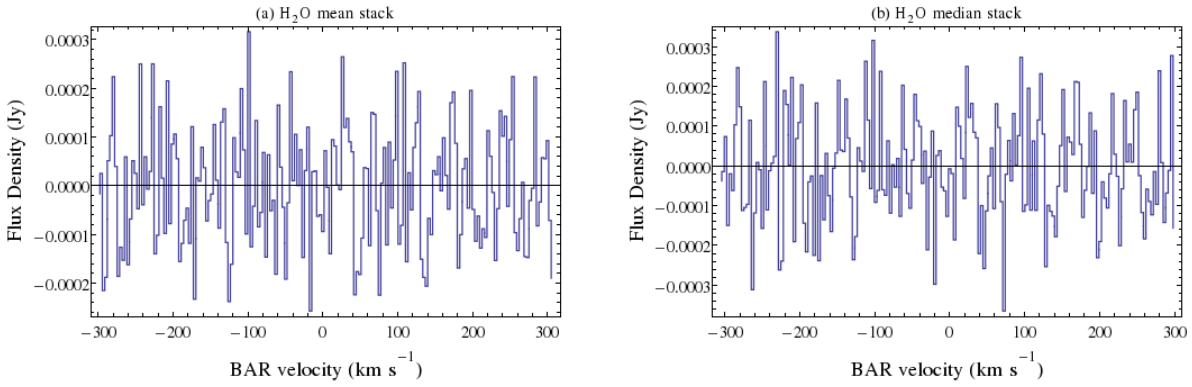

Fig. 14.— A plot of the H_2O mean (a) and median (b) stacks.

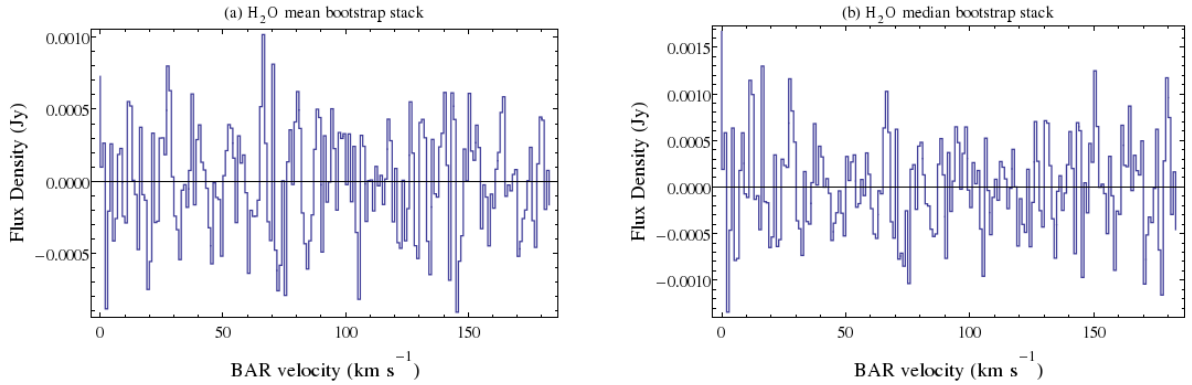

Fig. 15.— A plot of the H_2O mean (a) and median (b) stacks of the brightest 50 24 μm sources.

5. NH_3 Analysis

5.1. NH_3(1,1) Integrated Flux Comparison

Using the non-detection from the $NH_3(1,1)$ stack, we can estimate a 3σ upper limit on the typical $NH_3(1,1)$ integrated flux, $\int NH_3(1,1)dv$, from an M31 GMC[32]. $\int NH_3(1,1)dv$ is an integral over the $NH_3(1,1)$ line profile, and thus an effective measurement of the total energy carried in the $NH_3(1,1)$ emission line. One channel width in the $NH_3(1,1)$ stacked

[32]Because of our resulting non-detection, we can use our rms noise in the $NH_3(1,1)$ stack $\left(\text{rms noise}_{NH_3(1,1)\text{ stack}}\right)$ to set an upper limit on a 3σ $NH_3(1,1)$ detection in a M31 GMC at a value less than or equal to $3\left(\text{rms noise}_{NH_3(1,1)\text{ stack}}\right)$.

spectrum is[33] 3.1 km s^{-1}, and the conversion from flux density, S, to main beam brightness temperature[34], T_{MB}, is[35] $T_{MB} = 2.16\frac{K}{Jy}(S)$, and so we used the rms noise from the $NH_3(1,1)$ mean stack shown in Figure 11 (a) and an assumed typical Gaussian line width (i.e., the width of the peak at half it's maximum value, or FWHM) of 25 km s^{-1} (C. Battersby, A. Ginsburg, private communication)[36] to determine

$$\log_{10}\left(\int_{\rm mean} NH_3(1,1)dv\left[\text{K km s}^{-1}\right]\right) \leq -1.7 \tag{30}$$

and the same assumption for the $NH_3(1,1)$ median stack, shown in Figure 11 (b), to determine

$$\log_{10}\left(\int_{\rm median} NH_3(1,1)dv\left[\text{K km s}^{-1}\right]\right) \leq -1.6 \tag{31}$$

We separately obtained the MW $\int NH_3(1,1)dv$ data presented in Longmore et al. 2013 (S. Longmore, private communication), which shows $\int NH_3(1,1)dv$ values over 2° Galactic longitude bins[37]. We used this data to compute the $\int NH_3(1,1)dv$ of each MW GMC placed at the distance of M31 (McConnachie et al. 2005) using the corresponding near and far distance[38] data, d_{near} and d_{near}, respectively (S. Longmore, private communication):

$$\int_{\rm MW\rightarrow M31} NH_3(1,1)dv = \left(\frac{d_{\rm MW\ GMC}}{d_{\rm M31}}\right)^2 \int_{\rm MW} NH_3(1,1)dv, \tag{32}$$

---

[33]We can rearrange equation 11 to show that $v_{\rm obs} = \left(\frac{f_{\rm obs}-f_{\rm rest}}{f_{\rm obs}}\right)c$, or $\Delta v = \left(\frac{\Delta f}{f_{\rm obs}}\right)c$, where Δf is the channel width for a spectrum in frequency space and Δv is the channel width for a spectrum in velocity space. Thus, an identical post-smoothed channel width in frequency space yields a non-identical post-smoothed channel width in velocity space because $\left(\frac{\Delta f}{f_{\rm obs}}\right)$ is different for different ovserved lines (e.g., H_2O and H66α both have a ∼3.3 km s^{-1} post-smoothed channel width, but $NH_3(1,1)$ and $NH_3(2,2)$ both have a ∼3.1 km s^{-1} post-smoothed channel width).

[34]In radio astronomy, the main beam brightness temperature is the temperature that a blackbody would have to be at in order to duplicate the observed brightness of an object at the observed frequency (Burke & Graham-Smith 2010, pg. 14).

[35]see the GBT Spectral Line Calibration Manual: www.gb.nrao.edu/GBT/DA/gbtidl/gbtidl_calibration.pdf

[36]The typical MW $NH_3(1,1)$ line width is ∼1 km s^{-1} (e.g., Dunham et al. 2011) whereas the typical $NH_3(1,1)$ line width in distant galaxies is ∼250 km s^{-1} (e.g., Ao et al. 2011), and thus a typical M31 $NH_3(1,1)$ line width should lie in between these two extremes.

[37]2° bins in the Galaxy are of comparable physical size (100-200pc) to the 33" beam in M31 (125 pc), both approximately covering the physical diameter of a GMC.

[38]The near/far distance ambiguity in astronomy refers to the ambiguity for a distance determination method within the MW disk. We can compare the measured radial velocity of any observed object in the MW disk to the MW rotation curve to determine its near and far distance, shown in Figure 16.

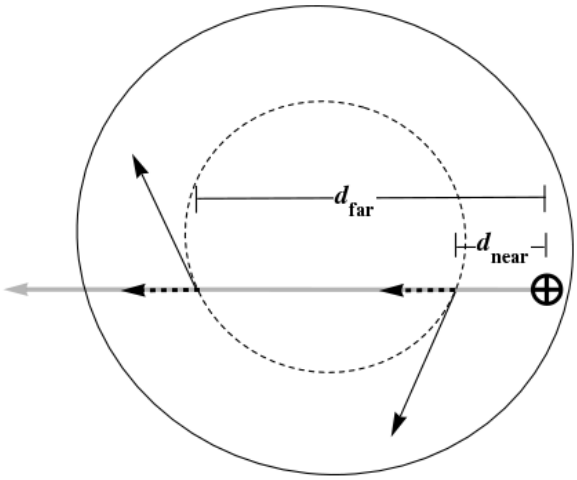

Fig. 16.— A schematic diagram indicating the near-far distance ambiguity, showing a top-down view of the MW disk. The $\oplus$ symbol indicates the location of Earth in the MW disk.

where $d_{\mathrm{MW\ GMC}}$ is the distance to each MW GMC and d_{M31} is the distance to M31. Using equation 32 with the $\int \mathrm{NH_3}(1,1)\mathrm{dv}$ data and corresponding distance data from Longmore et al. (2013), we found that

$$\begin{aligned} \log_{10}\left(I_{\mathrm{MW,\ d_{near}}}\left[\mathrm{K\ km\ s^{-1}}\right]\right) &= -1.7 \pm 0.1, \text{ and} \\ \log_{10}\left(I_{\mathrm{MW,\ d_{far}}}\left[\mathrm{K\ km\ s^{-1}}\right]\right) &= -0.7 \pm 0.1, \end{aligned} \tag{33}$$

where $I_{\mathrm{MW,\ d_{near}}}$ is $\int_{\mathrm{MW}\rightarrow\mathrm{M31}} \mathrm{NH_3}(1,1)\mathrm{dv}$ using $d_{\mathrm{MW\ GMC}} = d_{\mathrm{near}}$ and $I_{\mathrm{MW,\ d_{far}}}$ is $\int_{\mathrm{MW}\rightarrow\mathrm{M31}} \mathrm{NH_3}(1,1)\mathrm{dv}$ using $d_{\mathrm{MW\ GMC}} = d_{\mathrm{far}}$.

Another additional correction is required to compare the M31 $\int \mathrm{NH_3}(1,1)\mathrm{dv}$ results in equations 30 and 31 to the MW $\int \mathrm{NH_3}(1,1)\mathrm{dv}$ results in equation 33: one 33" beam in M31 is not the same as a 2° horizontal bin along the Galactic plane because we observe M31 as a tilted disk and the MW as an edge on disk. Thus, there are inherently less GMCs along a M31 sightline vs. a MW sightline (i.e., resulting from the effect of looking through a tilted disk vs. an edge on disk). The ratio of the two different path lengths through the respective M31 and MW disks along each sightline, $\frac{S_{\mathrm{MW}}}{S_{\mathrm{M31}}}$ (see Figure 17), would be one way to calculate this correction, but this is a huge overestimate because it assumes that ammonia in GMCs is present uniformly throughout each disk along a given sightline. However, as shown in Figure 1, GMCs are uniformly distributed in denser regions within the disk, and thus tilting the M31 disk to an edge on geometry would increase the ammonia emission by a factor much less than $\frac{S_{\mathrm{MW}}}{S_{\mathrm{M31}}}$. More realistically, a 2° bin from the Longmore et al. (2013) $\mathrm{NH_3}$ data

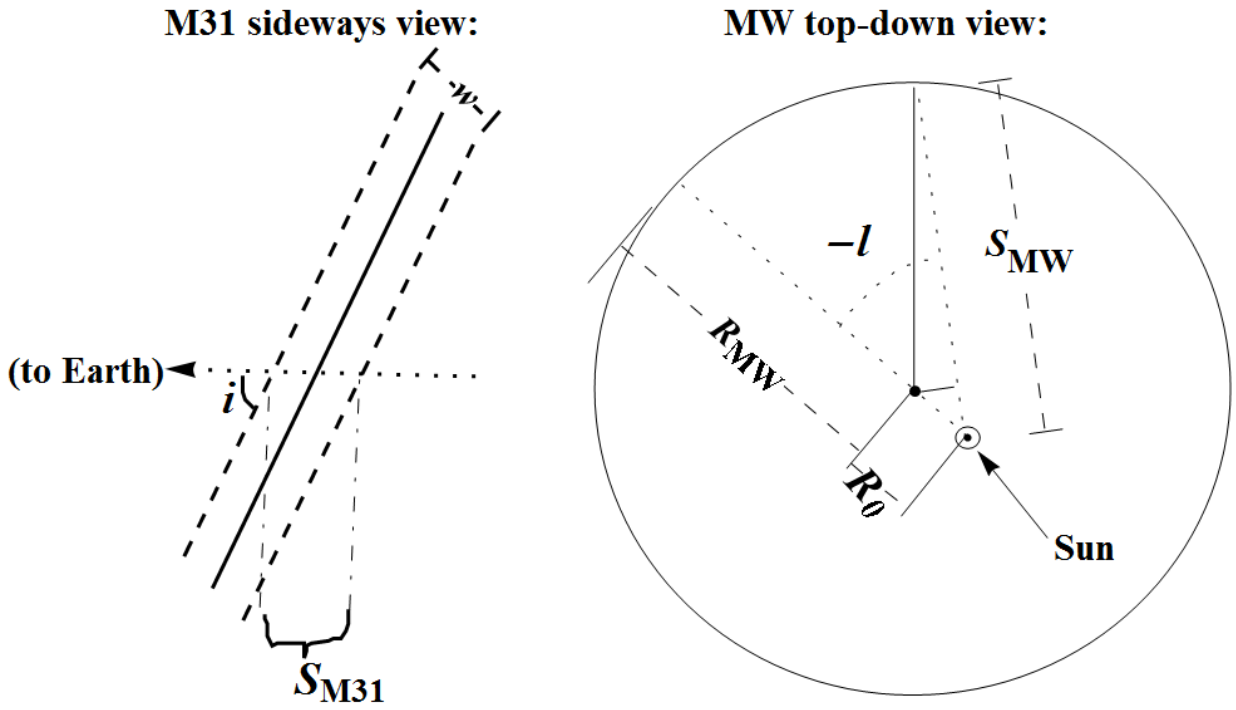

Fig. 17.— A diagram showing the difference in path length along a M31 sightline vs. a MW sightline.

represents a sum over the vertical height of the MW disk in ∼125 pc wide bins. Thus, we similarly define the typical $\int \mathrm{NH_3}(1,1)\mathrm{dv}$ in a M31 vertical bin (now 33" wide instead of 2° wide, but still 125 pc wide) by determining the number of GMCs in each vertical M31 bin (i.e., spanning the vertical height of the M31 disk; see Figure 18). The 506 observed sources shown in Figure 1 cover the most likely sources of ammonia emission within the M31 molecular ring, and so we simply count the typical number of observed sources within a 33" M31 vertical bin to obtain a correction factor due to the difference in disk geometry between M31 and the MW, as shown in Figure 18.

Using this method, we found a correction factor of

$$\frac{\int_{\mathrm{MW}} \mathrm{NH_3}(1,1)}{\int_{\mathrm{M31}} \mathrm{NH_3}(1,1)} = 2.50 \pm 0.05, \tag{34}$$

which lists the typical number of GMCs in a M31 vertical bin. Applying equation 34 to

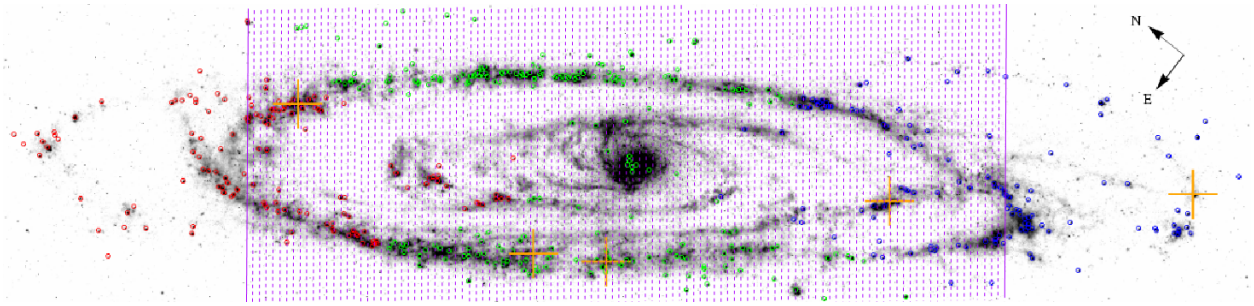

Fig. 18.— A schematic diagram showing the vertical binning process used in M31 to determine a correction factor due to the difference in disk geometry between M31 and the MW. We restrict the binning procedure to deprojected radii within the ∼11 kpc radius of the M31 molecular ring because of a source selection bias at larger radii.

equations 30 and 31 gives

$$\log_{10}\left(\int_{\text{mean bin}} \mathrm{NH_3}(1,1)\mathrm{dv}\left[\mathrm{K\ km\ s^{-1}}\right]\right) \leq -1.3, \text{ and}$$
$$\log_{10}\left(\int_{\text{median bin}} \mathrm{NH_3}(1,1)\mathrm{dv}\left[\mathrm{K\ km\ s^{-1}}\right]\right) \leq -1.2 \quad (35)$$

Finally, comparing equations 33 and 35 indicates that the near distance flux scaling method for $\int \mathrm{NH_3}(1,1)\mathrm{dv}$ in the MW is $\sim 4\sigma$ below the typical M31 $\int \mathrm{NH_3}(1,1)\mathrm{dv}$ value but the far distance MW flux scaling method for $\int \mathrm{NH_3}(1,1)\mathrm{dv}$ in the MW is $\sim 6\sigma$ above the typical M31 $\int \mathrm{NH_3}(1,1)\mathrm{dv}$ value. However, because the near and far distance ambiguity for the observed MW objects has not been solved, we can only conclude that a typical M31 GMC may have an $\mathrm{NH_3}$ content that is less than or equal to 4σ above the typical MW $\mathrm{NH_3}$ content.

5.2. $\mathrm{NH_3}$ Abundance Comparison

To resolve the ambiguity discussed in §5.1, we describe the $\mathrm{NH_3}$ abundance in a GMC, either in the MW or M31, by comparing the $\int \mathrm{NH_3}(1,1)\mathrm{dv}$ to the corresponding 500 μm integrated flux over the same region[39]: $\mathrm{NH_3}$ abundance $= \frac{\int \mathrm{NH_3}(1,1)\mathrm{dv}}{500\ \mu\mathrm{m\ flux}}$. Infrared emission from a GMC is a tracer of total gas as opposed to only dense gas (Carrol & Ostlie 2006,

[39]This ratio of fluxes is independent of distance, which allows for a comparison between the M31 and MW $\mathrm{NH_3}$ abundance without using the near/far distance ambiguity.

chap. 12), and so $\frac{\int \mathrm{NH_3(1,1)dv}}{500\ \mu\mathrm{m\ flux}}$ gives an indication of the amount of NH_3 per unit of total gas, or NH_3 abundance.

Thus, we obtained 500 μm maps of M31 (Smith et al. 2012) and the MW (Molinari et al. 2010) and carried out the same vertical binning procedure for each map to account for the different disk geometry between the MW and M31 (as done in §5.1 for $\int \mathrm{NH_3}(1,1)\mathrm{dv}$). This process is shown for the MW and M31 in Figures 19 and 20, respectively.

Fig. 19.— A schematic diagram of the vertical binning procedure used on a MW 500 μm map (Molinari et al. 2010) from $l = 30°$ to $l = -54°$ in order to account for the different disk geometry between the MW and M31 (l represents Galactic Longitude; see Carrol & Ostlie 2006, chap. 12). We skip the Galactic Center at $|l| \leq 4°$ in this binning procedure because the associated physical conditions are much different from the rest of the MW (Longmore et al. 2013) and M31 (J. Bally, private communication).

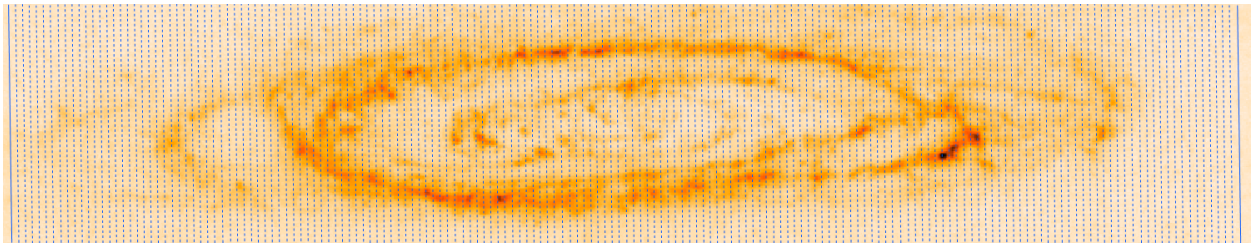

Fig. 20.— A schematic diagram of the vertical binning procedure used on a M31 500 μm map (Smith et al. 2012) to account for the different disk geometry between the MW and M31. Unlike the source selection bias described in Figure 18, no selection bias is present in the coverage for the M31 500 μm map, and thus our vertical binning procedure here spans to the apparent edge of the M31 disk.

As shown in Figure 20 , we determine the average M31 500 μm flux for each 33" bin, $I_{33\text{" M31 bin, 500 }\mu\mathrm{m}}$, to be

$$I_{33\text{" M31 bin, 500 }\mu\mathrm{m}} = (44 \pm 1)\ \mathrm{Jy} \tag{36}$$

In M31, we can only place an upper limit on the typical NH_3 abundance in a GMC due to the non-detection of $NH_3(1,1)$ in individual spectra and stacked spectra. Thus, combining equations 35 and 36 gives an upper limit on the M31 NH_3 abundance from the mean stack,

$\left(\frac{\int \mathrm{NH_3(1,1)dv}}{500\ \mu\mathrm{m\ flux}}\right)_{\mathrm{M31,\ mean}}$, in a typical GMC:

$$\log_{10}\left(\left(\frac{\int \mathrm{NH_3}(1,1)\mathrm{dv}}{500\ \mu\mathrm{m\ flux}}\right)_{\mathrm{M31,\ mean}}\left[\frac{\mathrm{K\ km\ s^{-1}}}{\mathrm{Jy}}\right]\right) \leq -1.89 \pm 0.01, \tag{37}$$

and an upper limit on the M31 NH_3 abundance from the median stack, $\left(\frac{\int \mathrm{NH_3(1,1)dv}}{500\ \mu\mathrm{m\ flux}}\right)_{\mathrm{M31,\ median}}$, in a typical GMC:

$$\log_{10}\left(\left(\frac{\int \mathrm{NH_3}(1,1)\mathrm{dv}}{500\ \mu\mathrm{m\ flux}}\right)_{\mathrm{M31,\ median}}\left[\frac{\mathrm{K\ km\ s^{-1}}}{\mathrm{Jy}}\right]\right) \leq -1.79 \pm 0.01, \tag{38}$$

In contrast, we can use the MW NH_3 data from Longmore et al. (2013) and corresponding binned 500 μm data from Molinari et al. (2010) to obtain specific ammonia abundances for each 2° bin in addition to the average abundance, $\left(\frac{\int \mathrm{NH_3(1,1)dv}}{500\ \mu\mathrm{m\ flux}}\right)_{\mathrm{MW}}$. Averaging the separate 2° bins, we find that

$$\log_{10}\left(\left(\frac{\int \mathrm{NH_3}(1,1)\mathrm{dv}}{500\ \mu\mathrm{m\ flux}}\right)_{\mathrm{MW}}\left[\frac{\mathrm{K\ km\ s^{-1}}}{\mathrm{Jy}}\right]\right) = -1.84^{+0.05}_{-0.06} \tag{39}$$

Comparing equations 37, 38, and 39 indicates that our upper limit on the M31 NH_3 abundance is consistent with the typical MW NH_3 abundance. Equations 37, 38, and 39, and the $\left(\frac{\int \mathrm{NH_3(1,1)dv}}{500\ \mu\mathrm{m\ flux}}\right)_{\mathrm{MW}}$ data points corresponding to equation 39 are shown below in Figure 21.

It is also worth noting how our upper limit on the M31 NH_3 abundance would change if we assumed a different typical $NH_3(1,1)$ line width[40] in order to calculate an upper limit on M31 $\int \mathrm{NH_3}(1,1)\mathrm{dv}$. Table 3 shows the results of calculating an upper limit on the NH_3 abundance using a range of line widths, indicating that smaller line widths create a more stringent upper limit on the M31 NH_3 abundance in comparison with the MW NH_3 abundance, and thus ultimately followup observations with longer integration times are needed to detect NH_3 and confirm our upper limit.

[40] $NH_3(1,1)$ has never been detected in M31, and so we can only estimate the width of an "observed line."

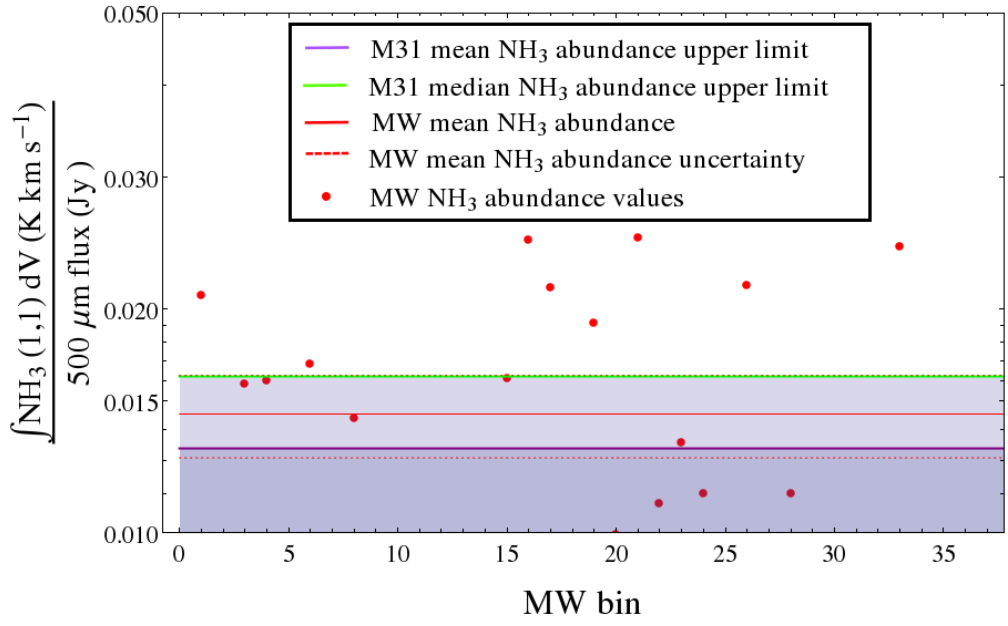

Fig. 21.— A plot comparing the NH_3 abundance, $\frac{\int NH_3(1,1)dv}{500\ \mu m\ flux}$, between the MW and M31. The x-axis represents the specific 2° binning channels, ranging from $l = 30°$ to $l = -54°$, used to calculate $\left(\frac{\int NH_3(1,1)dv}{500\ \mu m\ flux}\right)_{MW}$.

Table 3

Gaussian line width (FWHM) (km s^{-1})	10	20	30	40	50
$\log_{10}\left(\left(\frac{\int NH_3(1,1)dv}{500\ \mu m\ flux}\right)_{M31,\ mean}\right)$ $\left(\log_{10}\left(\left[\frac{K\ km\ s^{-1}}{Jy}\right]\right)\right)$	$\leq -2.28 \pm 0.01$	$\leq -1.98 \pm 0.01$	$\leq -1.81 \pm 0.01$	$\leq -1.68 \pm 0.01$	$\leq -1.59 \pm 0.01$
$\log_{10}\left(\left(\frac{\int NH_3(1,1)dv}{500\ \mu m\ flux}\right)_{M31,\ median}\right)$ $\left(\log_{10}\left(\left[\frac{K\ km\ s^{-1}}{Jy}\right]\right)\right)$	$\leq -2.19 \pm 0.01$	$\leq -1.89 \pm 0.01$	$\leq -1.71 \pm 0.01$	$\leq -1.59 \pm 0.01$	$\leq -1.49 \pm 0.01$
$\log_{10}\left(\left(\frac{\int NH_3(1,1)dv}{500\ \mu m\ flux}\right)_{MW}\right)$ $\left(\log_{10}\left(\left[\frac{K\ km\ s^{-1}}{Jy}\right]\right)\right)$	$-1.84^{+0.05}_{-0.06}$	$-1.84^{+0.05}_{-0.06}$	$-1.84^{+0.05}_{-0.06}$	$-1.84^{+0.05}_{-0.06}$	$-1.84^{+0.05}_{-0.06}$

6. H_2O Analysis

We used the same flux scaling and MW comparison procedure with H_2O as we did with $NH_3(1,1)$. The non-detection of H_2O in the stacking procedure allows for a 3σ upper limit calculation of the peak M31 H_2O maser flux density in a typical GMC, $S_{peak,\ M31}$, which gives

$$\log_{10}\left(S_{peak,\ M31}\ [Jy]\right) \leq -3.9 \tag{40}$$

using the rms noise from the either the average or median H_2O stack[41].

We also used a set of MW H_2O maser peak flux density values (Urquhart et al. 2011) and corresponding distances (Urquhart et al. 2009a, Urquhart et al. 2009b), applying the same flux scaling methodology as equation 32, to calculate the MW peak flux density in a typical molecular cloud[42], placed at the distance of M31 $S_{\text{peak, MW}}$. However, because our upper limit calculation of $S_{\text{peak, M31}}$ incorporates a full sample of observed sources, we also represent the full sample of observed MW H_2O maser sources from Urquhart et al. (2011) by additionally incorporating the non-detections within the sample of observed sources (Urquhart et al. 2011 list a 50% detection rate among observed sources). To incorporate these non-detections, we used the rms noise data for each MW H_2O maser detection (Urquhart et al. 2011) to represent an additional non-detection. Incorporating this 50% detection rate, we found that

$$\log_{10}(S_{\text{peak, MW}}\ [\text{Jy}]) = -4.5 \pm 0.2 \tag{41}$$

Noting that comparing the flux of two objects at the same distance (i.e., the distance to M31) is identical to comparing their luminosities, equation 40 and equation 41 indicate that our upper limit on the M31 H_2O maser luminosity in a typical GMC is consistent with the MW H_2O maser luminosity in a typical GMC.

7. Conclusion & Future Work

We observed 506 luminous 24 μm regions in M31 for NH_3(1,1), NH_3(2,2), H66α, and H_2O in order to describe the physical conditions in M31 GMCs and corresponding star-forming regions. In the first observed 200 sources, Darling (2011) presents and explains the detection of five H_2O masers, which is expected to allow for the most precise measurement yet of $\vec{v}_{\text{M31-tan}}$ (see Appendix 1). No additional masers were detected in the second observed batch of 306 sources (J. Darling, private communication).

Although many potential features appeared in individual NH_3(1,1), NH_3(2,2), and H66α spectra throughout the data reduction process, detection heuristics ultimately served to

---

[41]To two significant figures, $\log_{10}(3 \times 0.00012) = \log_{10}(3 \times 0.00013)$ (i.e., the rms noise from the H_2O mean and median stack are too similar to one another to create a noticeably different 3σ upper limit, and so we use one upper limit representing both stacks).

[42]Unlike our NH_3(1,1) comparison, here we do not need to incorporate a difference in angular size in order to compare identical physical sizes or disk geometry between the MW and M31 because H_2O maser emission within a GMC is dominated from extremely compact sources on the edge of a single HII region, well embedded within the much larger GMC, and therefore a 33" beam in both M31 and the MW will cover the same extent of H_2O maser emission (J. Darling, private communication)

indicate that none of these features were real, and so we present no detection in any of the individual 506 spectra for NH_3(1,1), NH_3(2,2), and H66α. The typical rms noise in individual 244 kHz channel spectra was 2.5 mJy.

In an additional stacking procedure, where we shifted and separately averaged and medianed 446 NH_3(1,1), NH_3(2,2), and H66α spectra and 441 H_2O spectra, we do not detect any of the observed lines. The typical rms noise in 244 kHz channel stacked spectra was 0.13 mJy, which agrees with $\sqrt{N}$ noise reduction.

The non-detection of NH_3(1,1) in the stacking procedure allows for an upper limit calculation of $\int NH_3(1,1)dv$ in a typical M31 GMC. $\int NH_3(1,1)dv$ is an indicator of the amount of NH_3, and more generally the amount of dense gas and star formation, in a typical GMC. By comparing $\int NH_3(1,1)dv$ values between M31 and the MW (scaled to the distance of M31), we found that our upper limit for M31 $\int NH_3(1,1)dv$ in a typical GMC varies in consistency with the MW $\int NH_3(1,1)dv$ in a typical GMC depending on the use of the near or far distance in our MW flux scaling procedure. However, by additionally comparing the ratio of $\int NH_3(1,1)dv$ to 500 μm flux between M31 and the MW, we conclude that our upper limit on the M31 NH_3 abundance is consistent with the MW NH_3 abundance in a typical GMC.

The non-detection of H_2O in the stacking procedure allows for an estimate of an upper limit on the typical H_2O maser flux density in an M31 GMC. In comparison to MW H_2O maser flux density data (scaled to the distance of M31), we found that our upper limit on the M31 H_2O maser luminosity is consistent with the MW H_2O maser luminosity in a typical GMC.

Ultimately, only a detection of NH_3(1,1) and/or H_2O will determine if these upper limits are correct. Thus, follow-up observations with longer integration times that detect NH_3(1,1) and/or H_2O are needed to more accurately describe the physical conditions in M31 GMCs.

Appendix 1[43]: Uses and Measurements of $\vec{v}_{\mathbf{M31}}$

A. Introduction

The radial velocity of the M31, $v_{\text{M31-rad}}$, is well known (e.g., see Table 1 in Karachentsev & Kashibadze 2006). However, measurements and derivations of M31's transverse velocity, $\vec{v}_{\text{M31-tan}}$, and consequentially its three dimensional velocity vector, $\vec{v}_{\text{M31}}$, remain imprecise and potentially inaccurate. Many defining static and dynamic characteristics of M31 and the Local Group[44] (LG) rely heavily on an accurate and precise value of $\vec{v}_{\text{M31}}$. In particular, the current range of uncertainty on $\vec{v}_{\text{M31}}$ allows for a number of different possible outcomes in determining the MW, M31, and LG mass (Brunthaler et al. 2007; van der Marel & Guhathakurta 2008; Li & White 2008; Watkins et al. 2010; van der Marel et al. 2012a), dark matter halo structure[45] (Loeb et al. 2005; Cox & Loeb 2008; Li & White 2008), and past and future evolution (Sawa & Fujimoto 2005; Fouquet et al. 2012; van der Marel & Guhathakurta 2008; van der Marel et al. 2012b; Peebles & Tully 2013; Cox & Loeb 2008). As a result, a more accurate and precise measurement of $\vec{v}_{\text{M31-tan}}$, and thus of $\vec{v}_{\text{M31}}$, will allow for a more accurate physical model of the LG and its components.

In this appendix, we discuss the characteristic LG properties that rely on an accurate and precise measurement of $\vec{v}_{\text{M31}}$ (§B.1 and §B.2) and further explain how such accuracy and precision ultimately depends on directly measuring M31's proper motion[46] (PM) (§B.3). We present a comparative analysis of different methods used to measure M31's PM, both indirectly (§C.1 and §C.2) and directly (§C.3), and discuss the potential use of H_2O masers for an extremely accurate and precise M31 PM measurement (§D). The PM measurement of H_2O masers[47] in M31 are expected to provide the most accurate and precise value of $\vec{v}_{\text{M31-tan}}$ (Darling 2011), and, hence, act as the most useful observational tool to model the static and dynamic properties of the LG and its components (§E).

---

[43]This section was originally written for a writing course at CU Boulder (WRTG 3030, Writing on Science and Society) during the Spring 2013 semester.

[44]See footnote 1.

[45]A dark matter halo is thought to be composed of non-baryonic matter and surround every galaxy, being more than 10 times as massive and 100 times as large (i.e., linear distance) as the luminous (i.e., baryonic) matter in a galaxy (Carrol & Ostlie 2006, §24.2, pg. 884).

[46]See footnote 2

[47]See footnote 3

B. The Local Group

B.1. Local Group Statics

B.1.1. Mass

The first method used to estimate the LG mass is known as the Timing Argument (TA; Kahn & Woltjer, 1959) and is still commonly used today. The basic premise of the argument is governed by Kepler's laws and goes as follows: we can parameterize the M31 orbit about the MW, assuming that the two galaxies are gravitationally bound to one another, such that (Binney & Tremaine, 1987)

$$r_{\rm M31} = a_{\rm M31}(1 - e\cos(\eta)), \text{and} \tag{B1}$$

$$t = (\eta - e\sin(\eta))\sqrt{\frac{a_{\rm M31}^3}{G\ M_{\rm LG}}}, \tag{B2}$$

where $r_{\rm M31}$ is the current distance between the MW and M31, t represents the current age of the Universe and assumes that the MW-M31 system began at a single point at $t = 0$, $a_{\rm M31}$ is the M31 orbital semi-major axis about the MW, G is Newton's Gravitational constant, $M_{\rm LG}$ is the total mass of the LG, e is the M31 orbital eccentricity about the MW, and η represents the parameterization variable known as the eccentric anomaly[48]. Similarly, we can write (Kochanek, 1996)

$$v_{\text{M31-rad}} = \frac{e\sin(\eta)}{1 - e\cos(\eta)}\sqrt{\frac{a_{M31}^3}{G\ M_{LG}}}, \text{and} \tag{B3}$$

$$\vec{v}_{\text{M31-tan}} = \frac{\sqrt{1-e^2}}{1 - e\cos(\eta)}\sqrt{\frac{a_{M31}^3}{G\ M_{LG}}}, \tag{B4}$$

Using an independent estimate and/or measurement of $r_{\rm M31}$, t, $v_{\text{rad-M31}}$, and $\vec{v}_{\text{M31-tan}}$ in equations B1-B4 allows for an estimate of $M_{\rm LG}$, $a_{\rm M31}$, e, and η (where η is on the interval $[\pi, 2\pi]$, assuming that M31 and the MW are approaching each other for the first time), which, in turn, allows for an estimate of (van der Marel & Guhathakurta 2008)

$$r_{\rm peri} = \frac{a_{\rm M31}}{1 - e}, \text{and} \tag{B5}$$

$$T = 2\pi\sqrt{\frac{a_{\rm M31}^3}{G\ M_{\rm LG}}}, \tag{B6}$$

[48]Note that in this parameterization, $\eta = 0$ corresponds to the pericenter passage at $t = 0$, and $\eta = 2\pi$ corresponds to the pericenter passage at $t = T$, where T is M31 the orbital period about the MW.

where $r_{\rm peri}$ is M31's position at pericenter.

Brunthaler et al. (2007) make PM measurements with the Very Long Baseline Array[49] to estimate a lower limit for the M31 mass, $M_{\rm M31}$. They measure the PM (and resultantly the tangential velocity; see §B.3) of IC10, a satellite galaxy of M31, using previously detected H_2O masers. They also use previously obtained PM measurements for M33 (Brunthaler et al. 2005), another M31 satellite galaxy. Combining the IC10 and M33 PM measurements, they provide a lower limit on $M_{\rm M31}$. Their underlying assumption in calculating $M_{\rm M31}$ is that M33 and IC10 are both gravitationally bound to M31 (i.e., the total energy, $E_{\rm total}$, is negative), in which case they argue that the velocity of the two galaxies relative to M31 must be smaller than their escape velocities:

$$\frac{1}{2}(m)v_{\rm rel}^2 - G\frac{M_{\rm M31}(m)}{R} = E_{\rm total} < 0, \tag{B7}$$

and rearranging equation B7 to solve for $M_{\rm M31}$ gives

$$M_{\rm M31} > \frac{v_{\rm rel}^2(R)}{2\,G}, \tag{B8}$$

where m is the mass of either M33 or IC10, R is the orbital radius of either M33 or IC10 about M31, and $v_{\rm rel}$ is the relative orbital velocity of either M33 or IC10 with respect to M31, respectively. Because $v_{\rm rel}$ for M33 or IC10 can only be known given the full three dimensional velocities for both M31 and either M33 or IC10, Brunthaler et al. (2007) can only estimate a $M_{\rm M31}$ lower limit which incoorporates $v_{\rm M31\text{-}rad}$ but not $\vec{v}_{\rm M31\text{-}tan}$. Thus, they conclude that

$$M_{M31} > 7.5 \times 10^{11} {\rm M}_\odot, \tag{B9}$$

where $\rm M_\odot$ is the mass of the Sun. Brunthaler et al. (2007) do not list an uncertainty in equation B9 above (see Brunthaler et al. 2007, p. 105).

van der Marel & Guhathakurta (2008) use a number of statistical methods to determine $\vec{v}_{\rm M31\text{-}tan}$[50] and resultantly calculate the LG mass via the TA. Their derived value for $\vec{v}_{\rm M31\text{-}tan}$ is small compared to the known M31 radial velocity, suggesting that M31 and the MW are gravitationally bound. Thus, they use an orbital radius $a_{\rm M31} = (770 \pm 40)$ kpc (McConnachie et al. 2005) to determine a corresponding relative velocity given by $v_{\rm rel} = v_{\rm M31} = \sqrt{v_{\rm M31\text{-}rad}^2 + v_{\rm M31\text{-}tan}^2}$. van der Marel & Guhathakurta (2008) then use two separate methods to calculate (1) a lower limit and (2) a general estimate for the LG mass:

---

[49]The Very Long Baseline Array combines the signals from ten separate radio telescopes to provide μarcsecond order of magnitude accuracy and precision for PM measurements (see §B.3 and §D.1).

[50]See §C.3; their statistical approach to calculating the M31 transverse velocity also uses the M33 and IC10 PM results from Brunthaler et al. (2005) and Brunthaler et al. (2007), respectively.

1. They use equation (B8), the same argument as Brunthaler et al. (2007), and determine

$$M_{\rm LG} > 1.72^{+0.26}_{-0.25} \times 10^{12}{\rm M}_{\odot} \tag{B10}$$

2. Using recent data on the age of the Universe (i.e., $t = 13.73^{+0.16}_{-0.15}$ Gyr; see p. 193), they use the TA (see equations (B1)-(B6) above, and also the discussion in van der Marel & Guhathakurta 2008 on p. 193) to determine

$$M_{LG} = 5.58^{+0.85}_{-0.72} \times 10^{12}{\rm M}_{\odot}. \tag{B11}$$

It is important to note that the main sources of uncertainty for $M_{\rm LG}$ in equation (B11) come from the uncertainty in $a_{\rm M31} = (770 \pm 40)$ kpc, and $\vec{v}_{\rm M31\text{-}tan}$ (see §C.3 for a further discussion on van der Marel & Guhathakurta's (2008) calculation of $\vec{v}_{\rm M31\text{-}tan}$).

Watkins et al. (2010) present a mass estimate for M31 and the MW out to a radial distance of 300 kpc using two different methods:

1. using the line of sight velocities of M31 and MW satellite galaxies and assuming velocity isotropy[51]. The resulting mass estimates are

$$M_{\rm MW} = (0.9 \pm 0.3) \times 10^{12}{\rm M}_{\odot},$$

with velocity anisotropy creating an upper and lower bound of $3.4 \times 10^{12}{\rm M}_{\odot}$ and 0.7×10^{12} M$_{\odot}$, respectively, and

$$M_{\rm M31} = (1.4 \pm 0.4) \times 10^{12}{\rm M}_{\odot}, \tag{B12}$$

with velocity anisotropy creating an upper and lower bound of 1.6×10^{12} M$_{\odot}$ and 1.3×10^{12} M$_{\odot}$, respectively.

2. additionally incorporating the PM of the M31 and MW satellite galaxies into method 1. The resulting MW mass estimate is

$$M_{\rm MW} = (1.4 \pm 0.3) \times 10^{12}{\rm M}_{\odot}, \tag{B13}$$

with velocity anisotropy creating an upper and lower bound of 2.7×10^{12} M$_{\odot}$ and 1.2×10^{12} M$_{\odot}$, respectively. $M_{\rm M31}$ does not change in method 2 compared to method 1.

---

[51]Watkins et al. (2010) uses the term "velocity isotropy" to imply that the velocity dispersions for $v_{\rm M31\text{-}rad}$ and $\vec{v}_{\rm M31\text{-}tan}$ are equal to one another.

Watkins et al. (2010) explain that both the inapplicability of method 2 to improving the $M_{\rm M31}$ accuracy and the major source of their uncertainty in equations (B12) and (B13) are likely due to the lack of PM measurements available for M31 satellite galaxies[52]. Although they does not explicitly list a value for $M_{\rm LG}$, a rough estimate is possible assuming that $M_{\rm LG} = M_{\rm MW} + M_{\rm M31}$ (see van der Marel et al. 2012, p. 12). Hence, combining equations (B12) and (B13) gives

$$M_{\rm LG} = (2.5 \pm 0.5) \times 10^{12} {\rm M}_{\odot}. \tag{B14}$$

van der Marel et al. (2012a) draw on the work from Sohn et al. (2012)[53] to derive an observationally-based value for $\vec{v}_{\rm M31}$, and resultantly a TA-based virial mass[54] for the MW, M31 and LG. Similar to the methods in van der Marel & Guhathakurta (2008) and Li & White (2008), van der Marel et al. (2012a) incorporate the full value of $\vec{v}_{\rm M31}$ (i.e., including $\vec{v}_{\rm M31\text{-}tan}$) into the TA. They then continue and estimate the mass of M33 using information from previous studies about the M33 and M31 mass to light ratio, an assumed dark matter halo distribution, and their own estimate of $M_{\rm M31}$ from the TA. van der Marel et al. (2012a) conclude that M33 and M31 most likely form a bound pair. However, the assumption that M33 and M31 are bound slightly changes the range of possible initial conditions in the TA-based Monte Carlo scheme used to calculate $M_{\rm MW}$, $M_{\rm M31}$, and $M_{\rm LG}$. Hence, incorporating the bound nature of M33 to M31 into their TA analysis, van der Marel et al. (2012a) determine a final estimate of

$$M_{\rm MW} = 2.4^{+0.9}_{-1.0} \times 10^{12} {\rm M}_{\odot}, \tag{B15}$$

$$M_{\rm M31} = (1.54 \pm 0.39) \times 10^{12} {\rm M}_{\odot}, {\rm and} \tag{B16}$$

$$M_{\rm LG} = (3.17 \pm 0.56) \times 10^{12} {\rm M}_{\odot}. \tag{B17}$$

Li & White (2008) use the Millennium Simulation (Springel et al., 2005), a numerical simulation based on the Λ Cold Dark Matter (ΛCDM) cosmological model[55] which follows

---

[52]Method 2 incorporates the PM of six MW satellites but only two M31 satellites (M33 and IC10; see Brunthaler et al. 2005 and Brunthaler et al. 2007, respectively).

[53]Sohn et al. (2012) determine the M31 transverse velocity by measuring the PM of M31 stars (see §C.3).

[54]The virial mass is considered to be a reasonable measurement of the total mass within a dark matter halo based on ΛCDM theory (see footnote 55). It is defined as the mass contained within the virial radius, where such an estimate requires an assumption of the dark matter halo density profile (see in van der Marel et al. 2012a, equations A1 and A3).

[55]The Λ Cold Dark Matter cosmological model explains the structure and evolution of the Universe via the existence of (1) Λ, known as the "cosmological constant" and often used as an explanation for "dark

the motion of $\sim 10^{10}$ dark matter particles (see Li & White 2008, p. 1460) to derive the true masses of the MW and LG from their TA masses. The true mass is determined from a selection process within the Millennium Simulation of spiral pairs similar to the M31-MW system, whereas the free Keplerian parameters used to determine the TA mass (see equations (B1)-(B6)) are provided from the same selection process as "observable" quantities. Then, after calculating the TA mass and noting the ratio for the true mass to the TA mass in the simulation, they present estimates for the true mass of the MW and the LG:

$$M_{\rm MW} = 2.4^{+0.9}_{-1.0} \times 10^{12} {\rm M}_{\odot}, \text{and} \tag{B18}$$

$$M_{\rm LG} = (5.3 \pm 2.2) \times 10^{12} {\rm M}_{\odot}, \tag{B19}$$

and a rough estimate of $M_{\rm M31}$ can be made using equations (B18), (B19), and $M_{\rm M31} = M_{\rm LG} - M_{\rm MW}$ (see van der Marel et al. 2012a, p. 10), which gives

$$M_{\rm M31} = (2.9 \pm 2.4) \times 10^{12} {\rm M}_{\odot}. \tag{B20}$$

Figure 22 shows a comparison of the mass estimates from equations (B9)-(B20).

B.1.2. Dark Matter Halos

Li & White (2008) summarize their results with a discussion of the spread for $\vec{v}_{\rm M31\text{-}tan}$ resulting from their selection process in the Millennium Simulation (Springel et al., 2005). They find that $\vec{v}_{\rm M31\text{-}tan}$ is small compared to $v_{\rm M31\text{-}rad}$ and comparable to the van der Marel & Guhathakurta (2008) $\vec{v}_{\rm M31\text{-}tan}$ estimate for the real M31-MW system. Although Li & White (2008) do not actually measure a value for $\vec{v}_{\rm M31\text{-}tan}$ or use it as a free parameter, their resultant estimate for this value can be compared against a real measurement and ultimately be used to quantify the accuracy of the ΛCDM model in the Millennium Simulation (Springel et al., 2005) and its application to the nature of dark matter halos in the LG.

Loeb et al. (2005) present a model of the MW-M31-M33 system based on observational M33 data which predicts a range of values for $\vec{v}_{\rm M31\text{-}tan}$ (see §C.1 for a further discussion). Their simulation relies on a specific distribution of dark matter halos based on ΛCDM theory (see §2 in Loeb et al., 2005), as these components are much more massive than their visual

---

energy" and the accelerating expansion of the universe, and (2) Cold Dark Matter (CDM), considered to be non-baryonic particles that interact very weakly with electromagnetic radiation and explain the role of dark matter in galaxy structure, evolution, etc. (Carrol & Ostlie 2006, §30.1, pg. 1233) The ΛCDM cosmological model explains that the Universe is composed mostly of a combination of Λ (∼70%) and CDM (∼ 30%).

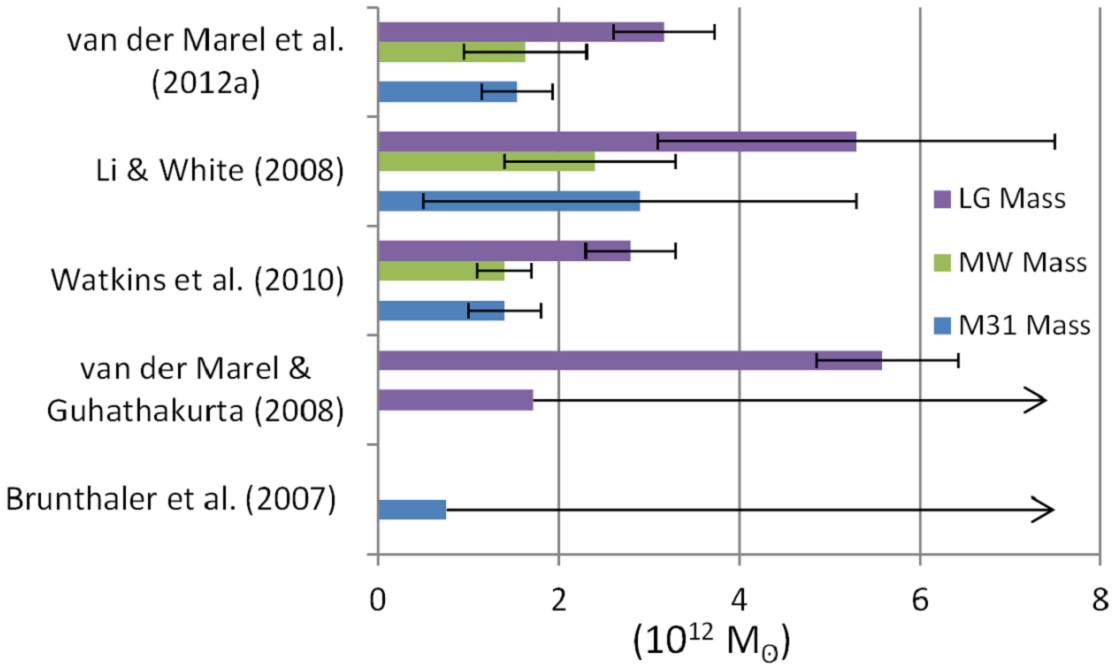

Fig. 22.— Mass estimates for the MW, M31, and the LG. Note that the estimates from Brunthaler et al. (2007) and van der Marel & Guhathakurta (2008) are lower limits on the M31 and LG mass, respectively.

counterparts and therefore extremely influential on LG dynamic behavior. Thus, an actual measurement of $\vec{v}_{\text{M31-tan}}$ can be compared with the predictions from Loeb et al. (2005) and will resultantly help to describe the density profiles and distribution of dark matter halos for M33, M31, and the MW.

Cox & Loeb (2008) simulate a N-body hydrodynamic collision of the anticipated future merger between M31 and the MW, where $\vec{v}_{\text{M31-tan}}$ is set as a free parameter (see §B.2.2). Similar to Li & White (2008) and Loeb et al. (2005), Cox & Loeb (2008) use a ΛCDM-based model to construct the various LG dark matter profiles. However, they additionally consider the effect of dynamical friction within the dark matter halos during the merger, and resultantly make assumptions about the nature of this frictional process (e.g., the shape of the potential well, the deceleration leading dependence on mass, density, etc.). Cox & Loeb (2008) gauge the success of their model by its ability to reproduce the well known values of the MW-M31 orbital radius and $v_{\text{M31-rad}}$, and to produce $\vec{v}_{\text{M31-tan}} < 200$ km s^{-1}, a consistent claim from previous models (e.g., Peebles et al., 2001; Loeb et al., 2005; van der Marel & Guhathakurta, 2008). Hence, comparing a real measurement of $\vec{v}_{\text{M31}}$ with the range of calculated $\vec{v}_{\text{M31}}$ values in this simulation will help to further describe the static

and dynamical nature of the LG dark matter halos.

B.2. Local Group Dynamics

Although the LG is often considered a quiescent environment, it provides us with the closest example to observe and model galactic dynamics. Due to our current limitations in astrometric[56] instrument precision, we are unable to measure the transverse velocity of galaxies beyond the Local group over a sufficient baseline. Consequentially, only a LG dynamical model of past and future evolution can be compared with current velocity observations, resultantly improving our understanding of galactic dynamics.

B.2.1. Past Evolution

Sawa & Fujimoto (2005) and Fouquet et al. (2012) both present similar dynamical models for the orbit of M31 and the origin of the LG which result in an estimate of $\vec{v}_{\text{M31-tan}}$. They both propose the occurrence of an ancient off-center collision between M31 and the MW, compressing the primordial interstellar gas to form many of the LG dwarf galaxies.

Sawa & Fujimoto (2005) focus their model, which examines various MW and M31 tidal streams[57], on recreating the structure and formation of the Large and Small Magellanic Clouds (LMC and SMC, respectively)[58] and the Magellanic Stream (MS)[59]. They also account for the present day observation of the LMC and SMC's large orbital angular momenta (and corresponding MS) around the MW (see, e.g., Fich & Tremaine). Their model of an ancient MW-M31 merger constrains $\vec{v}_{\text{M31-tan}}$ to allow for a small separation between the MW and M31 at an earlier epoch (see §C.1). In principle, any real measurement of $\vec{v}_{\text{M31-tan}}$ can be compared with the model's $\vec{v}_{\text{M31-tan}}$ predictions that describe the origin of the LMC-SMC system. Thus, comparing a real measurement of $\vec{v}_{\text{M31-tan}}$ with the $\vec{v}_{\text{M31-tan}}$ predictions from

[56]Astrometry refers to the subfield of astronomy which involves accurate and precise position measurements of stars, masers, planets, etc.

[57]A tidal stream refers to the streams of stars and gas that result from interacting galactic tidal forces.

[58]The LMC and SMC are both MW satellite dwarf galaxies.

[59]The Magellanic Stream is a high velocity gas cloud connecting the LMC and SMC. Although previous studies have successfully modeled the geometric and dynamical structures of the MS assuming its nature as a tidal stream, Sawa & Fujimoto (2005) argue that the MS is also a result of the proposed primordial M31-MW off-center collision.

Sawa & Fujimoto (2005) will ultimately determine the accuracy of their dynamical model.

Fouquet et al. (2012) focus their model on recreating the structure and formation of the Galactic Stream (GS)[60] and the LMC-SMC system. They use hydrodynamical simulations to examine the dynamics of the most prominent tidal stream formed during the proposed ancient M31-MW merger. They then compare this simulation with a backwards time evolution model of the LG, run until the LMC reaches the M31 outskirts, where $\vec{v}_{\text{M31-tan}}$ is set as a free parameter (see the bottom of p. 1773). However, within a specific range for $\vec{v}_{\text{M31-tan}}$, a striking set of coincidences appears upon comparison between the two models, specifically between the tidal stream in the ancient merger model and the LMC-SMC system in the backwards time evolution model. Resultantly, Fouquet et al. (2012) conclude that the present day LMC-SMC system and GS are both products of an ancient M31-MW merger. Hence, a real measurement of $\vec{v}_{\text{M31-tan}}$ will act as a heuristic to confirm the accuracy of their model in describing the origin of the GS and LMC-SMC system.

B.2.2. Future Evolution

Cox & Loeb (2008) simulate a N-body hydrodynamic collision of the anticipated future merger between M31 and the MW, incorporating the effect of dynamical friction between the two galaxy's dark halos (see §B.1). The simulation, which begins at $t = -5$ Gyr from the current epoch, relies on an assumption of three of initial conditions: orbital separation, eccentricity, and angular velocity (see p. 464). Cox & Loeb (2008) determine the range for these three initial conditions based on their agreement with the known observations at $t = 0$ Gyr for

1. r_{M31}, the separation of M31 and the MW,
2. $v_{\text{M31-rad}}$, and
3. $\vec{v}_{\text{M31-tan}}$.

They explain that r_{M31} and $v_{\text{M31-rad}}$ are well known and estimated to an uncertainty of $\sim$5%, but that measurements for $\vec{v}_{\text{M31-tan}}$ remain uncertain. Thus, constraints on their simulation are based mostly on agreement with r_{M31} and $v_{\text{M31-rad}}$, whereas $\vec{v}_{\text{M31-tan}}$ acts as a free parameter specified within a broad range. Incorporating the possible ranges for r_{M31},

[60]The Galactic Stream is a (proposed) tidal stream at the M31 outskirts.

$v_{\rm M31\text{-}rad}$, and $\vec{v}_{\rm M31\text{-}tan}$ into their model, they estimate that the first close pass between M31 and the MW will occur in less than 2 Gyr, and the two galaxies will fully merge in

$$t_{\rm merge} < 5{\rm Gyr} \tag{B21}$$

Throughout their simulation, Cox & Loeb (2008) track the Sun-like particles, which lie at comparable distances to the Sun's current distance from Galactic center (i.e., the MW center of mass), and resultantly predict (with 54 % confidence) that after the merger the Solar System will reside in the outer halo, greater than 30kpc away from the Galactic center. The merger also predicts values for $\vec{v}_{\rm M31}$ and $\vec{v}_{\rm M31\text{-}tan}$ at $t = 0$ Gyr. Thus, comparing measured values of $\vec{v}_{\rm M31}$ and $\vec{v}_{\rm M31\text{-}tan}$ with the model's predicted values will help to describe the accuracy of this dynamical model.

van der Marel & Guhathakurta (2008), using recent data on the age of the Universe (i.e., $t = 13.73^{+0.16}_{-0.16}$ Gyr; see p. 193), use the TA (see equations (B1)-(B6) in §B.1), incorporating their estimated value of $\vec{v}_{\rm M31\text{-}tan}$ (see §C.3), to determine

$$r_{\rm peri} = 23 \text{ kpc},$$

with a 1 σ confidence interval that $r_{\rm peri} \leq 40.9$ kpc, and

$$T = 16.70^{+0.27}_{-0.72} \text{ Gyr},$$

where $r_{\rm peri}$ is the M31-MW orbital pericenter distance and T is the M31-MW orbital period. Thus, assuming that the current orbital motion between the MW and M31 began from a pericenter at the beginning of the Universe, they calculate an approximate timescale for the M31-MW collision as

$$\begin{aligned} t_{\rm merge} &= T - t \\ &= 16.70^{+0.27}_{-0.26}{\rm Gyr} - 13.73^{+0.16}_{-0.16}{\rm Gyr} \\ t_{\rm merge} &\approx (3.0 \pm 0.3){\rm Gyr} \end{aligned} \tag{B22}$$

van der Marel et al. (2012b) present an analysis on the future of the MW-M31-M33 system. $\vec{v}_{\rm M31\text{-}tan}$ is not set as a free parameter, and is instead constrained based on it's derived observational value from Sohn et al. (2012; see §C.3) and van der Marel et al. (2012a; see §B.1 and §C.3). van der Marel et al. (2012b) take two different approaches to modeling the anticipated future MW-M31-M33 merger:

1. They use an N-body simulation similar to Cox & Loeb (2008), although they do not consider the effect of dynamical friction from dark matter halos. However, a more

accurate and precise estimate of $\vec{v}_{\text{M31-tan}}$ yields a more accurate precise estimate of collision timescales; they estimate the first close MW-M31 pass at $t = 3.87^{+0.42}_{-0.32}$ Gyr and the complete merger at

$$t_{\text{merge}} = 5.68^{+1.61}_{-0.72}\text{Gyr} \tag{B23}$$

Also similar to similar to Cox & Loeb (2008), van der Marel et al. (2012b) track Sun-like particles throughout their simulation, and they resultantly estimate (with 85 % confidence) that the Sun will end up at a greater radius from the new Galactic center compared to its current radius. They also note that no candidate Suns (0%) become entirely unbound from the MW-M31 merger remnant.

2. Additionally, van der Marel et al. (2012b) use Monte Carlo simulations and a simplified Keplerian model[61] in order to test the full range of uncertainties for the observations and results from Sohn et al. (2012) and van der Marel et al., (2012a). They determine a more realistic uncertainty for the first-pericenter in each component of the MW-M31-M33 system, and also for probabilistic likelihoods of the fate of M33 before, during, and after the MW-M31 merger (although compared to equation (B23), their new result for t_{merge} remains relatively unchanged). They explain that the most likely possible orbit for M33 (with 84% confidence) shows it missing the initial MW-M31 merger, then entering a decaying orbit around the merger remnant, and ultimately undergoing a later merger. However, a 9% chance shows M33 taking a direct hit with the MW before the MW-M31 merger, and a 7% chance shows M33 being ejected from the LG.

Figure 23 shows a comparison of the collision timescales for the MW-M31 merger, t_{merge}, from equations (B21)-(B23).

B.3. Proper Motion

Brunthaler et al. (2007), van der Marel & Guhathakurta (2008), Watkins et al. (2010), van der Marel et al. (2012a), Loeb et al. (2005), Sawa & Fujimoto (2005), Fouquet et al. (2012), and van der Marel et al. (2012b) all use the PM measurements of M33 (Brunthaler et al., 2005), IC10 (Brunthaler et al., 2007), and/or M31 (Sohn et al., 2012) in their analysis of the LG and its components. Although Li & White (2008) and Cox & Loeb (2008) do not directly use any PM measurements, their models ultimately predict values for the M31 PM.

[61]The basic idea behind their model is that instead of using a gravitational potential for each stellar particle, a galaxy is approximated by a single-component gravitational potential.

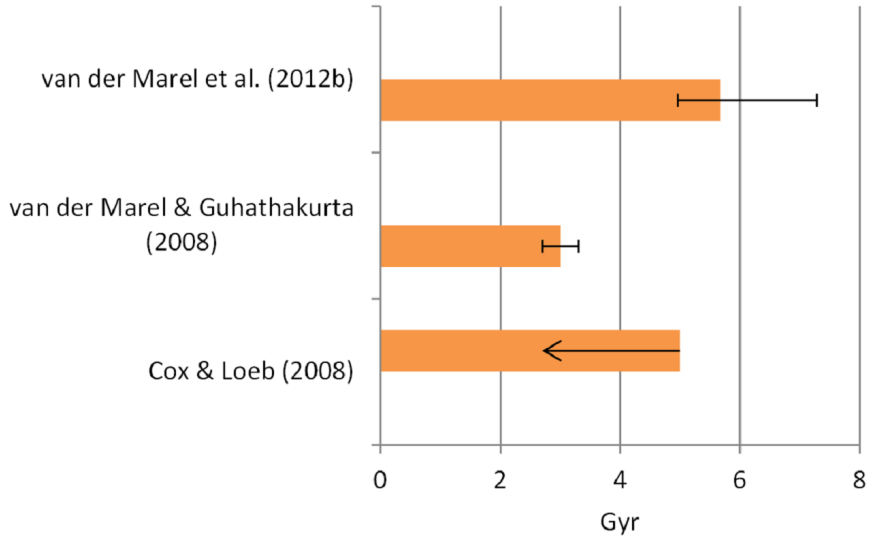

Fig. 23.— Collision timescales for the MW-M31 merger. Note that the estimate for $t_{\rm merge}$ from Cox & Loeb (2008) is an upper limit.

Thus, due to the common use of PM measurements in LG analysis, we present a further explanation of how these measurements are made (also see §C and §D).

After tracking an object's motion across the sky, we can subtract out the expected motion of the Earth rotating about its axis, the Earth revolving around the Sun, and, in extragalactic astronomy, the Sun revolving around the Galactic center. Thus, we can obtain the angular motion of a galaxy with respect to the MW center of mass by monitoring the angle it sweeps out on the sky, $\theta_{\rm total}$, in a given amount of time, Δt:

$$\omega_{\rm total} = \frac{\theta_{\rm total}}{\Delta t},$$

where $\omega_{\rm total}$ and $\theta_{\rm total}$ incorporate the angular motion of the galaxy's rotation, translation, and divergence[62−63]. If the distance to the galaxy, d, is known, then its tangential velocity, $v_{\rm tangential}$, is given by

$$\begin{aligned} v_{\rm tangential} &= d\,\frac{\theta_{\rm tangential}}{\Delta t} \\ &= d\,\omega_{\rm tangential}, \end{aligned} \tag{B24}$$

[62]A galaxy's divergence represents the concept that it appears to be either expanding or shrinking on the sky over time due to its approaching or receding nature from the MW, respectively.

[63]The motion from a galaxy's rotation, translation, and divergence are all orthogonal to one another, and can therefore be individually determined.

where $\theta_{\text{tangential}}$ and $\omega_{\text{tangential}}$ incorporate the angular motion of the galaxy's translation, but not its rotation or divergence. On the other hand, if d is unknown, but $v_{\text{rotational}}$ is known from the galaxy's rotation curve[64] (see e.g., Chemin et al. 2009), d is given by

$$d = \frac{v_{\text{rotational}}}{\omega_{\text{rotational}}},$$

where this reasoning is often referred to as the method of "rotational parallax".

Brunthaler et al. (2005) measure the M33 PM (i.e., ω_{total}), and Brunthaler et al. (2007) measure the IC10 PM, both using H_2O masers in each respective galaxy. They then use known rotation curves for each galaxy to determine their distances via rotational parallax, and resultantly use their distance estimates in equation (B24) to determine their tangential velocities. The approximate uncertainty in their PM measurements is on the order of

$$\begin{aligned} \sigma_{\text{water masers}} &\approx 8\ \mu\text{arcseconds in each epoch, and} \\ &\approx 5\ \mu\text{arcseconds yr}^{-1} \text{ over a 3-yr baseline fit} \end{aligned} \tag{B25}$$

See §D.1 for a further discussion of maser astrometry and precision.

C. Measuring M31 Proper Motion without Masers

C.1. Indirect Dynamical Models

Loeb et al. (2005) derive a range of realistic values for $\vec{v}_{\text{M31-tan}}$ based on a simulation of Local Group dynamics. Their main constraint on the values of $\vec{v}_{\text{M31-tan}}$ relies on the agreement of their simulation with current observational evidence showing that M33 has not been tidally disrupted by either M31 or the MW (i.e., M33 has no tidal streams). They create a simulation using a backwards time evolution model that relies on the current "initial conditions" of M31 and M33, including their three-dimensional space velocities (see p. 896). Since the three dimensional velocity vector of M33 is already known from H_2O maser PM measurements (Brunthaler et al., 2005), $\vec{v}_{\text{M31-tan}}$ is left as the only unknown variable, and therefore acts as a free parameter. Hence, the simulations that result in M33 not being tidally disrupted provide a corresponding estimate of $\vec{v}_{\text{M31-tan}}$. Loeb et al. (2005) resultantly determine that

$$\vec{v}_{\text{M31-tan}} = (100 \pm 20)\ \text{km s}^{-1}, \tag{C1}$$

[64]See footnote 23.

where motion along negative right ascension (α) and positive declination (δ)[65] is strongly ruled out. Although Loeb et al. (2005) use the precise M33 PM measurements from Brunthaler et al. (2005; see equation (B25) above) to constrain their estimate of $\vec{v}_{\rm M31\text{-}tan}$, their criteria for defining and selecting a non-tidally-stripped M33 inherently contains an additional nonzero uncertainty. Thus, Loeb et al. (2005) add an additional source of uncertainty in their estimate of $\vec{v}_{\rm M31\text{-}tan}$ that would otherwise not be present in a direct measurement of the M31 PM.

Sawa & Fujimoto (2005) initially set $\vec{v}_{\rm M31\text{-}tan}$ as a free parameter in their model of an ancient MW-M31 merger, which describes the origin of the LMC-SMC system. However, their MW-M31 model constrains $\vec{v}_{\rm M31\text{-}tan}$ such that

1. M31 was close to the MW at approximately 9 to 13 Gyr ago (i.e., a relatively small separation between M31 and the MW is necessary in order to account for an off-center collision which creates of many of the MW and M31 dwarf satellite galaxies),

2. the current MW-M31-LMC-SMC system roughly forms a plane as evidence that the LMC-SMC system originated from the MW-M31 system, and

3. as seen from the present location of the Sun, M31 orbits the MW counter clockwise as indicated by the current LMC-SMC system's orbital direction.

The above constraints applied to the MW-M31 ancient merger model gives

$$\vec{v}_{\rm M31\text{-}tan} = (230 \pm 60) \text{ km s}^{-1} \tag{C2}$$

Sawa & Fujimoto (2005) use assumptions 1-3 to estimate $\vec{v}_{\rm M31\text{-}tan}$ and its uncertainty, but they do not use any PM measurements in this estimation. Thus, as shown from a comparison of the uncertainty in equations (C1) and (C2), their estimated uncertainty of $\vec{v}_{\rm M31\text{-}tan}$ is larger than the uncertainty from a real measurement of $\vec{v}_{\rm M31\text{-}tan}$.

C.2. Statistical Models

Peebles et al. (2001) provide an estimate of the transverse velocity for a number of nearby galaxies (including M31). They preform a reduced χ^2 fit on the difference between known catalog values for the redshift and distance of approximately 40 nearby galaxies to the

[65]See footnote 24.

same values produced by the Action principle[66], and present the solutions which minimize χ^2. Peebles et al. (2001) explain that most of the solutions for $\vec{v}_{\text{M31-tan}}$ are on the order of ± 150 km s^{-1}, which sets an upper limit given by

$$\vec{v}_{\text{M31-tan}} < 150\text{km s}^{-1}, \tag{C3}$$

where no uncertainty is given for this specific estimate (see the bottom of p. 111 in Peebles et al., 2001).

Peebles & Tully (2013) present a similar argument to Peebles et al. (2001). They similarly minimize a reduced χ^2 fit between the Action principle and known catalog values for a number of LG galaxies (including M31) to resultantly predict their orbital motions and transverse velocities. The main difference in this statistical model from Peebles et al. (2001) is that Peebles & Tully (2013) use known catalog values that either

- were previously not available in the Peebles et al. (2001) paper (e.g., PM measurements) or
- have been more recently updated since the Peebles et al. (2001) paper (e.g., mass and distance measurements)

in order to constrain the free parameters in their model. Their updated cosmological model predicts the future orbital motion of M31, the LMC, M33, IC10, and a few other LG galaxies. Although Peebles & Tully (2013) do not list a quantitative value for $\vec{v}_{\text{M31-tan}}$, they present an interesting result for the M31 orbital motion. In contrast to Loeb et al. (2005), Sawa & Fujimoto (2005), Peebles et al. (2001), van der Marel & Guhathakurta (2008; see §C.3), and Sohn et al. (2012; see §C.3), Peebles & Tully (2013) find that $\vec{v}_{\text{M31-tan}}$ is considerably large compared to $v_{\text{M31-rad}}$ (see Figure 2 in Peebles & Tully, 2013). For this reason, we represent Peebles & Tully's (2013) estimate for $\vec{v}_{\text{M31-tan}}$ as a lower limit given by

$$\vec{v}_{\text{M31-tan}} > 290 \text{ km s}^{-1}, \tag{C4}$$

where we choose 290 km s^{-1} for the $\vec{v}_{\text{M31-tan}}$ lower limit based on the otherwise greatest $\vec{v}_{\text{M31-tan}}$ upper limit that remains within the uncertainty (see equation (C2)).

---

[66]Peebles et al. (2001) uses the Action Principle, a Lagrangian based approach to determining an object's motion and position, adapted to reflect ΛCDM theory (see §C.1 in Peebles et al., 2001). Using a ΛCDM-based mass to light ratio for each galaxy, the Action Principle is based mainly on the assumption that the luminosities of galaxies trace their mass (and thus a measurement of M31 PM will ultimately determine if this assumption is valid).

C.3. Indirect and Direct Observational Models

van der Marel & Guhathakurta (2008) use three different independent statistical methods to determine $\vec{v}_{\text{M31-tan}}$:

1. They use the measured line of sight velocity from 17 different M31 satellite galaxies, assuming that v_{rad} for each satellite follows $v_{\text{M31-rad}}$ plus an extra Gaussian dispersion.

2. They use the measured PM of two M31 satellites, M33 (Brunthaler et al. 2005) and IC10 (Brunthaler et al. 2007), assuming that v_{tan} for each satellite follows $\vec{v}_{\text{M31-tan}}$ plus an extra Gaussian dispersion.

3. They use the measured line of sight velocities from outer, non-virialized, LG galaxies, assuming that v_{rad} for each LG galaxy follows the line of sight velocity of the LG barycenter (i.e., center of mass) with respect to the MW plus an extra Gaussian dispersion.

Combining a weighted average of these three independent methods and a χ^2 fit of their residuals provides an estimate for $\vec{v}_{\text{M31}}$ given by

$$\vec{v}_{\text{M31-tan}} = (91 \pm 53) \text{ km s}^{-1} \tag{C5}$$

In determining their uncertainty in equation (C5), van der Marel & Guhathakurta (2008) use the M33 and IC10 PM measurements from Brunthaler et al. (2005) and Brunthaler et al. (2007), respectively, as well as a number of known LG satellite radial velocities, all of which have relatively small uncertainties (e.g., see equation (B25)). However, their assumption that the peculiar velocities for LG satellites follow a Gaussian distribution in their deviation from corresponding values of $v_{\text{M31-rad}}$, $\vec{v}_{\text{M31-tan}}$, $v_{\text{LG-rad}}$, and $\vec{v}_{\text{LG-tan}}$, although justified by the central limit theorem[67], carries an additional nonzero systematic uncertainty. Thus, van der Marel & Guhathakurta (2008) also add an additional source of uncertainty in their estimate of $\vec{v}_{\text{M31-tan}}$ that would otherwise not be present in a direct measurement of the M31 PM.

Sohn et al. (2012) directly measure the M31 PM with the Hubble Space Telescope (HST), using thousands of M31 stars with respect to hundreds of compact background galaxies, all within the same field of view (FOV). Their selection process in finding M31 stars is relatively simple and plethoric due to the large number of detectable stars and reference compact background galaxies within a single HST FOV. They choose three separate M31

[67]The central limit theorem states that any random distribution can be approximated, to first order, by a Gaussian distribution.

fields (a spheroid field near the M31 minor axis, an outer disk field along the M31 major axis, and a field along an extended M31 tidal stream) and measure the PM of stars in each field with respect to compact background galaxies over five to seven year baselines. Although the HST absolute astrometric resolution is approximately 0.2 arcseconds, it can measure relative positions to better than 0.5 milliarcseconds[68]. The large number of individually resolved M31 stars also provides the $\sqrt{N}$ benefit in minimizing the uncertainty for a M31 PM measurement. Additionally, Sohn et al. (2012) use an analysis strategy which accounts for and minimizes systematic errors present in the HST observations. Ultimately, they estimate an uncertainty for their M31 PM measurement on the order of

$$\sigma_{\rm stars} \approx 20\ \mu{\rm as\ yr}^{-1} \tag{C6}$$

van der Marel et al. (2012a) combine the M31 PM measurement from Sohn et al. (2012) and their results from a model using the kinematics of M31 and LG satellite galaxies to estimate $\vec{v}_{\rm M31\text{-}tan}$:

1. They correct for the internal stellar motions of the M31 stars and the Solar reflex motion around the Galactic center to obtain a $\vec{v}_{\rm M31\text{-}tan}$ estimate with respect to the MW center of mass.

2. They construct a LG model to determine $\vec{v}_{\rm M31\text{-}tan}$ using the kinematics of M31 and LG satellites. This method is identical to the approach as used in van der Marel & Guhathakurta (2008; see the beginning of §C.3) except that van der Marel et al. (2012a) use additional satellite data that was previously not available.

van der Marel et al. (2012a) calculate a weighted average of the results from methods 1 and 2 and conclude that

$$\vec{v}_{\rm M31\text{-}tan} = (17 \pm 17)\ {\rm km\ s}^{-1} \tag{C7}$$

Note that method 1, above, may include an additional unaccounted-for systematic uncertainty due to the underlying assumption describing the nature of stellar kinematics for individual M31 stars. Method 2 also contains the same potential additional nonzero uncertainty as described in our discussion of the van der Marel & Guhathakurta (2008) paper, above.

---

[68]Measuring relative photometric positions to a higher accuracy than the absolute resolution (i.e., FWHM) is possible by implementing a fitting procedure to a star's point spread function (PSF). For example, if a star's spatial intensity can be approximated by a two dimensional Gaussian function, then the center of the star, or peak of the Gaussian function, can be estimated to a precision on the order of its $\frac{\rm FWHM}{\rm (S/N)}$, where (S/N) is the star's signal to noise ratio.

Figure 24 shows a comparison of estimates for $\vec{v}_{\text{M31-tan}}$ from equations (C1)-(C5) & (C7).

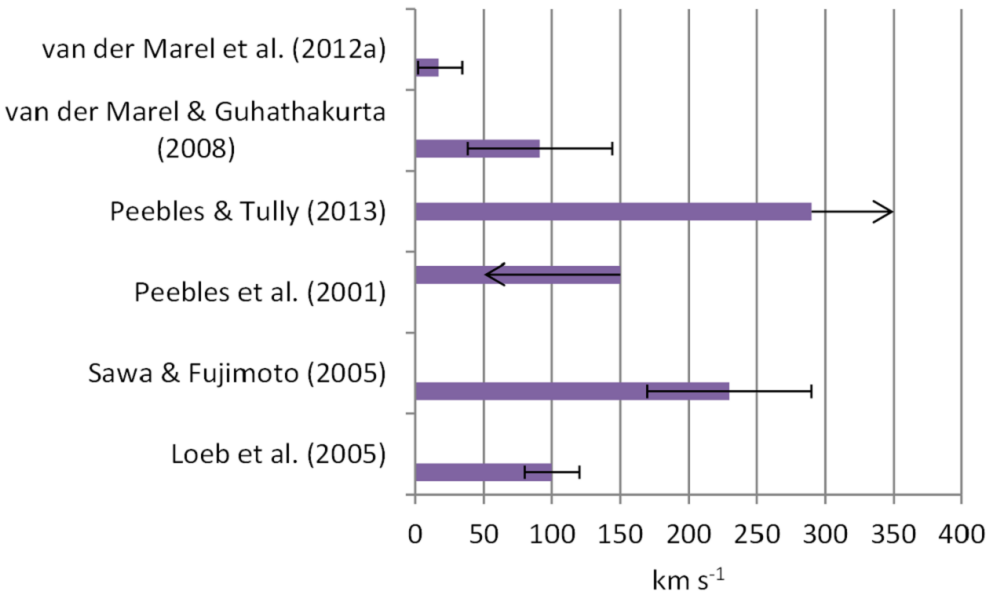

Fig. 24.— A comparison of estimates for $\vec{v}_{\text{M31-tan}}$. Note that the estimate from Peebles et al. (2001) is an upper limit, and the estimate from Peebles et al. (2013) is a lower limit.

Although the $\vec{v}_{\text{M31-tan}}$ estimate from van der Marel et al. (2012; also equation (C7) above) has the smallest uncertainty compared to estimates from Loeb et al. (2005; equation (C1)), Sawa & Fujimoto (2005; equation (C2)), Peebles et al. (2001; equation (C3)), Peebles & Tully (2013; equation (C4)), and van der Marel & Guhathakurta (2008; equation (C5)), the M31 PM uncertainty estimate from Sohn et al. (2012; equation (C6)) is comparable to but slightly larger than the M33 and IC10 PM uncertainty estimate from Brunthaler et al. (2008; equation (B25)). This suggests that a PM measurement of H_2O masers in M31 would provide an even more precise estimate of $\vec{v}_{\text{M31-tan}}$ than equation (C7).

D. Directly Measuring M31 Proper Motion with Masers

D.1. Maser Astrometry

Measuring the PM of masers yields μarcsecond accuracy and precision estimates due to the benefits of the Very Long Baseline Array (VLBA), a network of ten radio telescopes

which span a large portion of the Northern Hemisphere[69]. Figure 25 shows a schematic layout of the VLBA network.

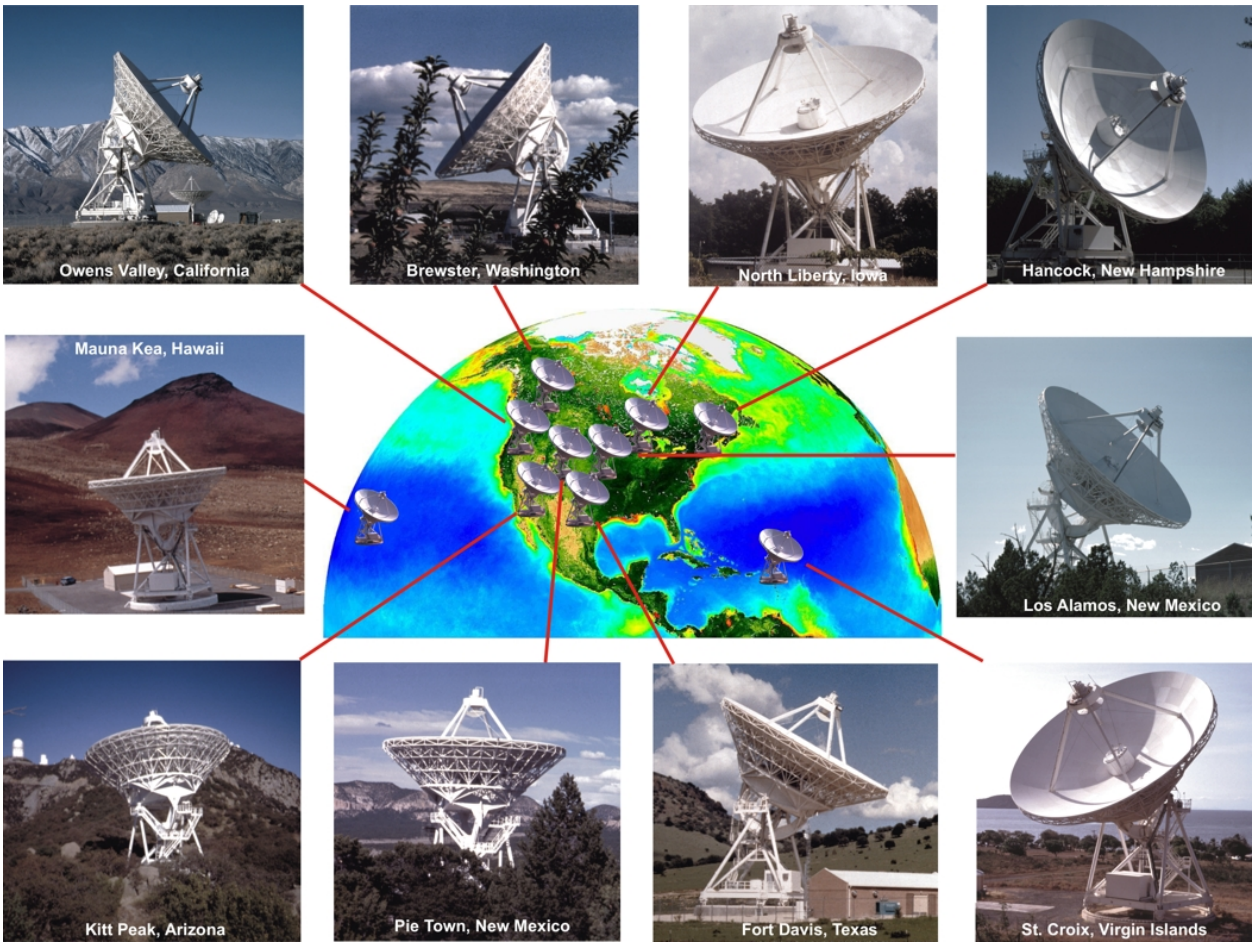

Fig. 25.— A schematic layout of the VLBA network, obtained from http://images.nrao.edu/549; image courtesy of NRAO/AUI, and Earth image courtesy of the SeaWiFS Project NASA/GSFC and ORBIMAGE.

The basic concept which allows the VLBA to make μarcsecond accuracy and precision in PM measurements is the use of interferometry, which combines the signals from each telescope into a network that provides the resolution equivalent to a telescope whose diameter was the same as the longest VLBA baseline ($\sim$8000 km). Thus, the VLBA can resolve an astrophysical H_2O maser, which emits at 23 GHz (1.3 cm), to an absolute resolution given

[69]See www.vlba.nrao.edu. The National Radio Astronomy Observatory (NRAO) is a National Science Foundation facility operated under cooperative agreement by Associated Universities, Inc.

by

$$\begin{aligned} \text{FWHM} &\approx \frac{\lambda}{d} \\ &= \frac{13 \text{ mm}}{8000 \text{ km}} \text{radians} \\ &= 340 \ \mu\text{as} \end{aligned} \tag{D1}$$

However, as discussed in footnote 68, an object's relative position is given roughly by $\sigma \approx \frac{\text{FWHM}}{(S/N)}$. So, for a bright H_2O maser complex observed over a reasonable integration time with a signal to noise of, say, 40, the smallest uncertainty in measuring its relative position for a single epoch is given by

$$\begin{aligned} \sigma_{\text{water maser}} &= \frac{\text{FWHM}}{(S/N)} \\ &= \frac{340 \ \mu\text{as}}{40} \\ &= 8 \ \mu\text{as} \end{aligned} \tag{D2}$$

As we would expect, equation (B25) and equation (D2) present identical results, as Brunthaler et al. (2005) and Brunthaler et al. (2007) both used the VLBA to measure the M33 and IC10 PM, respectively.

D.2. M31 Maser Surveys

Although the VLBA provides unparalleled astrometric capabilities in measuring the relative positions of masers, the physical conditions that give rise to masers, and resultantly the regions on the sky where we look for them, are still not well understood. Churchwell et al. (1977) detected the first extra galactic maser in M33 via an inefficient selection process (i.e., one detection and 15 non-detections). H_2O masers in nearby galaxies are thought to be associated with star-forming regions[70]. This association has so far justified the selection of pointed H_2O maser surveys in M31[71]. However, our current M31 H_2O maser selection process has yielded inefficient results.

---

[70]A typical star during its main lifetime (i.e., undergoing Hydrogen fusion) outputs significantly more energy than is required to break the covalent bonds in a H_2O molecule. Thus, H_2O vapor that is capable of undergoing a population inversion and corresponding stimulated emission is thought to only exist around protostars and star forming regions where the right amount of outgoing energy flux is available to begin an exponential amplification via stimulated emission from radiation.

[71]M31's effective area on the sky is too large for a single comprehensive H_2O maser survey ($\sim 1^\circ$ wide), and thus potential compact H_2O maser regions must be identified in advance.

Greenhill et al. (1995) conducted a pointed H_2O maser survey towards HII regions[72] in M31 and found no detections. Imai et al. (2001) conducted a pointed H_2O maser survey in 330 different M31 regions towards candidates indicating the presence of both HII regions and molecular clouds and still found no detections. The non-detection from both Greenhill et al. (1995) and Imai et al. (2001) indicates an absence of H_2O masers in the observed M31 regions above the respective survey sensitivity limits. However, M31 H_2O maser detections below the respective survey sensitivity limits remains a possibility and therefore warrants future M31 surveys in the same or similar regions but with greater sensitivity.

Sjouwerman et al. (2010) present the first M31 maser detection of any type, a Class II 6.7 GHz methanol (CH_3OH) maser, using the Green Bank Telescope (GBT). Although a highly accurate and precise VLBA PM measurement of this maser is possible, it's own individual peculiar velocity is likely impossible to distinguish from the M31 velocity components representing translation, rotation, and divergence[73]. 6.7 GHz methanol masers represent the second brightest known type of Galactic maser, only surpassed by 22 GHz H_2O masers. A search for 22 GHz H_2O masers in the same M31 region found no detections. However, this M31 methanol maser detection suggests that M31 H_2O masers are detectable within the GBT sensitivity.

Darling (2011) detects and confirms five H_2O maser complexes in M31 using the GBT. In contrast to previous M31 H_2O maser surveys, Darling (2011) selects potential M31 compact star forming regions based on their 24 μm luminosity[74] (Gordon et al., 2006). Figure

---

[72]HII regions are believed to indicate the presence of star forming regions as follows. Star formation is believed to occur in large quantities on a relatively short time scale (e.g., hundreds of stars embedded in a single molecular cloud all form around the same time). However, impurities in the compressing gas cloud which forms the new group of stars results in a broad range of stellar masses. Only the hottest and most massive stars, which live for a few million years, output enough ultraviolet energy at 13.6 eV or greater (i.e., the energy required to fully ionize a neutral hydrogen atom) to observe the resulting series of hydrogen recombination lines from Earth (the observation of hydrogen recombination lines indicates the previous, relatively recent occurrence of hydrogen ionization). However, the lower mass stars can live for billions of years. Thus, regions of ionized hydrogen are thought to indicate the presence of extremely massive stars, whose entire lifetimes are still in the early stages of star formation with respect to the lower mass stars, and resultantly indicate the recent occurrence of star formation.

[73]Thus, assuming that a large number of peculiar maser velocities throughout M31 should average out to zero without a necessary correction for internal M31 kinematic motion, a greater number of M31 maser detections will allow for a greater accuracy and precision in measuring the M31 proper motion.

[74]24 μm emission is dominated by thermal blackbody radiation from dust grains (i.e., condensed refractory minerals which range from a few molecules wide to 0.1 μm wide). Dust grains are typically blown away from hydrogen fusion-burning stars due to stellar winds, but stellar winds in star forming regions are weak enough for dust grains to remain present and resultantly absorb light of comparable wavelength to their size (and

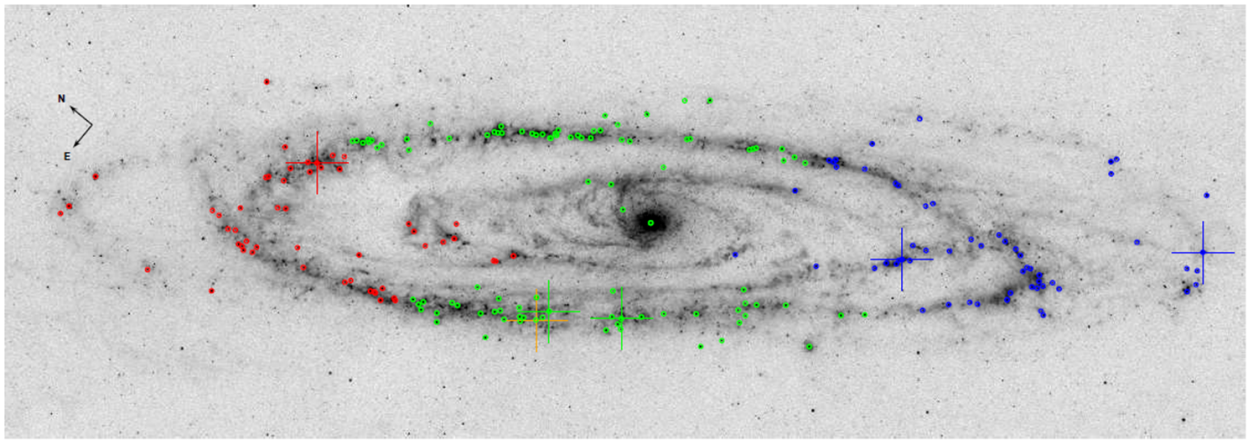

Fig. 26.— A M31 24 μm map (Gordon et al., 2006), adapted from Figure 1 in Darling (2011), showing the 200 most luminous compact regions (circles), all used as potential maser regions in a pointed M31 H_2O maser survey (Darling, 2011). The 5 detected 22 GHz H_2O masers (Darling, 2011) are indicated with a cross, and the single detected 6.7 GHz methanol maser (Sjouwerman et al., 2010) is indicated with an orange cross. The colors indicate the systemic portion (green), redshifted portion (red), and blueshifted portion (blue) of M31 relative to the MW.

26 (adapted from Figure 1 in Darling, 2011) shows the 200 selected M31 compact 24 μm regions, the 5 confirmed 22 GHz H_2O maser detections (Darling, 2011), and the single 6.7 GHz methanol maser detection (Sjouwerman et al., 2010). Use of the VLBA will allow for μas resolution of these masers' relative positions on the sky. Follow up observations with the VLBA over a 2-3 year baseline will then provide highly accurate and precise measurements of the masers' PM on the order of $\sigma_{\text{water masers}} = 5$ μas yr^{-1}, corresponding to a M31 transverse velocity on the order of $\sim$18 km s^{-1} (see equation (B25) above and also §5.3 in Darling, 2011).

E. Summary

Based on the results presented in Brunthaler et al. (2005) and Brunthaler et al. (2007), we expect that PM measurements of the only detected M31 H_2O masers (Darling, 2011) will yield the most accurate and precise value yet for $\vec{v}_{\text{M31-tan}}$, and thus for $\vec{v}_{\text{M31}}$. A more

---

also wavelengths that are blue-ward of their size). The dust grains will then re-emit their absorbed light as thermal blackbody radiation which peaks at 24 μm, indicating their presence in a star forming region.

accurate and precise value of $\vec{v}_{\rm M31}$ will allow for

- a more accurate and precise estimate of the MW, M31, and LG mass,
- a more accurate understanding of the dark matter halo structure for the LG and its components (and resultantly a more accurate understanding of the ΛCDM theory's applicability to the LG),
- a more accurate understanding of the LG's past evolution and the origin of it's many dwarf satellite galaxies,
- and a more accurate understanding of the LG's future evolution, including the anticipated future collision between the MW and M31, the fate of the Solar System during and after this collision, and the fate of other LG galaxies during and after this collision.

REFERENCES

Ao, Y., Henkel, C., Braatz, J. A., et al. 2011, A&A, 529, A154

Avalos, M., & Lizano, S. 2012, ApJ, 751, 63

Binney, J., & Tremaine, S. 1987, Princeton, NJ, Princeton University Press, 1987, 747 p.

Brunthaler, A., Henkel, C., de Blok, W. J. G., et al. 2006, A&A, 457, 109

Brunthaler, A., Reid, M. J., Falcke, H., Greenhill, L. J., & Henkel, C. 2005, Science, 307, 1440

Brunthaler, A., Reid, M. J., Falcke, H., Henkel, C., & Menten, K. M. 2007, A&A, 462, 101

Brunthaler, A., Reid, M. J., Falcke, H., Henkel, C., & Menten, K. M. 2008, IAU Symposium, 248, 474

Burke, B. F. & Graham-Smith, F. 2010, An Introduction to Radio Astronomy, 3rd edition, by Bernard F. Burke and F. Graham-Smith. Cambriage University Press, 437 pages.

Carroll, B. W. & Ostlie, D. A. 2006, An Introduction to Modern Astrophysics and Cosmology, San Francisco, CA: Pearson

Chapman, J. M., & Baan, W. A. 2008, Astrophysical Masers and their Environments (IAU S242), UK: Cambridge University Press

Chemin, L., Carignan, C., & Foster, T. 2009, ApJ, 705, 1395

Churchwell, E., Witzel, A., Huchtmeier, W., et al. 1977, A&A, 54, 969

Cox, T. J., & Loeb, A. 2008, MNRAS, 386, 461

Darling, J. 2011, ApJ, 732, L2

de Vaucouleurs, G., de Vaucouleurs, A., Corwin, H. G., Jr., et al. 1991, S&T, 82, 621

Dunham, M. K., Rosolowsky, E., Evans, N. J., II, Cyganowski, C., & Urquhart, J. S. 2011, ApJ, 741, 110

Fich, M., & Tremaine, S. 1991, ARA&A, 29, 409

Ford, G. P., Gear, W. K., Smith, M. W. L., et al. 2013, ApJ, 769, 55

Fouquet, S., Hammer, F., Yang, Y., Puech, M., & Flores, H. 2012, MNRAS, 427, 1769

Gordon, K. D., Bailin, J., Engelbracht, C. W., et al. 2006, ApJ, 638, L87

Greenhill, L. J., Henkel, C., Becker, R., Wilson, T. L., & Wouterloot, J. G. A. 1995, A&A, 304, 21

Henkel, C., Mauersberger, R., Peck, A. B., Falcke, H., & Hagiwara, Y. 2000, A&A, 361, L45

Herzberg, G. 1966, New York: Van Nostrand, Reinhold, 1966

Imai, H., Ishihara, Y., Kameya, O., & Nakai, N. 2001, PASJ, 53, 489

Kahn, F. D., & Woltjer, L. 1959, ApJ, 130, 705

Karachentsev, I. D., & Kashibadze, O. G. 2006, Astrophysics, 49, 3

Kibble, T. W. B. 1985, Classical Mechanics (London: Longman)

Kochanek, C. S. 1996, ApJ, 457, 228

Li, Y.-S., & White, S. D. M. 2008, MNRAS, 384, 1459

Longmore, S. N., Bally, J., Testi, L., et al. 2013, MNRAS, 429, 987

Loeb, A., Reid, M. J., Brunthaler, A., & Falcke, H. 2005, ApJ, 633, 894

McConnachie, A. W., Irwin, M. J., Ferguson, A. M. N., et al. 2005, MNRAS, 356, 979

Merrett, H. R., Merrifield, M. R., Douglas, N. G., et al. 2006, MNRAS, 369, 120

Molinari, S., Swinyard, B., Bally, J., et al. 2010, A&A, 518, L100

Nieten, C., Neininger, N., Guélin, M., et al. 2006, A&A, 453, 459

Peebles, P. J. E., Phelps, S. D., Shaya, E. J., & Tully, R. B. 2001, ApJ, 554, 104

Peebles, P. J. E., & Tully, R. B. 2013, arXiv:1302.6982

Sawa, T., & Fujimoto, M. 2005, PASJ, 57, 429

Sjouwerman, L. O., Murray, C. E., Pihlström, Y. M., Fish, V. L., & Araya, E. D. 2010, ApJ, 724, L158

Smith, M. W. L., Eales, S. A., Gomez, H. L., et al. 2012, ApJ, 756, 40

Sohn, S. T., Anderson, J., & van der Marel, R. P. 2012, ApJ, 753, 7

Springel, V., White, S. D. M., Jenkins, A., et al. 2005, Nature, 435, 629

Urquhart, J. S., Hoare, M. G., Purcell, C. R., et al. 2009, A&A, 501, 539

Urquhart, J. S., Hoare, M. G., Lumsden, S. L., et al. 2009, A&A, 507, 795

Urquhart, J. S., Morgan, L. K., Figura, C. C., et al. 2011, MNRAS, 418, 1689

van der Marel, R. P., & Guhathakurta, P. 2008, ApJ, 678, 187

van der Marel, R. P., Fardal, M., Besla, G., et al. 2012a, ApJ, 753, 8

van der Marel, R. P., Besla, G., Cox, T. J., Sohn, S. T., & Anderson, J. 2012b, ApJ, 753, 9

Walterbos, R. A. M., & Kennicutt, R. C., Jr. 1987, A&AS, 69, 311

Watkins, L. L., Evans, N. W., & An, J. H. 2010, MNRAS, 406, 264

Wilson, T. L., Rohlfs, K., & Huttemeister, S. 2012, Tools of Radio Astronomy, 5th edition, by Thomas L. Wilson; Kristen Rohlfs and Susanne Hüttemeister. Moscow: Fizmatlit, 568 pages.

Yin, J., Hou, J. L., Prantzos, N., et al. 2009, A&A, 505, 497